



TAMPERE UNIVERSITY OF TECHNOLOGY

MATTI JAVANAINEN

OXYGEN - TO LUNG SURFACTANT AND BEYOND

Masters of Science Thesis

Tarkastaja: Ilpo Vattulainen
Tarkastaja ja aihe hyväksytty
Ympäristötekniikan ja luonnontieteiden
tiedekunnan kokouksessa 9.11.2011

TIIVISTELMÄ

TAMPEREEN TEKNILLINEN YLIOPISTO

Teknis-luonnontieteellinen koulutusohjelma

JAVANAINEN, MATTI: Hapen kulkeutumisesta keuhkokalvon läpi

Diplomityö, 89 sivua

January 2012

Pääaine: Teknillinen fysiikka

Tarkastaja: professori Ilpo Vattulainen

Ohjaajat: TkT Luca Monticelli, professori Ilpo Vattulainen

Avainsanat: Biologinen fysiikka, molekyyliidynamiikka, vapaaenergia, diffuusio, keuhkokalvo, happi, läpäisevyys, yksikerroskalvo, epähomogeeninen liukoisuus–diffuusio-malli

Keuhkojen pinta-aktiivinen aine muodostaa keuhkorakkuloiden sisäpinnalla ohuen kalvon veden ja ilman väliseen rajapintaan. Tämän kalvon tärkein tehtävä on keuhkorakkuloiden pintajännityksen alentaminen siten, etteivät ne uloshengityksen aikana painu kasaan. Keuhkojen hengitysmekanismin toiminnan mahdollistamisen lisäksi keuhkokalvon uskotaan vaikuttavan pienten molekyylien, kuten hapen, kulkeutumiseen sisäänhengitetystä ilmasta verenkiertoon. Aiemmat aihetta käsitelleet tutkimukset ovat kuitenkin johtaneet ristiriitaisiin johtopäätöksiin. Laskennallisten tutkimusten luotettavuutta ovat rajoittaneet muun muassa keuhkokalvomallien yksinkertaistukset, simulaatiomallien puutteet ja rajoitetut laskentaresurssit. Kokeellisella puolella ongelmana on usein menetelmien rajoitettu tarkkuus.

Näiden sudenkuoppien välttämiseksi proteiinittomien keuhkokalvosysteemien läpäisevyysominaisuuksia tarkasteltiin pitkien, atomaarisen tarkkuuden molekyyliidynamiikkasimulaatioiden avulla. Kokeellisesti mitattua lipidikoostumusta vastaavia yksikerroskalvoja tutkittiin altistamalla ne erisuuruisille jännityksille biologisessa ympäristössä. Simulaatioita laajennettiin myös kaksoiskalvorakenteisiin, jotta hapen mahdollisia kulkeutumisreittejä voitiin tutkia vesi-ilma-rajapinnan jälkeisissä kalvorakenteissa.

Simulaatioita varten happimolekyyliä kehitettiin uusi malli, joka käytökseltään vastasi reaali maailman molekyyliä aiempia atomistisia kuvauksia paremmin. Kalvorakenteiden läpäisevyys happimolekyyliä selvitettiin käyttäen vapaaenergiamenetelmiä. Epähomogeeninen liukoisuus–diffuusio-malli yhdistettynä tiettyyn simulaatioalgoritmiin mahdollisti sen, että sekä energieettisten että kineettisten tekijöiden vaikutus läpäisevyyteen voitiin selvittää huomattavasti kokeellisia menetelmiä tarkemmin. Laskettujen vapaaenergia- ja diffuusiiovakioprofiilien tärkeimmät tunnusluvut täsmäsivät hyvin kokeellisesti mitattujen arvojen kanssa, mutta yksityiskohtaisista profileista saatiin myös uutta ja kiinnostavaa tietoa. Yksikerroskalvojen läpäisevyydet pystyttiin menestyksekkäästi yhdistämään muihin näitä kalvoja kuvaaviin suureisiin. Mahdollisten yksikerroskalvojen alla sijaitsevien kalvorakenteiden hapenkuljetuskykyä vertailtiin keskenään. Kaikkia laskettuja arvoja verrattiin perusteellisesti sekä kokeellisten että laskennallisten tulosten kanssa.

ABSTRACT

TAMPERE UNIVERSITY OF TECHNOLOGY

Degree Programme in Science and Engineering

JAVANAINEN, MATTI: Oxygen - To Lung Surfactant and Beyond

Masters of Science Thesis, 89 pages

January 2011

Major: Technical Physics

Examiner: Professor Ilpo Vattulainen

Supervisors: PhD Luca Monticelli, Professor Ilpo Vattulainen

Keywords: Biological physics, molecular dynamics, free energy, diffusion, lung surfactant, oxygen, permeation, monolayer, inhomogeneous solubility–diffusion model

Lung surfactant is a thin lining covering the air–water interface inside the alveoli. Its main function is to reduce the surface tension at this interface and thus prevent the alveoli from collapsing at the end of the breathing cycle. In addition to its importance in maintaining proper lung function, it is suggested that this monolayer affects the permeation of small non-electrolytes such as molecular oxygen from inhaled air towards circulation. However, the results on this topic are extremely diverse. Earlier computational studies have been inadequate in terms of monolayer composition and state, simulation conditions and force field parametrisations and the amount of employed computational resources. They have also often considered either energetic or kinetic factors on permeability alone. On the other hand, lack of resolution has been the main issue with experimental studies on oxygen permeability.

To overcome these limitations, the permeation properties of protein-free surfactant membrane systems were studied through long atomistic molecular dynamics simulations with high spatial resolution. Monolayers at different compression states were employed with the lipid composition and simulation conditions of the systems mimicking that of the real surfactant. In addition to the permeation properties of the monolayer, information about oxygen pathways below the interface were also discussed with the data obtained from bilayer simulations with the same composition.

A new model for molecular oxygen was sought in this study and its performance was verified with multiple benchmarks. A special free energy technique, the z constraint method was employed together with the inhomogeneous solubility–diffusion model to study the permeabilities of the membrane systems as it provides one with detailed information about both energetic and kinetic factors on permeation. The key values of the spatially resolved free energy and diffusion coefficient profiles along the membrane normal agree with those of earlier studies yet the detailed profiles also provide new and interesting information. The calculated permeabilities of the monolayer systems are successfully linked to the other physical quantities characterizing the monolayers. The possible suggested structures lying below the surfactant monolayer are compared based on their effect on oxygen transport. Finally, thorough comparison is performed between our calculations and earlier studies.

PREFACE

This Thesis was written as part of my research work on lung surfactant conducted during the last four years. I have been privileged to work as a research assistant as a part of the Biological Physics and Soft Matter Research group located in the Department of Physics at the Tampere University of Technology.

I am very thankful for Prof. Ilpo Vattulainen for providing me the possibility for challenging and independent work in a renowned and international research group. I want to express my great thanks to Ph.D. Luca Monticelli for guiding and supervising me throughout the project even from a long distance through these four years.

I also appreciate all the help from other members of the group. I especially want to thank M.Sc. Antti Lamberg for all the technical support and scientific discussions. After his departure, Ph.D. Hector Martinez-Seara Monné has acted as an acceptable replacement for Antti. I greatly appreciate the gang of the Bat Cave, SG317, for providing young minds from different fields a place where to share ideas and thoughts. It was a great pleasure to share offices with M.Sc. Bernhard Reischl and M.Sc. Sanja Pöyry.

I also want to thank my family and friends for all the support throughout the years. The most special thanks goes to Linda who managed to support me even though hiding somewhere far away for most of the time I spent with the Thesis.

After six years of successful M.Sc. studies, the next phase in life is about to begin. During the next three to four years I will continue to work in my home group as a Ph.D. student focusing on the dynamical aspects of proteins and their interplay with lipid molecules. This means good times for energy drink and chewing gum companies. . .

Tampere, May 28th, 2012

SYMBOLS & ABBREVIATIONS

$\Delta A(z)$	Position-dependent Helmholtz free energy difference
$C_{(12)}^A$	The Lennard-Jones parameter related to r^{12} in reference state
$C_{(12)}^B$	The Lennard-Jones parameter related to r^{12} in target state
$C_{(6)}^A$	The Lennard-Jones parameter related to r^6 in reference state
$C_{(6)}^B$	The Lennard-Jones parameter related to r^6 in target state
c	Concentration
c_{organic}	Concentration of solute in organic phase
c_{water}	Concentration of solute in aqueous phase
$c(z)$	Concentration at z
c^*	Concentration of bulk solute
$c^{\text{eq}}(z)$	Equilibrium concentration at z
CLP	Crossed layers of parallels
D	Diffusion coefficient
$D_z(z)$	Diffusion coefficient in z direction at z
$D_{xy}(z)$	Lateral diffusion coefficient at z
DMPC	Dimyristoylphosphatidylcholine
DOPC	Dioleoylphosphatidylcholine
DPPC	Dipalmitoylphosphatidylcholine
d_c	Membrane thickness
F_z	Force in z direction
$F_z(z), F_z(z')$	Force in z direction at position z or z'
$\Delta F_z(z, t)$	Deviation of the mean force in z direction at position z , time t
$F_i(t)$	Force on particle i at time t
$F_{\text{soft-core}}(r_{ij}, \lambda)$	Soft-core force at state λ
$F^A(r_A), F^B(r_B)$	Forces in states A and B
FFT	Fast Fourier Transform
f_{ij}	Scaling factor for non-bonded interactions
G	Gibb's free energy
ΔG_{water}	Free energy of solvation into aqueous phase
$\Delta G_{\text{organic}}$	Free energy of solvation into organic phase
$\Delta G_{\text{water} \rightarrow \text{organic}}$	Free energy of partitioning from water phase to organic phase
$G(\lambda)$	Free energy of state λ
H	Enthalpy
$\Delta_{\text{vap}} H^p$	Enthalpy of vaporisation at constant pressure

h	Planck's constant
ΔH	Enthalpy change
$\mathcal{H}(\mathbf{r}^N, \mathbf{p}^N, \lambda)$	Hamiltonian of state λ
\mathcal{H}^A	Hamiltonian of the reference state
\mathcal{H}^B	Hamiltonian of the target state
$\mathcal{H}_{\text{Coulombic}}$	Potential term for Coulombic interactions
$\mathcal{H}_{\text{bond stretching}}$	Potential term for bond stretching
$\mathcal{H}_{\text{Lennard-Jones}}$	Potential term for Lennard-Jones interactions
$\mathcal{H}_{\text{soft-core}}(r_{ij}, \lambda)$	Soft-core potential function at state λ
$\mathcal{H}_{\text{total}}$	Total potential function
$\mathcal{H}_{\text{bonded}}$	Potential function of bonded interactions
$\mathcal{H}_{\text{non-bonded}}$	Potential function of non-bonded interactions
J	Flux of solute
$J_z(z)$	Flux of solute in z direction at location z
$k_{r,i}$	Force constant for bond i
$k_{\theta,i}$	Force constant for angle i
LJ	Lennard-Jones
MD	Molecular dynamics
MLMPC	DMPC lipid with perdeuterated sn-2 chain
m	Mass
m_i	Mass of particle i
N	The number of particles in the system
N_A	Avogadro's constant
NMR	Nucleomagnetic resonance, a spectroscopy method
n	Amount of substance in moles
OPLS	'Optimized Potentials for Liquid Simulations', a force field
P	Partitioning ratio
\mathcal{P}	Permeability (coefficient)
PME	Particle Mesh Ewald
p	Pressure
p_V	Pressure in constant pressure situation
s	Soft-core power
\mathbf{p}^N	Momenta of the N particles
PC	Phosphatidylcholine
PG	Phosphatidylglycerol
POPC	Palmitoyloleoylphosphatidylcholine
POPG	Palmitoyloleoylphosphatidylglycerol
$Q'(z), Q'(z_1)$	Partition function, particle restricted to $[z, z+dz]$ or $[z_1, z_1+dz]$
Q_{ij}	The ij component of quadrupole moment tensor

q_i, q_j, q_l	Charges on particles i, j and l
q_i^A, q_j^A	Charges on particles i and j in reference state
q_i^B, q_j^B	Charges on particles i and j in target state
R	Universal gas constant
R^p	Permeation resistance
\mathcal{R}	Total permeation resistance
$\mathbf{r}(t)$	Two-dimensional coordinate vector at time t
\mathbf{r}^N	Coordinates of the N particles
$\mathbf{r}_i(t)$	Coordinates of particle i at time t
r_A	Parameter related to soft-core interactions in reference state
r_B	Parameter related to soft-core interactions in target state
$r_i, r_{i,0}$	The length and the equilibrium length of bond i
r_{ij}	The distance between particles i and j
r_l	Component l of distance
S	Entropy
ΔS	Entropy change
SP-B	Surfactant protein B
SP-C	Surfactant protein C
SPC	Single Point Charge, a water force field
T	Absolute temperature
t	Time
Δt	Time step
U	Internal energy
U_{liquid}	Internal energy of the liquid phase
U_{vapour}	Internal energy of the vapour phase
u	Average velocity of particles
V	Volume
$V(\lambda)$	Volume at state λ
V^0	A normalization constant
V_0, V_1, V_2, V_3	Multipliers in the cosine series for dihedral potential
v_j	Speed of particle j
$\mathbf{v}_i(t)$	Velocity of particle i at time t
x_i, x_j	Coordinates of particles with i, j taking the values x, y and z
Δz	The change in z coordinate of the solute over one time step
α	Soft-core parameter
β	Short for $\frac{1}{k_B T}$
$\delta(z_0 - z)$	Dirac delta function, non-zero value at $z = z_0$
δ_{ij}	Kronecker delta
ε_0	Permeability of vacuum

ε_r	Relative permeability of the medium
$\theta_i, \theta_{i,0}$	The angle i and its equilibrium value
λ	Coupling parameter for thermodynamic integration method
μ	Chemical potential
$\mu(z)$	Chemical potential at z
$\mu(z_1), \mu(z_1)$	Chemical potential on opposite sides of the membrane system
μ^0	Standard chemical potential
$\Delta\mu$	Chemical potential difference over the membrane system
ξ	Friction coefficient
$\xi(z, t)$	Friction coefficient at position z at time t
$\xi^S(z)$	Static friction coefficient at position z
$\rho(r)$	Charge density at position r
σ_A, σ_B	Lennard-Jones parameter for states A and B
ϕ	Dihedral angle
ϕ_i	Difference of the dihedral angle i from its reference value
Δ	Isothermal–isobaric partition function
$\Delta(\lambda)$	Isothermal–isobaric partition function at given λ

CONTENTS

1. Introduction	1
2. Biological Background	4
2.1 Overview of the Human Lung	4
2.2 Lung Surfactant	6
2.3 Lipid Structures below the Lung Surfactant	8
2.4 Structure and Function of Lipids	10
2.5 Lipids of the Pulmonary Surfactant	11
3. Thermodynamic Integration Method	14
3.1 Partitioning and Free Energy	14
3.2 Thermodynamic Integration	16
3.3 Potential Functions for Thermodynamic Integration	19
4. Theory of Permeation	21
4.1 General Properties of Permeation Processes	21
4.2 Homogeneous Solubility–Diffusion model	23
4.3 Inhomogeneous Solubility–Diffusion model	23
4.3.1 Theoretical Description	26
4.3.2 Relation to Computationally Available Quantities	28
4.3.3 Free Energies from Mean Force	30
4.3.4 Local Diffusion Coefficients from Force Autocorrelation	31
4.4 Oxygen Permeation through Membranes	32
5. Computational Methods	36
5.1 Overview of Molecular Dynamics	36
5.2 Thermodynamic Integration	40
5.3 Other Methods of Validation	42
5.4 Permeation Studies	44
6. Results	48
6.1 O ₂ Parameters from Thermodynamic Integration	48
6.2 Oxygen Permeation	52
6.2.1 Adequacy of Sampling	52
6.2.2 Excess Free Energy Profiles	52
6.2.3 Entropic and Energetic Components	57
6.2.4 Local Diffusion Coefficients	58
6.2.5 Permeation Resistance Profiles	62
6.2.6 Total Permeation Resistances and Permeabilities	65
6.2.7 Dependence of Permeability on Physical Quantities	67
6.2.8 Comparison to Density and Free Volume Profiles	69
6.3 Free Oxygen Molecules	70
6.4 Permeation below the Surfactant Monolayer	71
7. Concluding Remarks	74
Bibliography	77

1. INTRODUCTION

The study on biological systems forms an extremely interesting field covering a large amount of different research areas and methodology both in experimental and computational sciences. The great variety of length scales spanned by structures in soft matter together with the intriguing phenomena occurring in a large range of time scales substantially increase both the complexity and fascination of studying biological systems.

Experimental methods are usually quite limited in studying soft matter due to its dynamic and fragile nature. The data obtained from experiments is often indirect and greatly affected by the perturbations caused by the applied methodology and fluctuations in both external and internal variables. Further limitations are imposed by the resolution required to examine the often most exciting nanometre-level interactions and structural features of the studied system.

Despite these shortcomings, the importance of experiments cannot be underrated. They can nowadays, however, be accompanied by computational studies which are unaffected by the factors listed above. They naturally have their own weaknesses often characterized by balancing between the accuracy of the model and the reachable time and length scales. Of the large group of computational techniques available, biological nanosystems governed by mainly physical interactions and energy scale fixed by thermal fluctuations pose an ideal target for a classical computational method called molecular dynamics. This method maintains atomistic resolution yet discards the electronic interactions in the favour of larger system sizes and longer simulation times.

The key component of the mammalian lung is the pulmonary surfactant, a thin lining covering the small alveoli at the interface which separates the inhaled air from the aqueous nature that constitutes most of our body mass [1]. The functionality of this surfactant is vital for the lungs as it prevents the alveoli from collapsing during the exhaling step of the breathing cycle [2]. It is also considered to play an important role in the permeation of gases from an alveolus to the circulation and vice versa [3, 4]. In this study we focus our interest in oxygen permeability through this surfactant and membrane structures that lie in close vicinity to the air–water interface.

The permeability of biological membranes and monolayers for various small non-

electrolytes and in particular molecular oxygen have been studied both experimentally, see e.g. Refs. [5–7], and through computer simulations, see e.g. Refs. [8–10]. The results of previous studies have been extremely diverse and there is currently no consensus on the field on the effect of lung surfactant structures on the permeability of oxygen.

The experimental studies have been limited by their resolution and the perturbations caused by the measurement process itself. Also, the variation of results between studies can also be explained by different external and internal conditions, monolayer state and employed technique. Computational studies have also had their own issues. Models are often oversimplified, simulation times inadequate and bilayers have gained much more attention than monolayers. In addition, a common problem with both experimental and computational studies is that they usually consider only either the energetic or the kinetic factors on permeation yet they both are supposed to have an effect on the process [11].

In this study we employ the molecular dynamics methodology which is able to provide us with detailed information on the atomistic level. The systems constructed follow the measured compositions of the lung surfactant and they represent the surfactant monolayer at different compression states and are thus characterized by varying area per lipid molecule and therefore surface tension. They are simulated in biologically relevant environments for long enough times to provide trustworthy information on the permeation process in a far more detailed manner than what is obtained even in the most sophisticated experiments.

This thesis consists of seven chapters. Description of the structural and functional features of the lung and the pulmonary surfactant system together with the components it consists of are given after this introduction.

This is followed by the theoretical background for the development and verification of the oxygen model employed in the permeation studies. A short review of thermodynamic cycles, free energy and partitioning is given. These concepts are linked to simulations by the introduction of the thermodynamic integration method. This chapter is closed with details on the implementation aspects of this method in the employed simulation software.

The fourth chapter concentrates on permeation processes. To begin with, the general concepts and features of permeation processes in biological systems are listed. This is followed by the introduction of models that seek to explain the permeation through biological membranes. The inhomogeneous solubility–diffusion model is explained in detail and its mathematical derivation is given. The theoretical description is linked to computer simulations and finally the studies on oxygen permeation are reviewed.

The aim of this study is to calculate the permeabilities of lung surfactant model

systems for oxygen and to examine if the surfactant has an effect on oxygen kinetics within the lungs. The permeabilities are obtained by employing an inhomogeneous solubility–diffusion model [11, 12] that relates permeation to both energetic and dynamic quantities. First, however, the optimal parameters for molecular oxygen are sought through thermodynamic integration method and further verified by other benchmarks. The optimal description for oxygen is then employed in all permeation studies.

The results obtained for different compression states are compared to their other physical quantities in order to find qualitative dependencies between these factors. All results are explained with the aid of the four region model [12] and thoroughly compared to experiments and other simulation studies. In addition, the effect of suggested membrane structures residing below the surfactant monolayer on oxygen permeation is evaluated with the aid of data obtained from simulations of lung surfactant bilayers. These bilayers also simplify the comparison of the results between our study and experimental and computational studies on oxygen permeation through lipid bilayers.

The computational methods employed are explained in the fifth chapter. The general concepts of the molecular dynamics simulation method are first discussed and a detailed listing of the utilized simulation parameters is given for all types of simulations performed in this work.

The results section is divided into two. First, the optimal parameter set for the oxygen molecule is given with the reasoning based on comparison of its selected properties to those measured for other models and in experiments. This is followed by a thorough analysis of the results obtained from the permeation studies. Energetic and kinetic factors of permeation are discussed. The dependencies of the obtained permeability values on physical properties characterizing the pulmonary surfactant at different compression states are sought. The possible pathways for oxygen permeation below the surfactant monolayer are also discussed based on the results obtained for the bilayer system. All the results are compared to available computational and experimental data.

The thesis is summarized in the last chapter. The key results are reviewed and possible future directions are discussed.

2. BIOLOGICAL BACKGROUND

In this chapter a top-down approach is used to describe the biological structures relevant to this study. First the general structural and functional features of the mammalian lung are presented. Then a brief insight into the structure and function of the pulmonary surfactant structures in the alveoli is given. The chapter is closed with a discussion about the main building blocks of the surfactant, lipids, with an emphasis on the molecules employed in this study.

2.1 Overview of the Human Lung

The human lung consists of two zones. The conducting zone is responsible for the transport of air towards the sites at which gas exchange takes place. Air is simultaneously warmed, humidified and purified during this transport process [13]. The conducting zone consists of the trachea and the two primary bronchi that continue branching into a larger number of narrower secondary and further tertiary bronchi and finally into bronchioles [1].

The respiratory zone is responsible for gas exchange and it consists of the respiratory bronchioles and the alveolar ducts that finally end up to small and spherical air sacks called the alveoli [1, 14]. The lungs of a grown-up human may have a respiratory surface area of as high as 70 m² due to the total number of alveoli being around 500 million [14, 15]. This kind of a branched structure is characteristic only for the mammalian lung. Part of the respiratory zone is presented in Fig. 2.1.

The alveoli are the sites at which gas exchange between inhaled air and blood takes place. An alveolus has a diameter of about 0.2–0.3 mm but this value is significantly increased during inhalation [14, 16]. About 70% of the surface area of an alveolus is covered with tiny alveolar capillaries [17]. The carbon dioxide rich artery blood is transported to the lung and the oxygenated venous blood is carried away to the tissues along these capillaries. Non-polar oxygen molecules bind to haemoglobin inside the red blood cells during transportation while polar carbon dioxide molecules travel mostly dissolved in blood [1]. In the alveoli carbon dioxide is transported from blood to the alveoli and exhaled while oxygen from inhaled air is absorbed into haemoglobin [1].

Except for some micro organisms like bacteria or virae living in an anaerobic environment, all living beings need oxygen to maintain their metabolism. Energy

usable for the cells is released when the nutrients of food undergo redox reactions [18]. Puryvate formed in glycolysis can undergo either aerobic respiration in mitochondria or lactic acid fermentation in the cytoplasm in the absence of oxygen to form ATP [18]. Since humans are unable to store large amounts of ATP in their bodies, a constant intake of oxygen is required [19].

The human lung has a large reserve capacity that is not needed in normal conditions. The blood becomes saturated with oxygen already during the first third of the time it spends in the pulmonary capillaries and not all of the inhaled oxygen is transported to the capillaries at all [1]. However, during exercise the time that blood spends in the capillaries may be reduced to only one third of the corresponding value at rest, which is about 0.75 s [1]. Some diseases such as the chronic obstructive pulmonary disease (COPD) caused by e.g. smoking, occupational exposure or air pollution can also hinder the diffusion of oxygen from the alveoli to the capillaries by reducing the area available for permeation or by increasing the thickness of the alveolar wall [20]. In these situations the reserve capacity is needed in order to satisfy the oxygen demand of the cells.

The function of the lung is not restricted only to respiration. The pH value of the blood is controlled by the alteration of the partial pressure of carbon dioxide [21]. The gas micro-bubbles and small blood clots are also filtered out by the lung [1, 22]. The lungs control the levels of some biological substances [1] and maintain their own sterility by the production of compounds with antimicrobial function [23].

In order for the oxygen molecules to travel from an alveolus to the haemoglobin carried by the red blood cells and thus into the circulation, they must pass through various structures such as the pulmonary surfactant structures including the monolayer at the air–water interface, the alveolar epithelium, the capillary membrane fibres, the capillary endothelium and eventually the cell membrane of the red blood cell travelling in the capillary [24, 25].

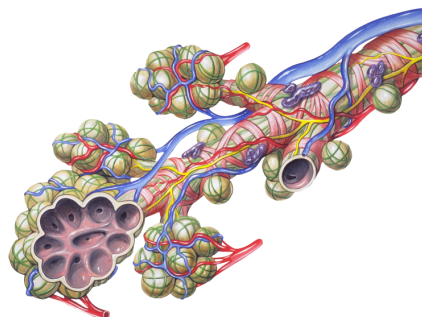


Figure 2.1: Spherical alveoli at the end of a bronchiole [26].

2.2 Lung Surfactant

Pulmonary surfactant is a mixture of lipids and proteins lining the interior of the alveoli [1]. It forms a monomolecular membrane at the liquid–air interface in the lung and thus separates the inhaled air from the circulation [1]. A simplification of this interface is represented in Fig. 2.2. In addition to alveoli, lung surfactant is also present in bronchioles and small airways [27]. The main function of this nanometre-scale membrane is to reduce the surface tension at the liquid–air interface during exhaling and thus prevent the alveoli from collapsing at the end of the respiratory cycle [2]. This property is believed to be mainly due to the principal component of this monolayer, dipalmitoylphosphatidylcholine (DPPC) [15].

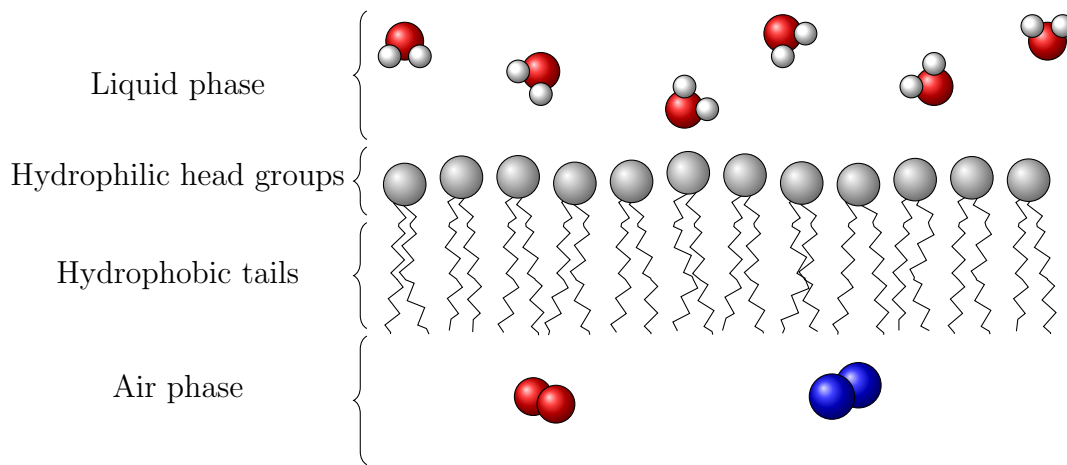


Figure 2.2: Schematic illustration of the mono-molecular layer at the liquid–air interface.

What happens at the surfactant layer during the breathing cycle is not completely understood [28]. An earlier view suggested that the volume of the alveoli remained constant [29] but later studies found out that their size changes during during exhaling and inhaling [30]. One view states that the surfactant is always at very low tension which corresponds to a small area per molecule. During the inhalation step the alveoli increase in size and the lipids required to maintain the small area per lipid are obtained from a lipid reservoir of some kind, residing in the close vicinity of the monolayer [31–34].

Another possibility is that the surfactant behaves as a plastic bag with very low interfacial tension that prevents its collapse even when not filled with air. The area of the monolayer is constant and the shape might change drastically during the breathing cycle. The difference between the two views is mainly on whether the lipid reservoir is a continuous part of the surfactant folded out of the monolayer or whether it is formed by separate bilayer aggregates [31–33, 35]. Scanning force microscopy studies have shown that both mechanisms might be possible and the

form of the reservoir could depend on the surfactant proteins B and C (SP-B and SP-C) [31, 36] with cholesterol stabilizing the bilayer parts of the folds formed in the presence of SP-C [37].

Third view states that the number of lipid molecules at the interface is constant and when the volume of an alveolus changes, the monolayer changes its compression state and thus both the area per lipid and surface tension change [4]. However, since the condensed monolayer has low compressibility [38], the effect of stretching might be smaller than suggested [15]. Therefore, it is possible that all these phenomena occur cooperatively [39, 40] and their individual contributions cannot be precisely determined.

The functionality of the surfactant is explained by the surface pressure–area isotherm an outline of which is presented in Fig. 2.3. It indicates that the surface pressure is raised up to a value of about 70 mN/m at high levels of compression. This pressure corresponds to the surface tension of water and indicates that the surface tension of the lung surfactant itself reaches values close to zero at small molecular areas before collapsing due to further compression. The shape of the isotherm also explains why smaller alveoli do not collapse and give out air to larger ones when connected to the same airway but rather keep their sizes equal [41]. The phases of the lung surfactant are also explained in Fig. 2.3. At low molecular areas, lipids arrange in the liquid condensed (LC) phase while at high molecular areas they prefer the liquid expanded (LE) phase. Between them a coexistence phase is observed. At very high molecular areas the surfactant turns into a two-dimensional gas and in the other end extensive compression induces first a gel-like state after which the monolayer collapses as lipids fold out from the monolayer to form bilayer structures.

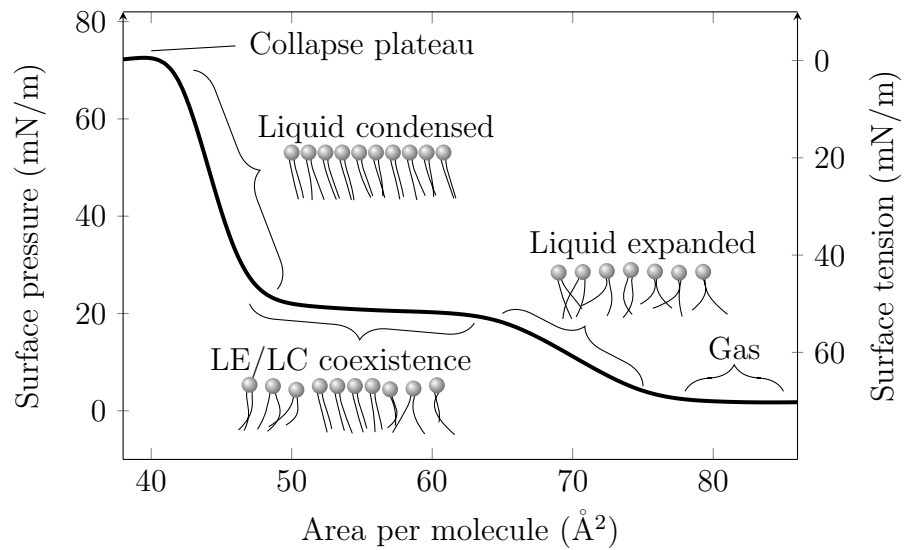


Figure 2.3: Example of a pressure–area isotherm.

The surfactant also functions as a pulmonary host defence system [42] and reduces the muscular work required for breathing in addition to various other tasks [43, 44]. Recent experimental evidence has suggested that the composition of lung surfactant is actually quite complex, and in addition to various protein components, several different types of lipids are required for a fully functional surfactant [2]. These include unsaturated PC and PG lipids as well as cholesterol.

The most abundant class of phospholipids is the PC lipids that together make around 80–90% of the lipid content of the surfactant [45, 46]. More than half of these PC lipids are disaturated with DPPC accounting for approximately 40% of the total lipid content [45, 46]. PG lipids make 5–10% of phospholipids and cholesterol comprises most of the neutral lipids [45, 46]. The composition of lung surfactant is different from other tissues such as cell membranes as it has relatively low concentrations of sphingomyelin and phosphatidylethanolamine. The protein components in lung surfactant are named surfactant protein A to D with surfactant protein B bearing the most critical physiological influence. It plays a role in the reduction of surface tension [47] and the formation of the surfactant [48], whereas A and D have an immunological role [49].

The structure of an alveolus is presented with detail in Fig. 2.4. After being synthesized by type II alveolar cells [50], phospholipids that will eventually fuse to the pulmonary surfactant are stored in lamellar bodies that carry the phospholipids to the alveoli as tightly packed bilayers [51]. In the alveoli the lipids form tubular myelin which is further absorbed into the air–water interface to merge into the already existing surfactant [51].

2.3 Lipid Structures below the Lung Surfactant

Since the pulmonary surfactant is only the first of various membrane structures that oxygen has to pass in order to reach the capillaries, it is likely that other structures also play a role in oxygen transport. It is a natural assumption that oxygen takes the route through which its permeation is most efficient. The very recent discussion on the possible structures of the lipid reservoir has also induced theories on oxygen permeation below the surfactant monolayer [53, 54].

In their theoretical study, Åberg et al. compared two possible models for the lipid reservoir [53]. The first and more likely structure was a special crossed layers of parallels (CLP) model suggested for tubular myelin by Larsson et al. [55]. This structure is depicted on the right in Fig. 2.5. The comparison was performed against a simple model of aligned bilayers which probably also exists below the monolayer to some extent [53]. Their conclusion was that the CLP model enhances oxygen transport due to oxygen, being able to diffuse partly through the membrane interior instead of permeating solely through the bilayers as suggested by the arrows on

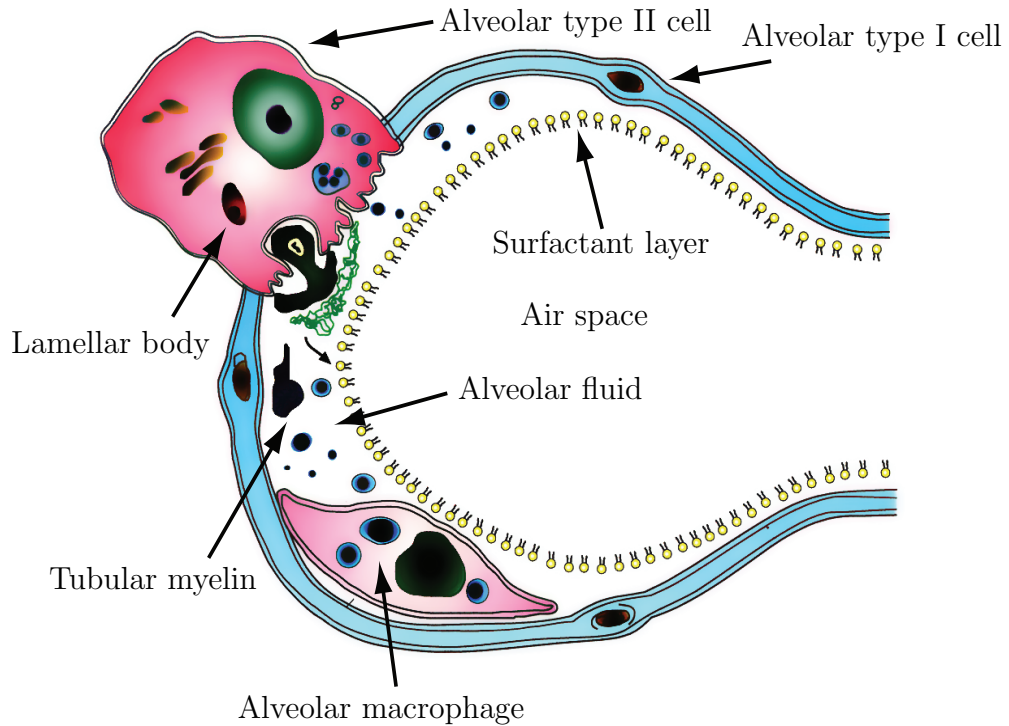


Figure 2.4: Structure of an alveolus, modified from [52].

the right side of 2.5. Furthermore, if the tubular structure is in direct contact with the monolayer as suggested by Kashchiev and Exerowa, then the oxygen does not necessarily have to pass through the monolayer at all [34].

In another recent experimental study, Olmeda et al. found out that the rate of permeation of oxygen through the surfactant film structure was enhanced when the concentration of phospholipids at the air–water interface was higher than the level required for covering the whole surface area [54]. They also noticed that the addition of surfactant proteins further increased oxygen transport through the membrane system. This suggests that surfactant proteins might form an interconnected membrane structure in which oxygen can travel through the bilayer cores [54]. This structure is depicted on the left side of Fig. 2.5 with solid arrows representing the movement of oxygen from one bilayer system to another through a channel formed by surfactant protein B. These channels are drawn in black. Surfactant protein C is not shown in the picture but it is considered to have a role in anchoring the bilayer systems together. The possible role of SP-B in channel formation in the tubular myelin structure was also discussed in a study by Pérez-Gil [56] and it might be the link between these two proposed models. The real structure of tubular myelin is possibly

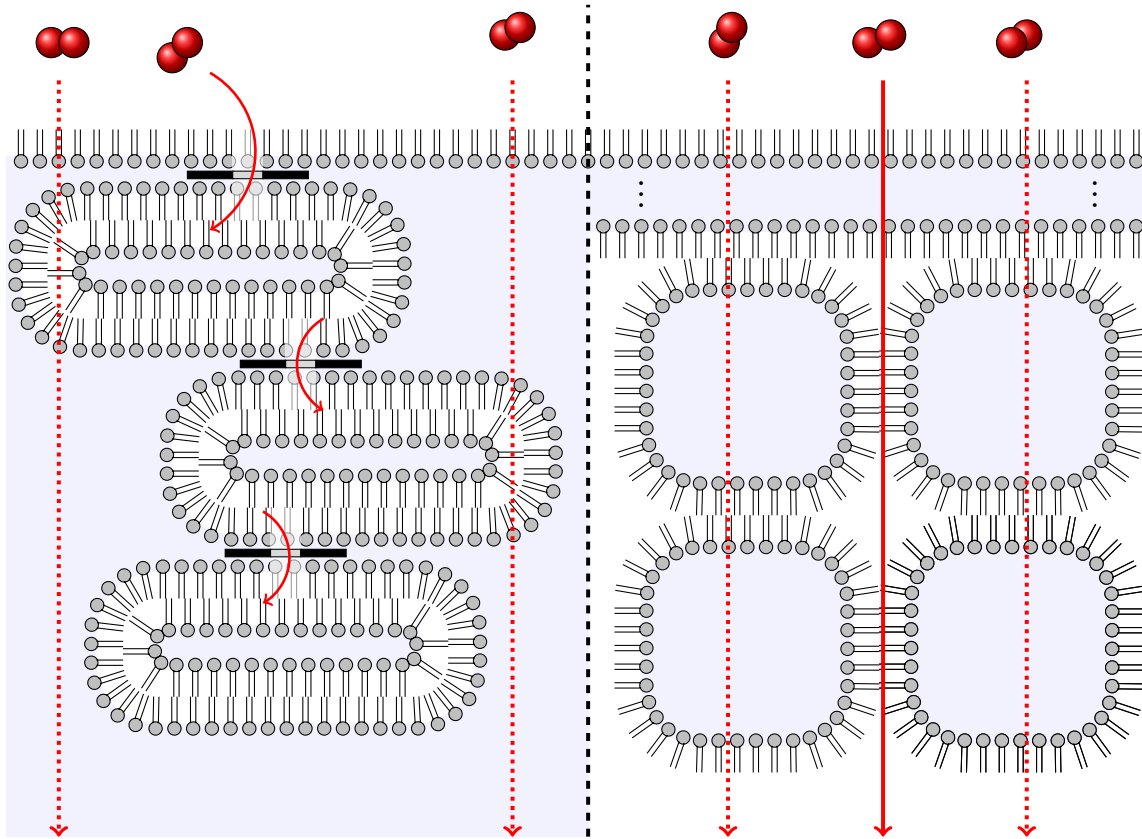


Figure 2.5: Possible membrane structures and pathways for oxygen permeation below lung surfactant. Left: Protein-induced pathways through disc-like bilayer structures suggested by Olmeda et al. [54]. Channels formed by SP-B between lipid layers are drawn in black. Right: The CLP model for the tubular myelin suggested by Åberg et al. [53]. The dots indicate that it is possible that the tubular structure begins right at the interface but this idea is still under debate.

a CLP-like structure in which the channels allowing a continuous path for oxygen are formed by the surfactant protein B. This might explain the effect of SP-B on permeation [54].

2.4 Structure and Function of Lipids

Lipids are a very diverse group of organic molecules. A lipid can be defined to be a naturally occurring molecule that is only marginally soluble in water and well soluble in non-polar organic solvents [57]. Phospholipids, fats, oils, waxes and cholesterol are examples of the wide variety of the lipid family [58]. Lipids play key roles in all living beings as they are the main components of biological membranes such as the plasma membrane and participate in the energy storage within cells [58]. Some hormones such as estrogen and testosterone are also classified as lipids as are some vitamins [58].

Lipids are either hydrophobic or amphiphilic molecules. The structure of an amphiphilic lipid consists of both a polar and a non-polar part [18]. This property enables them to form membrane structures at both liquid–air and liquid–liquid interfaces in the form of either a single layer of molecules or two layers of molecules with their hydrophobic parts in the two layers facing each other [18].

Examples of the former type, monolayers, can be found on the surface of an eye and in lung surfactant. Structures of the latter type, bilayers, can be found in various cellular membranes. In addition to planar membranes, lipids display various other ways to aggregate such as cubic, hexagonal and rhombic phases, inverted and planar micelles and vesicles [59, 60]. This morphology is dependent on various things such as temperature, saturation of the lipid tails, water content and various parameters related to the shape of the lipids [59].

All membrane-like structures in living cells are mainly composed of phospholipids because their structure is ideal for experiencing hydrophobic interactions when dissolved into water. All systems are driven towards the state of minimum free energy. In the temperature range of living systems this minimum value is obtained when the phospholipids are located so close to each other that there is no space for the water molecules to reside between them. Organising in the aforementioned structures such as mono- or bilayers minimizes both the reduction in entropy caused by the regular ordering of the water shell around the lipids and the contact area between the water and the non-polar parts of the lipids [60, 61].

We have studied membranes consisting of four different lipid species. Three of these components are phospholipids. Their structure is composed of a polar head group, a glycerol backbone and two hydrocarbon tails referred to as acyl chains [18]. This structure is explained in Fig. 2.6.

Cholesterol is part of the sterol group, a subgroup of steroids [58]. Sterols are important components in membranes and in intracellular signalling [62–64]. The structure of cholesterol is depicted in Fig. 2.7.

2.5 Lipids of the Pulmonary Surfactant

DPPC is a saturated lipid with a positively charged amino head group and two acyl chains formed of palmitic acid [65]. The tails are thus 16 carbon atoms long [65]. Palmitoyloleoylphosphatidylcholine (POPC) slightly differs from DPPC as it has a double bond in one of the hydrocarbon tails and it is thus unsaturated [65]. The chain with the double bond is 18 carbon atoms long and formed of oleic acid [65]. DPPC and POPC are classified by their head group to be members of the phosphatidylcholine (PC) lipids that are the main phospholipid components in membrane structures in mitochondria, microsomes, lysosomes, nuclei, and the Golgi apparatus [66]. PC lipids also make the majority of the phospholipid molecules that

constitute the plasma membrane surrounding cells in whole [66].

Palmitoyloleoylphosphatidylglycerol (POPG) has a glycerol head group, which is a triol with two free hydroxyl groups when bound to the phosphate group [65]. These hydroxyl groups have some tendency to form intra- and intermolecular hydrogen bonds [67]. The hydrocarbon tails of POPG are the same as those of POPC as the name suggests [65]. The special role of POPG in lung surfactant is to increase the fluidity in the environment of DPPC [68].

The structure of cholesterol is significantly different from other components in our model membrane. A cholesterol molecule consists of a planar and rigid hydrocarbon ring structure and a polar head group with a polar hydroxyl group so it is also an amphiphile [60]. Cholesterol can be found in many types of membranes. For instance roughly about 20 mass per cent of the plasma membrane is composed of cholesterol [69]. A cholesterol molecule is shorter and has a smaller cross-sectional area than the phospholipid molecules used in this study. Experimental and computational studies on cholesterol have revealed the importance of cholesterol in biological membranes as it makes the membranes stiffer, increases lipid ordering, and reduces the diffusive motion of other lipids in the fluid phase [70, and references therein].

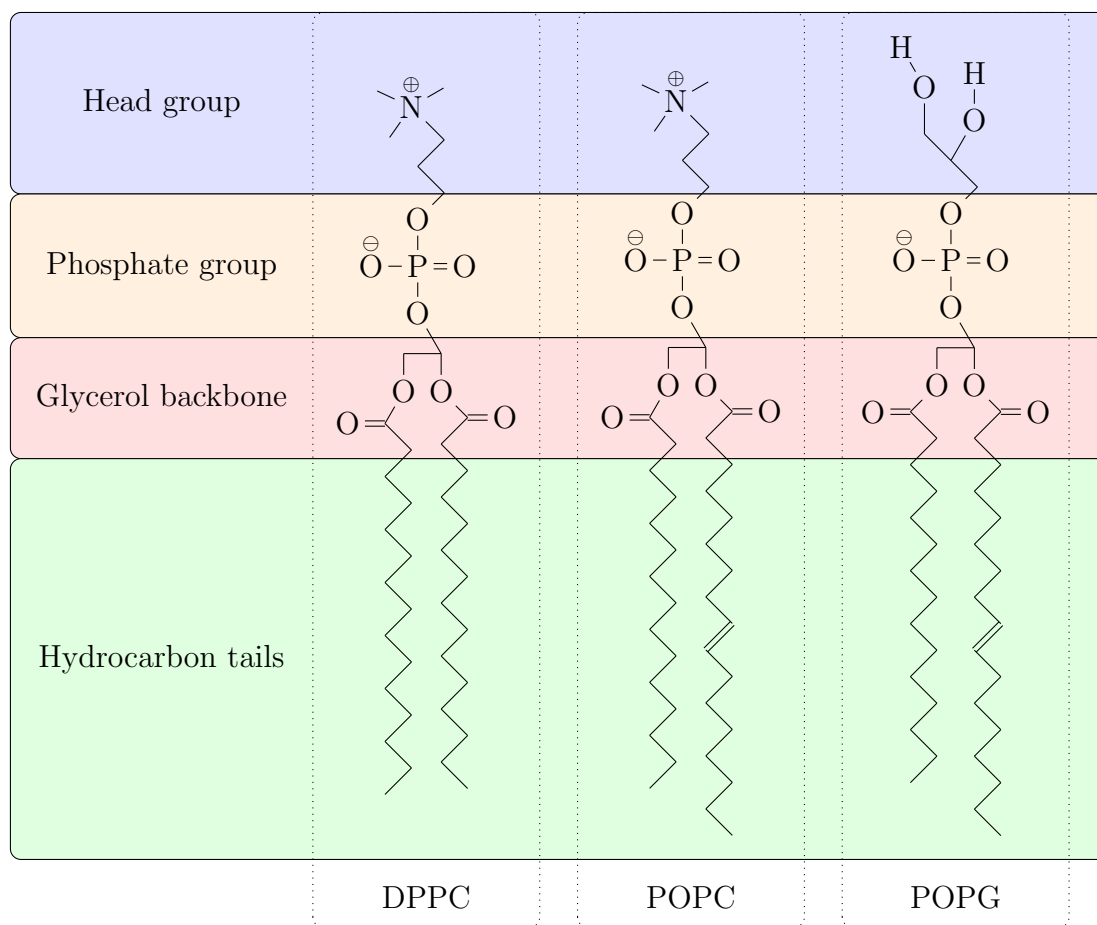


Figure 2.6: The structures of the phospholipids employed in this study. The important parts to which we will make references in the text below are labelled.

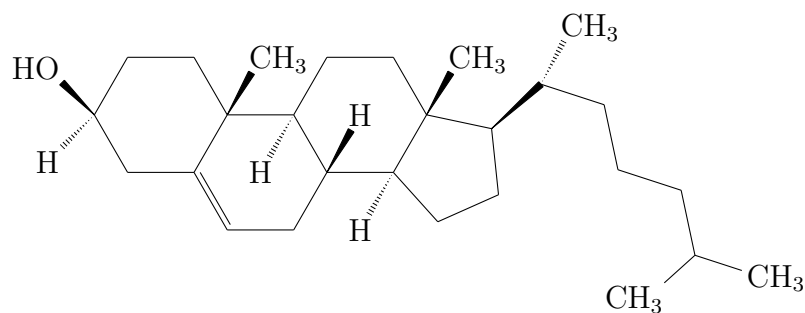


Figure 2.7: The structure of a cholesterol molecule.

3. THERMODYNAMIC INTEGRATION METHOD

In this chapter we discuss the thermodynamic integration technique which can be employed in computer simulations to calculate free energy changes along non-physical pathways. It is employed in the development of the model for the oxygen molecule to be used in permeation studies later in this work. The potential functions that are used in the thermodynamic integration method are listed in the end of the chapter. We begin by introducing the theoretical background of thermodynamic cycles and partitioning ratios that connect the values obtained from these special kinds of simulations to those available in literature.

3.1 Partitioning and Free Energy

Partitioning of molecules between different solvents is a good and common method for validating a force field. It is of large importance when interfaces between different solvents are being studied, as is the case in this work. The partition ratio for a molecule describes the ratio at which it partitions into the two phases. It is defined as

$$P = \frac{c_{\text{organic}}}{c_{\text{water}}}, \quad (3.1)$$

where P is the partition ratio, also known as the distribution constant, c stands for concentration, and the subscripts refer to the organic and aqueous phases [71]. Partition ratios are frequently used in pharmaceutical context to describe the distribution of a drug in a human body. A combination of octanol and water is usually employed in the experimental determination of partition ratios as these form a good model for the partitioning between the cytosol and lipid membranes in living organisms [72].

The partition ratio is a reaction quotient for the process of the solute molecule moving from the aqueous phase to the organic phase. Thus when the system is at equilibrium, P can be thought of as an equilibrium constant and directly linked to the free energy change of the solvent molecule moving from the aqueous phase to the organic one via the relation

$$\Delta G_{\text{water} \rightarrow \text{organic}} = -RT \ln P, \quad (3.2)$$

where $\Delta G_{\text{water} \rightarrow \text{organic}}$ is the excess Gibbs free energy change of the transfer process,

R the gas constant, and T temperature.

When we want to calculate the partition ratio between two solvents, we can form a cycle as represented in Fig. 3.1 and employ Hess’s law which states that since free energy is a state function, the total free energy of a process is the same regardless of whether it is performed in a single step or in many smaller steps. Thus we can calculate the free energy of a process of moving the solvent molecule from one solvent to the other by taking the reverse path around the circle and summing the excess free energies encountered along this path as indicated in Fig. 3.1.

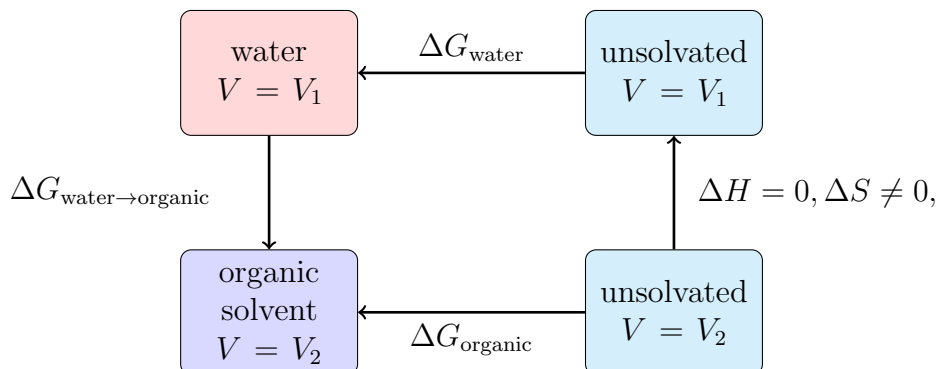


Figure 3.1: The cycle used for the calculation of the free energy of moving a solvent molecule from water to organic solvent. Unsolvated molecules are, in terms of computational methodology, molecules without long range interactions.

In order to calculate the value for $\Delta G_{\text{water} \rightarrow \text{organic}}$ we have to subtract the term ΔG_{water} from $\Delta G_{\text{organic}}$ and take into account also the possible volume-related entropy difference between the systems with unsolvated particles. Since we are only monitoring the free energy changes in the molecule being solvated, the “unsolvated” molecule in Fig. 3.1 has no long range interactions and therefore in terms of computational methodology it is identical to a dummy molecule in a solvent.

The free energy difference of the dummy molecule between the two phases consists of two parts. The enthalpic part is zero since the dummy molecules do not interact with any other particles. Another requirement is that the contributions arising from their internal degrees of freedom are neglected. This is a general assumption often employed in studies with free energy cycles [73, 74] and can be avoided by the use of modern simulation packages that allow separate coupling of each interaction type.

In addition to enthalpy, we must also consider the entropic part. The entropy change related to the process of transferring a dummy molecule from one environment with volume V_1 to another with volume V_2 can be estimated with the Sackur–Tetrode equation. This equation is valid for monatomic classical ideal gases at constant temperature. The change is $\Delta S = R \ln(V_2/V_1)$ and its contribution to the free energy is $-T\Delta S$.

3.2 Thermodynamic Integration

In the isothermal–isobaric ensemble, that is when the pressure, temperature and the number of particles of the system are constant, the equilibrium of the system is obtained when the Gibbs free energy

$$G = U + pV - TS \quad (3.3)$$

reaches its minimum value. Internal energy U can be obtained easily from simulations as it is just the function of the positions and velocities of the particles, that is, of the phase space variables [75]. However, the dependency of entropy and thus also the Gibbs free energy are more complicated and are related to the volume of the phase space accessible to the system and thus cannot be measured directly from computer simulations [75].

One method that allows us to calculate free energy differences is called thermodynamic integration. This approach is applied to both experimental and computational problems and the key point is to integrate the differential equations linking the derivatives of free energy to some measurable quantity [75]. Thus we can form a reversible path between the two states whose free energy difference we want to measure. This value is then obtained by measuring the change in thermal variables and integrating them along the taken path [75].

If one wants to calculate absolute free energy values, a reference state is required. However, fixing either of the end points of the integration is a challenging task as an analytic formula for the free energy of a system is known only for very few systems such as an ideal gas or an Einstein solid. Yet, if one is interested only in free energy differences as is the case in this work, such reference point is not needed.

In computational chemistry we have more freedom in choosing the variables for the integration as they do not need to be any measurable real world quantities [75]. We can directly employ all the variables in our potential function and even introduce new scaling parameters for the interactions [75]. This way we can turn desired types of interactions on or off during a simulation either separately or simultaneously [75].

We shall label the reference state with A and the system of interest with B . These correspond to the values 0 and 1 of the coupling parameter λ , respectively. Here we do not consider the linear dependence of the coupling parameter as this is not always employed. The Hamiltonian $\mathcal{H}(\mathbf{r}^N, \mathbf{p}^N, \lambda)$ has the boundary values

$$\mathcal{H}^A = \mathcal{H}(\mathbf{r}^N, \mathbf{p}^N, 0) \quad (3.4)$$

$$\mathcal{H}^B = \mathcal{H}(\mathbf{r}^N, \mathbf{p}^N, 1), \quad (3.5)$$

where \mathbf{r}^N and \mathbf{p}^N stand for the positions and the momenta of the N particles

comprising the system. The partition function Δ of this system at any value of λ is given by

$$\Delta(\lambda) = \frac{1}{V^0 h^{3N} N!} \times \int_0^\infty \int_{-\infty}^\infty \int_{D(V)} \exp(-\beta\Omega) d\mathbf{r}^N d\mathbf{p}^N dV, \quad (3.6)$$

where N is the number of particles, V^0 a normalisation constant and h Planck's constant [76]. The domain over which the integration with respect to \mathbf{r}^N is performed is labelled with $D(V)$, β is short for $(k_B T)^{-1}$ and

$$\Omega = \mathcal{H}(\mathbf{r}^N, \mathbf{p}^N, \lambda) + pV(\lambda). \quad (3.7)$$

Gibbs free energy can be obtained by definition from the partition function as

$$G(\lambda) = -RT \ln \Delta(\lambda). \quad (3.8)$$

The free energy change can be trivially written as

$$\Delta G = \int_0^1 \frac{\partial G(\lambda)}{\partial \lambda} d\lambda, \quad (3.9)$$

and thus inserting Eq. (3.8) into Eq. (3.9) we obtain

$$\Delta G = -RT \int_0^1 \frac{\partial \ln \Delta(\lambda)}{\partial \lambda} d\lambda \quad (3.10)$$

$$= \int_0^1 \frac{-RT}{\Delta(\lambda)} \frac{\partial \Delta(\lambda)}{\partial \lambda} d\lambda. \quad (3.11)$$

Next we calculate the derivative of the partition function (Eq. (3.6)) with respect to λ to be

$$\frac{\partial \Delta(\lambda)}{\partial \lambda} = \frac{1}{V^0 h^{3N} N!} \int_0^\infty \int_{-\infty}^\infty \int_{D(V)} \frac{\partial}{\partial \lambda} \exp(-\beta\Omega) d\mathbf{r}^N d\mathbf{p}^N dV. \quad (3.12)$$

By employing the chain rule for differentiation we obtain

$$\frac{\partial \Delta(\lambda)}{\partial \lambda} = \frac{-\beta}{V^0 h^{3N} N!} \int_0^\infty \int_{-\infty}^\infty \int_{D(V)} \frac{\partial \Omega}{\partial \lambda} \times \exp(-\beta\Omega) d\mathbf{r}^N d\mathbf{p}^N dV. \quad (3.13)$$

Substituting Eq. (3.13) back into Eq. (3.11) we end up with

$$\frac{\partial G}{\partial \lambda} = \frac{N_A}{V^0 h^{3N} N!} \frac{1}{\Delta(\lambda)} \int_0^\infty \int_{-\infty}^\infty \int_{D(V)} \frac{\partial \Omega}{\partial \lambda} \times \exp(-\beta\Omega) d\mathbf{r}^N d\mathbf{p}^N dV, \quad (3.14)$$

where N_A is Avogadro's constant. This can be rearranged into

$$\frac{\partial G}{\partial \lambda} = \frac{N_A}{V^0 h^{3N} N!} \int_0^\infty \int_{-\infty}^\infty \int_{D(V)} \frac{\partial \Omega}{\partial \lambda} \times \frac{\exp(-\beta \Omega)}{\Delta(\lambda)} d\mathbf{r}^N d\mathbf{p}^N dV. \quad (3.15)$$

We now notice that this is an equation for the expectation value for the partial derivative term as each of the terms in the sum is weighted by its exponential probability term and the whole equation is normalized by the partition function. Thus we can write Eq. (3.15) simply in the form of

$$\frac{\partial G}{\partial \lambda} = N_A \left\langle \frac{\partial [\mathcal{H}(\mathbf{r}^N, \mathbf{p}^N, \lambda) + pV(\lambda)]}{\partial \lambda} \right\rangle, \quad (3.16)$$

and plugging this result into Eq. (3.9) we finally end up with

$$\Delta G = N_A \int_0^1 \left\langle \frac{\partial [\mathcal{H}(\mathbf{r}^N, \mathbf{p}^N, \lambda) + pV(\lambda)]}{\partial \lambda} \right\rangle_\lambda d\lambda. \quad (3.17)$$

This key result allows us to easily calculate the free energy differences in simulations as we only need to know the dependence of the internal energy and possibly volume on the coupling parameter. The free energy difference between systems A and B is calculated simply by integrating the ensemble average along the coupling parameter.

A more accurate value of free energy can be obtained if it is divided into contributions from different terms in the potential function [77]. The potential energy function inside Eq. (3.17) can be separated into components in the form of

$$\begin{aligned} \left\langle \frac{\partial \mathcal{H}(\mathbf{r}^N, \mathbf{p}^N, \lambda)}{\partial \lambda} \right\rangle_\lambda &= \left\langle \frac{\partial \mathcal{H}_{\text{bond stretching}}(\mathbf{r}^N, \mathbf{p}^N, \lambda)}{\partial \lambda} + \dots \right. \\ &\quad \left. + \frac{\partial \mathcal{H}_{\text{Coulombic}}(\mathbf{r}^N, \mathbf{p}^N, \lambda)}{\partial \lambda} + \dots \right\rangle_\lambda, \end{aligned} \quad (3.18)$$

where we take into account all bonded and all non-bonded interactions. Now the integration can be performed for each term separately as

$$G(\lambda = 1) - G(\lambda = 0) = \Delta G_{\text{Bond stretching}} + \dots + \Delta G_{\text{Coulombic}} + \dots \quad (3.19)$$

$$\begin{aligned} &= N_A \int_{\lambda=0}^{\lambda=1} \left\langle \frac{\partial \mathcal{H}_{\text{bond stretching}}(\lambda)}{\partial \lambda} \right\rangle_\lambda d\lambda + \dots \\ &\quad + N_A \int_{\lambda=0}^{\lambda=1} \left\langle \frac{\partial \mathcal{H}_{\text{Coulombic}}(\lambda)}{\partial \lambda} \right\rangle_\lambda d\lambda + \dots \\ &\quad + N_A \int_{\lambda=0}^{\lambda=1} \left\langle \frac{\partial pV(\lambda)}{\partial \lambda} \right\rangle_\lambda d\lambda. \end{aligned} \quad (3.20)$$

The contributions from different terms are not meaningful since they are not state functions and thus only the sum should be considered to bear any physical relevance [75].

3.3 Potential Functions for Thermodynamic Integration

In the following section, we list the formulas which are employed in the GROMACS simulation package [78, 79] to calculate the derivatives of the potential function terms with respect to the coupling parameter λ . The averages of these derivatives at different values of λ are needed for obtaining the free energy difference as presented in Eq. (3.20). The values one gets from the simulation are not actually related to free energy changes during the simulation since that would require λ to change somehow. Instead, the terms in the potential function are differentiated analytically with respect to λ and the rate of change is obtained by plugging in the variables that are available in an equilibrium simulation.

We employ the thermodynamic integration method in solvating oxygen molecules into two solvents. Thus we are not interested in the internal contributions to the free energy of solvation but rather in the interactions between the oxygen molecule and the solvent molecules. These interactions are represented by the non-bonded terms in the potential function.

In the GROMACS simulation package, the non-bonded interactions can be interpolated either linearly or via soft-core interactions. In this study we have used the soft-core interpolation of the Coulomb and Lennard-Jones potentials as we make particles disappear from the system and the values of λ near 0 or 1 might cause singularities if simple linear interpolation was employed [78]. All the following dependencies are the standard ones used in GROMACS.

The linearly scaled formula for the Coulomb interaction $\mathcal{H}_{\text{Coulombic}}$ is given by

$$\mathcal{H}_{\text{Coulombic}}(\lambda) = \frac{1}{4\pi\epsilon_0\epsilon_r r_{ij}} \left((1-\lambda)q_i^A q_j^A + \lambda q_i^B q_j^B \right), \quad (3.21)$$

where q_i^A and q_j^A are the charges on particles i and j in the state with $\lambda = 0$ and q_i^B and q_j^B are the respective values for the state with $\lambda = 1$. The slope is obtained through differentiation as

$$\frac{\partial \mathcal{H}_{\text{Coulombic}}(\lambda)}{\partial \lambda} = \frac{1}{4\pi\epsilon_0\epsilon_r r_{ij}} \left(-q_i^A q_j^A + q_i^B q_j^B \right). \quad (3.22)$$

The linear interpolation version of the Lennard-Jones potential, $\mathcal{H}_{\text{Lennard-Jones}}$, is

given by

$$\mathcal{H}_{\text{Lennard-Jones}}(\lambda) = \frac{\left((1-\lambda)C_{(12)}^A + \lambda C_{(12)}^B\right)}{r_{ij}^{12}} - \frac{(1-\lambda)C_{(6)}^A + \lambda C_{(6)}^B}{r_{ij}^6}, \quad (3.23)$$

where $C_{(12)}^A$ and $C_{(6)}^A$ are the Lennard-Jones parameters in the initial state A with $C_{(12)}^B$ and $C_{(6)}^B$ being the respective values in the final state B . The derivative is obtained in the form of

$$\frac{\partial \mathcal{H}_{\text{Lennard-Jones}}(\lambda)}{\partial \lambda} = \frac{C_{(12)}^B - C_{(12)}^A}{r_{ij}^{12}} - \frac{C_{(6)}^B - C_{(6)}^A}{r_{ij}^6}. \quad (3.24)$$

The soft-core potential in GROMACS is a modification from the normal linear interpolation in which the regular potentials are shifted to avoid singularities. The general formula for the soft-core potential is given by

$$\mathcal{H}_{\text{soft-core}}(r_{ij}, \lambda) = (1-\lambda)\mathcal{H}^A(r_A) + \lambda\mathcal{H}^B(r_B), \quad (3.25)$$

where \mathcal{H}^A and \mathcal{H}^B are the potential functions of the A and B states and r_A and r_B are given by

$$r_A = (\alpha\sigma_A^6\lambda^s + r_{ij}^6)^{\frac{1}{6}} \text{ and} \quad (3.26)$$

$$r_B = (\alpha\sigma_B^6(1-\lambda)^s + r_{ij}^6)^{\frac{1}{6}}. \quad (3.27)$$

The soft-core parameter is labelled with α and s is the soft-core power of λ . The force derived from this potential is obtained in the form

$$F_{\text{soft-core}}(r_{ij}, \lambda) = -\frac{\partial \mathcal{H}_{\text{soft-core}}(r_{ij})}{\partial r} \quad (3.28)$$

$$= (1-\lambda)F^A(r_A) \left(\frac{r_{ij}}{r_A}\right)^5 + \lambda F^B(r_B) \left(\frac{r_{ij}}{r_B}\right)^5, \quad (3.29)$$

where the normal forces of the A and B states are labelled as F^A and F^B . The dependence of the potential on the coupling parameter is given as

$$\begin{aligned} \frac{\partial \mathcal{H}_{\text{soft-core}}(r_{ij}, \lambda)}{\partial \lambda} &= -V^A(r_A) + V^B(r_B) \\ &+ \alpha \frac{s}{6} \left(-(1-\lambda)\lambda^{s-1}F^A(r_A)\sigma_A^6r_A^{-5} \right. \\ &\left. + \lambda(1-\lambda)^{s-1}F^B(r_B)\sigma_B^6r_B^{-5} \right). \end{aligned} \quad (3.30)$$

4. THEORY OF PERMEATION

We begin this chapter by describing some general properties of permeation processes and list factors that are found to affect the rates of these processes. We then introduce a simple theoretical description of membrane permeation, the homogeneous solubility–diffusion model and its refinement, the inhomogeneous version of the theory. Finally, we review the specific case of permeation of oxygen through lipid membranes and monolayers.

4.1 General Properties of Permeation Processes

Carefully regulated membrane transport processes are vital to all living organisms. These mechanisms are required when ions or molecules need to pass through cell membranes or the membranes of different organelles. Permeation processes through biological membranes can be essentially categorized into two: those that require direct energy input and those that occur passively without an external energy source [80].

Passive transport can take place in two ways. In simple diffusion the particles move along their concentration gradient through the membrane without any regulatory mechanism via the so-called basal pathway [81]. However, for many large or charged molecules this is not possible and thus they diffuse through the membrane with aid from special carrier or channel proteins [80]. Active transport methods such as ion pumps require energy that is usually provided by ATP hydrolysis [80].

The range of experimentally measured permeability coefficients of small non-electrolyte permeants is very large spanning at least seven orders of magnitude [8]. Three important factors of the permeant that affect its permeability are its size, hydrophobicity/hydrophilicity, and shape [8]. The permeability of smaller molecules is found to have a very steep size dependency which can be explained either by the solubility part [82, 83], diffusion part [84], or both [85], but not by hydrophobicity [84].

Hydrophobicity has been found to affect the solubility part of the permeation process. This is verified by the strong correlation between permeability and partitioning coefficients in a hydrophobic solvent [84]. The effect of shape has been found to be small compared to the effect of size [85]. Non-spherical permeants have not shown anomalous effect on solubility [84, 85]. However, shape likely affects diffusion

as non-spherical molecules are assumed to diffuse slower than spherical ones.

In addition, permeability is affected by various properties of the membrane. These include the area per lipid for which a linear dependence has been found in the case of water [86]. The phase of the membrane has been seen to also have a large influence. The permeability coefficients of the membrane in crystalline phase were found to be two orders of magnitude smaller than those of the membrane in fluid phase [87]. A molecular dynamics study on a coarse-grained PC bilayer showed that a rise in water permeability at phase change temperature is associated with both a jump in area per molecule and increased free volume fluctuations [88].

The ordering of the hydrocarbon tails caused by cholesterol molecules has the effect of speeding up the permeation process in the hydrocarbon tail part but slowing it down in the head group region. In a study of hexadecane molecules modelling a monolayer without the head groups, cholesterol was seen to speed up oxygen diffusion by a factor of 2 [9]. In a study by Subczynski et al. the total rate of oxygen permeation was shown to slow down due to the addition of cholesterol even though the rate was higher in the acyl chain region [5]. The effect of cholesterol has a similar effect on water [86, 89], ions and larger neutral molecules [90].

According to the homogeneous solubility–diffusion model presented later in this chapter, permeabilities should depend linearly on the inverse of the thickness of the membrane. This relation verified earlier [91] has been recently questioned by Mathai et al. in their study on water permeation [86] and in some situations either a small [92] or an exponential dependence has been suggested [7, 93, 94].

The raise of temperature has been seen to speed up the permeation rate of oxygen [5], and in the case of water an exponential dependence between permeability and temperature has been found indicating a thermally activated process [94, 95]. Permeabilities of different molecules have been observed to decrease exponentially with increasing surface pressure [3, 95, 96] even though in the LC phase the permeability might be independent of surface tension [94].

Proteins might also have an effect on the permeation of some molecules [87]. Bemporad et al. found that the correlation of free volume and diffusion coefficient was not strong [83]. According to Al-Abdul-Wahid et al., however, permeation of oxygen into micelles is energetically not as favourable as partitioning into vesicles due to the interior of a micelle having less voids and being more ordered due to the cylindrical shape of the lipids [97]. Chain branching lowers the permeability of lipid membranes [98]. This is found to be due to the decrease in diffusion coefficients connected to the reduced amount of free volume in the membranes [98].

There are various methods to experimentally determine the permeability coefficients. These include osmotic, NMR and radioactive tracer experiments and fluorescence techniques that measure the concentration of permeated particles [10, 12, 99–

101]. Oxygen permeation can also be measured with stop-flow methods [102], with electron paramagnetic resonance employing spin-labelled lipids [103] or peptides [104] and scanning electrochemical microscopy induced transfer [105]. Naturally the selection of the method depends on the type of membrane studied. Some refined and specific methods have recently been developed for measuring oxygen permeation in polymer films [100, 101].

4.2 Homogeneous Solubility–Diffusion model

The homogeneous solubility–diffusion model treats the permeation process through a membrane as a three-step process [106]. First, the permeating molecule is dissolved into the membrane phase from the medium surrounding it. Then it is diffused through the membrane and finally dissolved again on the other side of the membrane back to the original medium. This model was originally developed to describe permeation through polymer membranes but it has proved its usefulness also in describing permeation through lipid bilayers [81, 84, 91, 107, 108]. It is most fruitfully employed on small polar molecules [109].

Diffusion through the bilayer is considered to be the rate-limiting step of permeation. The bilayer is considered to be a homogeneous and isotropic medium with sharp boundaries. If all the effects of any interfacial barriers are neglected, we can write the permeability coefficient \mathcal{P} of the permeating particles in the form of

$$\mathcal{P} = \frac{PD}{d_c}, \quad (4.1)$$

where P is the bilayer/water partitioning coefficient, D the diffusion coefficient within the membrane core, and d_c the thickness of the membrane [110]. If we approximate the bilayer as oil, we recover what is referred to as the Meyer–Overton rule [111, 112] which states that the permeability coefficient is linearly dependent on the water/oil partitioning coefficient. The dependency of \mathcal{P} on both the partitioning coefficient [84, 108] and membrane thickness [91] has been verified by experiments.

4.3 Inhomogeneous Solubility–Diffusion model

It has been observed that in contrast to polymer membranes, lipid membranes are very inhomogeneous. Due to their relatively thin nature, the interface may cover up to 40% of the thickness of the membrane phase [113]. Their thickness also varies due to thermal fluctuations [114]. The interior of the membrane is also found to be inhomogeneous [115]. Thus it is pretty obvious that both diffusion rate and solubility depend on the position within the membrane. This has also been verified in various computational studies [8, 12, 92, 98, 99, 116].

Experimental support for this comes from various sources. Some solutes are found to face resistance at the interfaces [117, 118]. The distribution of non-polar alkyl solutes in alkane membranes is also inhomogeneous [119]. The density distributions, order parameters and diffusion in lipid membranes are different to those in bulk oil-like systems since there are also highly polar groups within the lipid bilayers that the oil solvents lack [120]. These groups are more ordered than the inner parts of lipid bilayers that resemble bulk alkanes. The higher surface density compared to bulk alkanes has also been observed to decrease the partitioning into the membrane phase [118, 119]. The discrepancies between experiments and the homogeneous solubility–diffusion theorem have been explained either by special types of diffusion or presence of structural defects [9].

These discrepancies with the homogeneous solubility–diffusion have led many to question its validity in describing permeation processes through biological membranes. An improvement over the homogeneous version is given in the form of an inhomogeneous solubility–diffusion model [11, 121]. In this model both the diffusion rate and the solubility of the permeating molecule into the membrane depend on its position within the membrane. This method has been successfully adapted in computer simulations but its validation is difficult in experimental studies. The free energy profiles that can be linked to solubility are hard to determine experimentally due to the large spatial variations of free volume, density and polarity [122].

Mitragotri et al. linked the parameters in the inhomogeneous solubility–diffusion theory to quantities that are readily obtained from simulations or experiments [123]. The parameters in their model are lipid chain density, free area and order parameter. The inhomogeneous nature of the membrane has been explained in terms of the “three-region model” [124] in which the three regions are the hydrocarbon core and the two head group regions at both ends of the membrane. A more detailed “four-region model” in which each leaflet consists of the four regions was first suggested by Marrink and Berendsen [12] and also discussed by others [8, 83, 99, 125–127]. The four regions of this model [8, 12], depicted in Fig. 4.1 are:

- **Region 1, “Bulk water”, 20–27 Å from the bilayer centre:** This region resembles that of bulk water with a slight perturbation induced by the low head group density and water molecules loosely bound to the choline head groups. The solubilities and diffusion coefficients might vary a bit but the total effect is very close to that of bulk water. For hydrophilic molecules, this region is not of much importance but hydrophobic molecules such as oxygen may experience the strongest resistance to permeation in this region.
- **Region 2, “Interface”, 13–20 Å from the bilayer centre:** A good approximation to this region is an effective medium with a high dielectric constant and viscosity. The high dielectric constant allows the hydrophilic molecules to have low excess free energy in this region. The high viscosity is due to the high density within the head group area of the membrane. Due to the large variety of different atoms in this region, it does not essentially resemble any bulk phase. The region has water molecules but they are bound to the lipid head group atoms and most of the glycerol backbones also reside in this region. The amount of free volume available in this region is the lowest.
- **Region 3, “Soft polymer”, 6–13 Å from the bilayer centre:** This region is responsible for the experimentally observed trends of permeation for polar molecules. It resembles a soft polymer, has a high density and hosts most of the anomalous effects in the permeation process. It also has the highest resistance for hydrophilic permeants because of their low solubility in this region. This region consists of the hydrocarbon tails and it has a density higher than liquid hexadecane.
- **Region 4, “Fluid decane”, 0–6 Å from the bilayer centre:** This region resembles a low-density alkane fluid such as decane and therefore the dielectric constant, viscosity and ordering are low in this region. Due to the low viscosity, diffusion in this region is fast and the resistance to permeation is small for both hydrophilic and hydrophobic permeants.

In the case of monolayers at the air–liquid interface the density of the tail groups eventually decreases to zero which never happens with bilayers as the density within them does not reach values under about 500 kg/m^3 . To better compare the regions of both monolayers and bilayers we introduce the fifth region of a monolayer whose properties might differ from the original four due to its very low density. A monolayer with its five regions is presented in Fig. 4.2.

In addition to the homogeneous and inhomogeneous versions of the solubility–diffusion mechanism, yet another theoretical model for describing permeation processes exists. The transient pore model [128, 129] has, however, been most successful

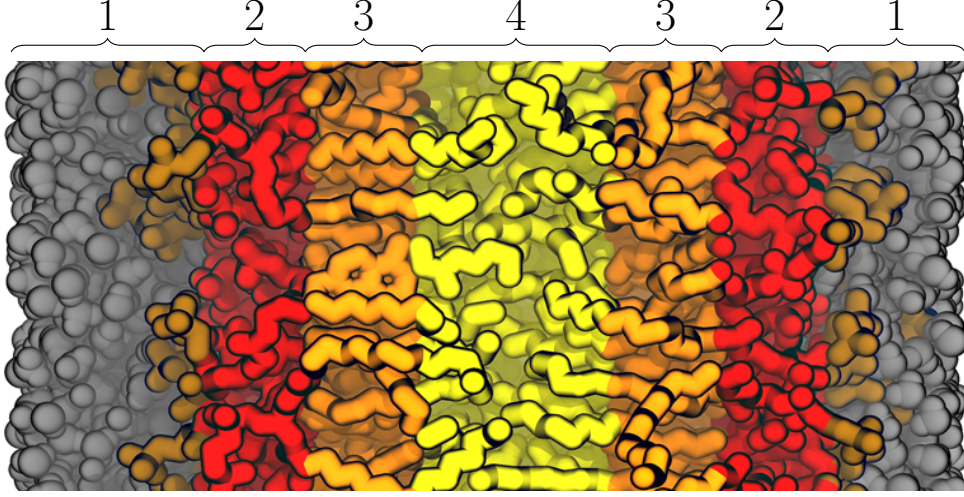


Figure 4.1: Regions in the “four region model”.

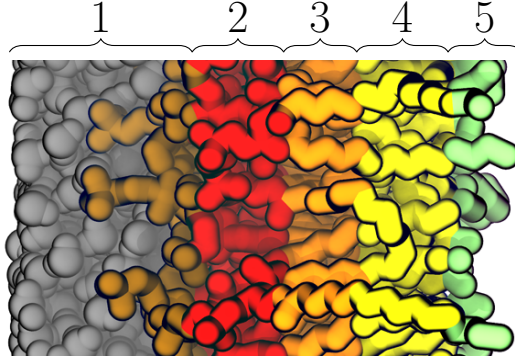


Figure 4.2: Regions in the “five region model”.

in describing the permeation of ionic solutes through thin membranes [91] and it is not therefore considered in this study.

4.3.1 Theoretical Description

Here we derive a formula for the permeation resistance suggested by the inhomogeneous description of the membrane. This theory can be related to quantities obtainable from computer simulations as presented first by Marrink and Berendsen [12]. Here we closely follow their derivation of the theory.

When a system is not in equilibrium and the motion of the particles is described as diffusion we can link the average velocity u to the concentration gradient or, as presented here, to the gradient of the chemical potential μ as

$$u = \langle v_j \rangle = -\frac{1}{\xi} \nabla \mu, \quad (4.2)$$

where ξ presents the friction coefficient of the diffusing particles and v_j is the speed of particle j of the examined type. The flux of the particles is obtained when we multiply this average speed by the concentration of the particles c and it is thus expressed as

$$J = cu = -\frac{c}{\xi} \nabla \mu. \quad (4.3)$$

We now employ the Einstein relation that links the diffusion coefficient of the particles, D , to the friction coefficient, ξ , as

$$D = RT/\xi, \quad (4.4)$$

where R is the universal gas constant and T the temperature. In the case of ideal solution for which $\mu = \mu^0 + RT \ln c$, combining Eqs. (4.3) and (4.4) results in the first of the Fick's laws of diffusion, $J = -D \nabla c$.

In the case of lipid membranes we can consider the direction of the normal of the membrane, usually labelled with z , to be the only direction in which a chemical potential may vary. Chemical potentials in the x and y directions are in contrast considered to be homogeneous. Thus we can employ Eq. (4.4) and write Eq. (4.3) in a form in which the chemical potential only depends on the z coordinate as

$$J_z(z) = -\frac{c(z)D(z)}{RT} \frac{d\mu(z)}{dz}. \quad (4.5)$$

Here we only consider cases in which the particles diffuse independently and encounter friction caused by the membrane. It is possible to obtain the dependence of the local concentration of the particles on location and time by employing the continuity equation for the concentration in the form of

$$\frac{dJ_z(z)}{dz} + \frac{dc(z)}{dt} = 0. \quad (4.6)$$

However, when the deviations from equilibrium are small, a steady-state solution is obtained in which the flux no longer has any spatial dependence. Thus we can integrate the derivative of μ versus z as calculated from Eq. (4.5) and obtain

$$\Delta\mu = \mu(z_2) - \mu(z_1) = -J_z RT \int_{z_1}^{z_2} \frac{1}{c(z)Dz} dz, \quad (4.7)$$

where z_1 and z_2 are locations on both sides of the membrane system we are interested in.

Assuming small gradients, we replace $c(z)$ by the equilibrium concentration $c^{\text{eq}}(z)$

and define local permeation resistance as

$$R^p = c^* \int_{z_1}^{z_2} \frac{1}{c^{\text{eq}}(z)D(z)} dz, \quad (4.8)$$

where c^* is the concentration of the bulk solvent. Again we assume that there is no gradient enforced in the system.

In the original formulation by Diamond and Katz, additional terms were added to represent the resistances at the interfaces [11]. The probes employed in experiments cannot often properly access the head group region and thus such corrections are needed. In simulations, however, we do not have such restrictions and the inhomogeneous solubility–diffusion model can be applied throughout the membrane with the same formalism.

4.3.2 Relation to Computationally Available Quantities

Our next task is to link the theoretical description and the parameters obtainable from computer simulations. With computer simulations we can obtain information on the details of the permeation process. What are the position dependencies of the diffusion and partitioning? How large is the impact of the interface? What is the rate limiting step? What are the effects of compression, thickness, surface tension and temperature on permeation? What are the differences between permeation through a monolayer and through a bilayer? How are the free energy profile and density profile or the free volume profile linked together? What are the characteristic features of oxygen permeation compared to other small molecules?

While in experimental setups with time scales of seconds we might measure up to millions of molecules permeating through the membranes [12], the case is completely different in the world of atomistic simulations. Special methods are needed as the time scales accessible by the molecular dynamics method are of the order of nanoseconds and the number of molecules permeating the membrane in this time scale is far less than one [12]. Thus in order to obtain proper sampling, we must employ a completely different approach. In what follows we derive equations that link the theory presented above to the physical quantities obtainable from a specific kind of simulation method described in section 5.4. The derivation again closely follows that of Marrink and Berendsen [12], but is performed for the case of canonical ensemble since it was employed in most of our simulations. This ensemble is also known as the NVT ensemble which refers to the fact that the number of particles, volume and temperature are kept constant.

We begin by noting that the local permeant concentration at equilibrium is proportional to the probability at which our system resides in phase space with the restriction that the z coordinate of one penetrant particle (z_0) lies within the

interval from z to $z + dz$. We can thus link the local equilibrium concentration to the partition function Q' as

$$c_i^{\text{eq}}(z) \propto Q'(z) = \frac{1}{N!h^{3N}} \int_{-\infty}^{\infty} \int_{D(V)} \delta(z_0 - z) \exp(-\beta \mathcal{H}(\mathbf{r}^N, \mathbf{p}^N)) d\mathbf{r}^N d\mathbf{p}^N, \quad (4.9)$$

where δ is the Dirac delta function. Now we are able to link the ratio of the concentrations at depth z ($c^{\text{eq}}(z)$) and in bulk (c^*) to the ratio of the partition functions in these locations $Q'(z)$ and $Q'(z_1)$ and this ratio is further related to the Helmholtz free energy difference between the two locations (ΔA) as

$$\Delta A(z) = -RT \ln \frac{Q'(z)}{Q'(z_1)} = -RT \ln \frac{c^{\text{eq}}(z)}{c^*}. \quad (4.10)$$

By combining Eq. (4.10) with Eq. (4.8) we obtain a formula for the permeation resistance as

$$R^p(z) = \frac{\exp\left(\frac{\Delta A(z)}{RT}\right)}{D_z(z)}. \quad (4.11)$$

In homogeneous media the local resistance naturally has a constant value and it is equal to the one suggested by the homogeneous solubility–diffusion model. The local permeation resistance can be linked to the total permeation resistance \mathcal{R} by integration over the membrane as

$$\mathcal{R} = \int_{z_1}^{z_2} R^p(z) dz. \quad (4.12)$$

The experimentally measurable permeability coefficient is obtained as the inverse of this value as

$$\mathcal{P} = \frac{1}{\mathcal{R}}. \quad (4.13)$$

In the case of a monolayer the direction of permeation plays a significant role in the determination of absolute values for permeation. The change of direction affects the free energy profile as a different phase is used as a reference value. The relative permeabilities, however, stay intact. Lets say that the free energy profile is shifted by a value of B so that the new value is $A'(z) = A(z) + B$. Then the new local permeation resistance is obtained from

$$R_{\text{shifted}}^p(z) = \exp\left(\frac{B}{RT}\right) \times R^p(z) \quad (4.14)$$

and thus the permeability from

$$\mathcal{P}_{\text{shifted}} = \exp\left(\frac{-B}{RT}\right) \times \mathcal{P}. \quad (4.15)$$

4.3.3 Free Energies from Mean Force

The free energy difference ΔA is obtained easily from computer simulations if we constraint the permeating particles at various depths in the membrane and calculate the force exerted on that particle in the direction of permeation. This allows us to calculate the local permeation resistances at different locations and from these we can integrate the total permeability coefficient. The z constraint method can be thought as a special case of the so-called umbrella sampling method [130] in which the sampled space in z direction is reduced into a single point per simulated window. The umbrella sampling method is also often used to study the free energy differences of permeation from molecular dynamics simulations as is the Widom particle insertion method, too [131].

However, by employing the z constraint method we are able to calculate both the free energy, an equilibrium quantity, together with the position-dependent diffusion coefficient, a dynamic quantity, from the same simulation data. A refined version of the z constraint method has also been published but here we stick to the one suggested by Marrink and Berendsen [12].

We begin by taking the derivative of the free energy difference in Eq. (4.10) and obtaining

$$\frac{d\Delta A(z)}{dz} = -\frac{RT}{Q'(z)} \frac{dQ'(z)}{dz}. \quad (4.16)$$

The derivative of $Q'(z)$ with respect to z can be obtained by the partial integration of Eq. (4.9) and substitution into Eq. (4.16) to obtain

$$\begin{aligned} \frac{dQ'(z)}{dz} = & -\frac{\beta}{N!h^{3N}} \int_{-\infty}^{\infty} \int_{D(V)} \delta(z_0 - z) \frac{\partial \mathcal{H}(\mathbf{r}^N, \mathbf{p}^N)}{\partial z} \\ & \times \exp(-\beta \mathcal{H}(\mathbf{r}^N, \mathbf{p}^N)) d\mathbf{r}^N d\mathbf{p}^N. \end{aligned} \quad (4.17)$$

Thus we obtain a formula for the derivative of the free energy difference with respect to the z coordinate as

$$\frac{d\Delta A(z)}{dz} = -N_A \left\langle \frac{\partial \mathcal{H}(\mathbf{r}^N, \mathbf{p}^N)}{\partial z} \right\rangle_{z_0} = -N_A \langle F_z(z_0) \rangle, \quad (4.18)$$

from which the free energy at depth z is obtained as

$$\Delta A(z) = -N_A \int_{\text{bulk water}}^z \langle F_z(z') \rangle dz'. \quad (4.19)$$

Here $\langle F_z(z') \rangle$ is the mean force that the constrained particle experiences, and it is obtained in the simulation as

$$F_z = m \frac{\Delta z}{(\Delta t)^2}, \quad (4.20)$$

where m is the mass of the particle and Δt the time step. The penetrant is constrained in the z direction by resetting its centre of mass position to the desired fixed z value at each step. This change is labelled as Δz . We see that the force is a linear function of this displacement. The permeating particle is free to move in the xy -plane and to rotate in all directions. The reference position is often given relative to the membrane system to cancel fluctuations of the whole system. The z constraint method is of most use in the region between the head groups and the low-density part of the hydrocarbon tails but it is here employed for the whole system. Sufficient accuracy is obtained by simulating the systems for a long time.

4.3.4 Local Diffusion Coefficients from Force Autocorrelation

The most effective way to obtain the local diffusion coefficients is to employ the force autocorrelation method as this way we are able to perform the calculations on the data obtained from the constrained z coordinate simulations that are also employed for the calculation of the free energy. The fluctuation–dissipation theorem [132] states that the location- and time-dependent friction coefficient, $\xi(z, t)$, can be given as

$$\xi(z, t) = \frac{\langle \Delta F_z(z, t), \Delta F_z(z, 0) \rangle}{RT}, \quad (4.21)$$

where ΔF stands for the random force that is exerted on our constrained particle. The angle brackets stand for calculation of the autocorrelation function through averaging in time. The static local friction coefficient $\xi^S(z)$ is obtained through time integration of this function. The assumption that during the decay of this autocorrelation function the particle stays in a region of constant free energy enables us to employ the Einstein relation, Eq. (4.4), to obtain

$$D_z(z) = \frac{RT}{\xi^S(z)} = \frac{(RT)^2}{\int_0^\infty \langle \Delta F_z(z, t), \Delta F_z(z, 0) \rangle dt}. \quad (4.22)$$

The random force at time t is given as the difference of the force at time t and the average force as

$$\Delta F_z(z, t) = F_z(z, t) - \overline{F_z(z, t)}, \quad (4.23)$$

where the overlining stands for averaging.

If the surrounding medium is considered to be locally isotropic, the diffusion coefficient in the direction perpendicular to the membrane plane can be approximated by the diffusion coefficient along the membrane plane. Since the permeating particle is free to diffuse in the xy -plane in the z constraint method, we can readily calculate the lateral diffusion coefficient, D_{xy} , in this plane. Since the force autocorrelation data is often really noisy even after a reasonably long simulation and obtaining a precise value for the integral in the denominator of Eq. (4.22) can be difficult, we can use the lateral diffusion coefficient to validate the method at least in the isotropic regions of our system. The lateral diffusion coefficient is defined as the slope of the mean squared displacement (MSD) as

$$D_{xy} = \lim_{t \rightarrow \infty} \frac{1}{4t} \langle [\mathbf{r}(t) - \mathbf{r}(0)]^2 \rangle, \quad (4.24)$$

where the angle brackets denote averaging of the MSD over the simulation time and \mathbf{r} is a vector in the xy -plane.

Other possibilities for measuring permeabilities computationally exist. The local diffusion coefficients and excess free energies required for the inhomogeneous solubility–diffusion model can be obtained with different methods as is explained in [12].

While the inhomogeneous solubility–diffusion model has been employed in various studies recently [8, 12, 83, 92, 98, 99, 116, 120, 133], others have focused on studying permeation considering only the diffusion part [134–136] or the energetic part [9, 122, 137]. The solubility part can also be calculated by introducing numerous oxygen molecules in the simulation system and letting them to permeate into the membrane. Solubility is then obtained from the concentration profile along the membrane [10]. However, to obtain reliable statistics with this methodology, pointlessly long simulations might be required.

4.4 Oxygen Permeation through Membranes

Oxygen permeation through lipid membranes and monolayers has been studied to some extent both experimentally [5–7] and computationally [8–10]. However, the permeation through lipid monolayers and especially those with composition mimicking that of lung surfactant structures has to our knowledge not been examined with the detail that the inhomogeneous solubility–diffusion model is able to provide.

Since oxygen is a highly hydrophobic molecule, it prefers to dissolve into the membrane interior in a bilayer system. The diffusion is also fastest in the hydrocarbon core where the density is at its lowest [8]. Thus the membrane might act as a permeation accelerator [8]. The unhindered movement through the tail part has also been seen with a very simple monolayer model [9]. The glycerol backbone region is possibly rate limiting in the case of O_2 due to the low solubility and low diffusion coefficients of oxygen in this region and the small number of voids present therein [97]. To conclude, the permeation of oxygen through membranes has earlier been considered to be rapid with permeation coefficients close to those of oxygen in pure water [138, 139].

Recently, however, another possible mechanism for permeation has been suggested. Ivanov et al. measured the permeation coefficients of oxygen in pure DPPC monolayers and found values that are three or four orders of magnitude smaller than those previously reported for lipid bilayers [6]. They suggest that the discrepancy arises from the use of probes with bulky organic radicals that perturb the membranes during measurements. The values they found are close to those of other polar molecules of similar size. Their conclusion was that the presence of aquaporin or H^+ channels in real functional membranes could enable the experimentally observed rapid permeation of oxygen [6].

In their more recent paper, Ivanov et al. found that oxygen permeation through a red blood cell membrane was slowed down substantially as they introduced mercury compounds acting as aquaporin inhibitors [102]. They consider these results to be the first evidence supporting the idea that oxygen, like many other small penetrants, permeates biological membranes through aquaporin channels [102]. The computational study by Hub and de Groot showed that it would be possible for oxygen to permeate through the GlfP channels but the high free energy barrier of hAQP1 channels caused by the hydrophobic nature of oxygen does not support the view presented by Ivanov et al. [137].

The wide range of values for oxygen permeation available can be explained both by the different measuring techniques and the properties of membranes such as temperature, surface tension and area per molecule, along with many others. The phase transitions have an effect on diffusion and possibly also on partitioning [140]. The domains might also have an effect depending on both the protein and cholesterol concentrations inside the domain [141, 142]. Ivanov et al. state that the slower-than-expected permeation of oxygen through monolayers is caused by microviscosity [6]. On the macroscopic level, however, the effect of macroscopic viscosity on oxygen diffusion in alkanes is found to be smaller than what is suggested by the Stokes–Einstein law [143, 144].

Strutwolf et al. employed the scanning electrochemical microscopy induced transfer

method to measure the permeability coefficients of oxygen through C₁₄PC, C₁₆PC and C₁₈PC monolayers at the liquid–liquid interface [105]. The coefficient for C₁₈ monolayers was substantially smaller than those for C₁₆ and C₁₄ monolayers due to differences in phase behaviour of these alkanes [105].

It has also been found that in the permeation through membrane complexes such as those found in the lung, the surfactant proteins SP-B and SP-C facilitate permeation by forming pathways so that diffusion is faster than through bulk lipid layers separated by water [54]. This is due to the poor solubility of oxygen into water [54]. These structures residing below the surfactant monolayer might also be difficult to control in experiments and they might thus greatly affect permeation rates.

The favourable entropy component and small enthalpy component typically drive the partitioning of hydrophobic molecules from water to the hydrophobic phase [97, 145]. However, studies on the partitioning of hydrophobic solutes into ordered lipid phases have challenged this picture [118, 119] and the permeation process was suggested to have been driven by a strong favourable enthalpy. This phenomenon is referred to as the bilayer effect or the non-classical hydrophobic effect [118, 119, 145, 146].

A study by Pu et al. showed that oxygen permeation through a polycrystalline phospholipid monolayer increases linearly with increasing domain boundary density and decreases exponentially with increasing lipid tail length [93]. The latter effect was also observed for condensed lipid monolayers by Borden and Longo [7], who also noticed that a smaller head group enabled lipids to pack tighter which resulted in a higher permeation resistance.

Subczynski et al. studied permeation of oxygen in PC bilayers and found that the transport is best explained by comparing the views of Träuble with those of Pace and Chan. The former one suggests that oxygen travels in the membrane along with kinks in lipid tails [107] as the latter one suggests there are jumps from one kink to another [148]. The kinks arise from *trans*–*gauche* conformations and packing defects such as hydrophobic length mismatch [147].

The permeability of DPPA monolayers was seen to decrease exponentially as the surface pressure was increased [96]. Same was observed for DSPE [149]. The change in permeability due to varying the surface tension was also discussed by Zuo et al. [3]. According to their study on bovine lipid extract surfactant the permeability of oxygen is only drastically hindered when surface tension drops down to values of a few mN/m. Similar observations were also made by Sosnowski et al. who found out that the lung surfactant provided no resistance to oxygen permeation at higher surface tension values but as this value was decreased from 37 to 22 mN/m, oxygen permeation slowed down by 30%. Ivanov et al. also noticed a decrease of one order of magnitude as the surface tension of their monolayer was decreased from 68 to 54 mN/m [6].

Zhang et al. found that there was no significant change in the permeability of oxygen through DSPC monolayers at a decane–water interface in the liquid expanded phase, but in the liquid condensed phase the permeation decreased drastically [151]. Macho et al. also observed a decrease in oxygen permeability when their DPPE films were tightly packed [152]. These findings are extremely important if lung surfactant is present in a highly condensed state.

5. COMPUTATIONAL METHODS

In this chapter the simulated systems are listed and the key parameters for each type of simulation are given. This listing is performed for both the thermodynamic integration simulations that aim for the development of a sufficient model for the oxygen molecule, and the constrained MD simulations whose goal is to study the permeation of oxygen through a lung surfactant monolayer, and the possible structures residing below it. All the parameters are listed in detail.

5.1 Overview of Molecular Dynamics

Molecular dynamics (MD) is a rather simple method that enables one to perform computer simulations employing only the principles of classical mechanics [153]. The exclusion of quantum mechanics makes it possible to use relatively long time scales yet retaining the discrete nature of particles as small as single atoms making it an ideal method of choice for studies of biological problems. In practice, these simulations still require a lot of computing power and large clusters or supercomputers are often employed in order to reach relevant time and length scales.

Simulations are performed by following the general MD algorithm given in Fig. 5.1. In the main cycle the simulated particles are relocated as their new positions are obtained by integrating the Newtonian equations of motion for each particle in the system. The forces acting on each of these particles required for the integration are extracted from the potential function by differentiation. The cycle is repeated until a desired simulation time is obtained. This internal time of the system is extended by the value of the time step after every cycle and is usually advancing by a rate of about one trillionth of the real world time used for the simulation.

In MD, a force field refers to the functional forms of the interaction potentials and the parameter sets used in these potential functions for different particles being studied. The parameters are obtained from comparing the simulation results to those obtained from both experimental studies and quantum chemistry calculations. The former often provide us with knowledge on dynamical properties, energetics and larger scale structure while the latter give us information of the fine structural details.

A lot of trial and error is often required in the development of a force field in order for the model to match the desired physical properties. It should also be noted that

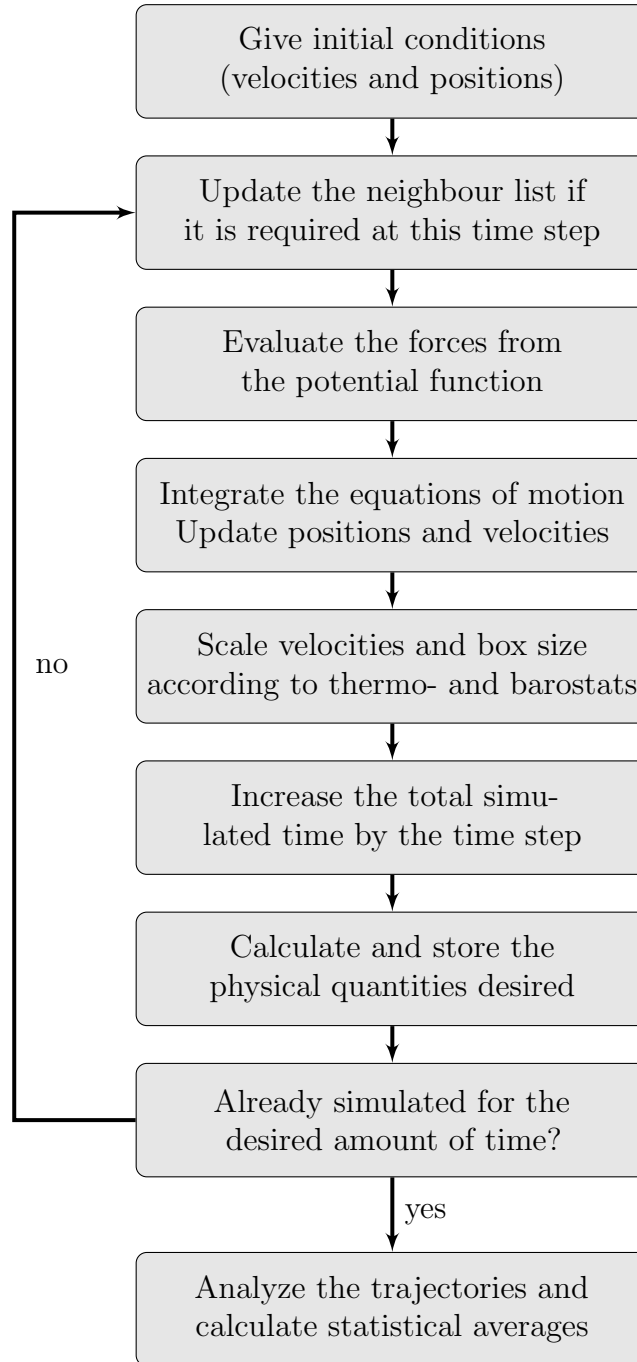


Figure 5.1: Flow chart of the simplified MD algorithm.

due to the fairly simple form of the potential function not all physical properties can be reproduced with the same parametrization. The validity of the parameter sets is usually limited and thus for each different type of simulation the optimal set of parameters must be either specially derived or carefully selected from the existing ones.

There are various force fields available for MD simulations. In this study we

employ the functional forms of the Optimized Potentials for Liquid Simulations (OPLS) united atom force field [154] with the Berger parametrizations for lipid molecules [155]. United atom refers to a force field in which the hydrogen and carbon atoms in methylene and methyl groups are considered as one simulation particle with the parametrization providing it with properties characteristic of the original set of atoms. This approach is often used since classical mechanics cannot account for the quantum-mechanical properties of the light hydrogen atoms. The reduction of the number of simulation particles allows the united atom method to be considerably faster than the all-atom method by a factor of about four [79].

The potential function is a classical description of the interactions between the particles in the simulated system. The forces exerted on single particles can be calculated by differentiating the potential function of this particle with respect to distances and angles to the other particles. The accelerations of the particles can then be calculated using the Newton's equations of motion. The general form of the potential function used in the OPLS force field consists of both bonded and non-bonded interactions. The former are represented with three terms accounting for bond stretching, bond angle vibrations and the torsion angle (also called a dihedral) twisting. These interactions are explained in Fig. 5.2.

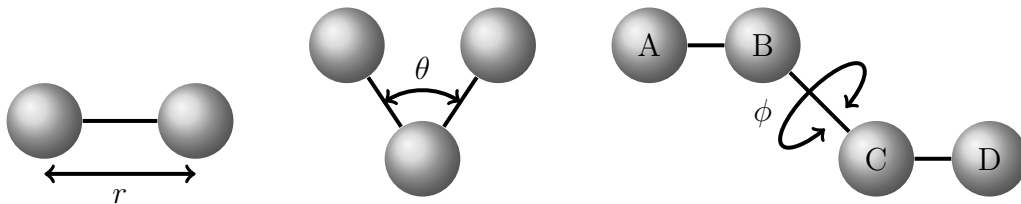


Figure 5.2: Bonded terms of the OPLS potential function. The two-body term is called bond stretching and it is a function of the inter-particle distance r . The three body term is the angle bending and it is a function of the angle θ defined by the three particles. The four-body term is the relative twisting of the planes ABC and BCD and it is characterized by the torsion angle ϕ .

The non-bonded interactions are described by two terms in the potential function. The electrostatic potential between two charged particles is considered by the Coulomb's law. It is scaled properly by the permittivity of the media. Both the always attractive van der Waals interaction and the always repulsive steric interaction between each pair of particles are presented by the Lennard-Jones (LJ) potential term. The sum of these contributions determines the nature of the LJ potential between a pair of particles and this value depends on their relative distance. When far from each other, the LJ potential between two particles is slightly attractive. However, when brought close to each other, a steep rise in the potential function is observed and the interaction becomes highly repulsive. Between these two extremes the LJ

potential obtains its minimum value at an inter-particle distance which presents the situation of the particles described by their hard core radii being in direct contact with each other.

In order to speed up the calculations, certain cut-off schemes are employed for the non-bonded interactions. The GROMACS simulation package uses a neighbour list to keep an account on which pairs of atoms the non-bonded interactions need to be calculated for. The update frequency of this list can be varied. The mathematical formulation of the potential function used in the OPLS force field is given as

$$\mathcal{H}_{\text{total}} = \mathcal{H}_{\text{bonded}} + \mathcal{H}_{\text{non-bonded}} \quad (5.1)$$

$$= \sum_{\text{bonds}} k_{r,i} (r_i - r_{i,0})^2 + \sum_{\text{angles}} \frac{k_{\theta,i}}{2} (\theta_i - \theta_{i,0})^2 + \sum_{\text{dihedrals}} \left(V_0 + \frac{V_1}{2} (1 + \cos \phi_i) + \frac{V_2}{2} (1 - \cos 2\phi_i) + \frac{V_3}{2} (1 + \cos 3\phi_i) \right) + \sum_{i=1}^N \sum_{j=i+1}^N \left(\frac{C_{ij}^{(12)}}{r_{ij}^{12}} - \frac{C_{ij}^{(6)}}{r_{ij}^6} + \frac{q_i q_j}{4\pi\epsilon_0\epsilon_r r_{ij}} \right) f_{ij}, \quad (5.2)$$

where the k 's are force constants for stretching and angle vibrations. The parameters r_i and θ_i correspond to the bond length and the angle of the bond under study, while $r_{i,0}$ and $\theta_{i,0}$ represent their corresponding equilibrium values. V_i 's are constant multipliers in the cosine series, whereas ϕ is the difference between the dihedral angle and its equilibrium value. The equilibrium value is usually set to zero but in some cases it might also have the value of 180° . The symbols $C_{ij}^{(12)}$ and $C_{ij}^{(6)}$ are related to definite pairs of interacting particles and r_{ij} is their relative distance. Other ways to describe the Lennard-Jones potential are also possible and maybe the most common notation uses the parameters σ and ϵ which have physical interpretations as they are related to the form of the potential function. σ and ϵ describe the location of the zero of the potential and the depth of the potential well respectively. $C^{(12)}$ and $C^{(6)}$ are combinations of these parameters, and σ is given as $\sqrt[6]{2C^{(12)}/C^{(6)}}$ that is required in this work in the discussion of the soft-core potentials employed together with the thermodynamic integration method. ϵ is obtained as $-B^2/(4A)$. The (σ, ϵ) description is also employed when these parameters for the atoms of the oxygen molecule are optimized. The powers of 6 and 12 are employed in the Lennard-Jones potential instead of more accurate exponential models because it is very fast to compute the term r^{12} by simply squaring the r^6 term. Charges on the particles i and j are written as q_i and q_j , whereas ϵ_r and ϵ_0 represent the relative permittivity of the medium and the permittivity of the vacuum, respectively. The non-bonded interactions of particles less than four bonds apart are scaled with a special factor f_{ij} . This scaling factor takes the value of 0.5 for particles that are separated by three

bonds and a value of 0 when they are just one or two bonds apart. For other pairs of particles the scaling factor is equal to 1.

There are many ways to perform numerical integration. The method used by the GROMACS simulation package is called the leap frog algorithm [156], a modified version of the better known Verlet integrator [157]. The name of the algorithm comes from the fact that the positions and velocities of the particles are never calculated at the same time step. The equations for the calculation of position and velocity can be written as

$$\mathbf{r}_i(t + \Delta t) = \mathbf{r}_i(t) + \mathbf{v}_i\left(t + \frac{1}{2}\Delta t\right) \Delta t \quad (5.3)$$

$$\mathbf{v}_i\left(t + \frac{1}{2}\Delta t\right) = \mathbf{v}_i\left(t - \frac{1}{2}\Delta t\right) + \frac{\mathbf{F}_i(t)}{2m_i} \Delta t, \quad (5.4)$$

where \mathbf{r}_i and \mathbf{v}_i stand for the position and velocity of the examined particle i . t is the time of the step at which we are calculating the velocities and positions, and Δt is the length of a time step. \mathbf{F}_i represents the force exerted on the examined particle with mass m_i .

There are many programs available for MD. In this study we are employing GROMACS, a public domain software package that has great scalability and that can be used together with a large variety of different force fields [78, 79]. The outcome of an MD simulation is a trajectory providing us with information on the places and velocities of all the different particles at desired time intervals. This data can then be analysed for information on the dynamics, energetics and structural features of the system.

5.2 Thermodynamic Integration

To calculate the free energy difference between the oxygen molecule solvated in water phase, and in hexadecane representing the organic phase, we constructed two systems, one for each phase. The box with water consisted of 1728 water molecules and spanned spatial dimensions of about $(3.7 \text{ nm})^3$. The SPC description for the force field of water was used [158]. Another cubic box with an edge of also 3.7 nm was filled with 108 hexadecane molecules for which the united atom description was applied. Force field parameters for hexadecane were similar to those employed in the Berger force field [155] for saturated lipid tails. The simulated systems are depicted in Fig. 5.3.

For both systems we employed a total of 23 simulations with varying values for the coupling parameter λ . The values used were 0.00, 0.03, 0.09, 0.14, 0.18, 0.24, 0.30, 0.35, 0.40, 0.45, 0.48, 0.52, 0.55, 0.58, 0.60, 0.62, 0.65, 0.70, 0.75, 0.80, 0.85, 0.90 and 1.00. A denser spacing was used near the value $\lambda = 0.5$.

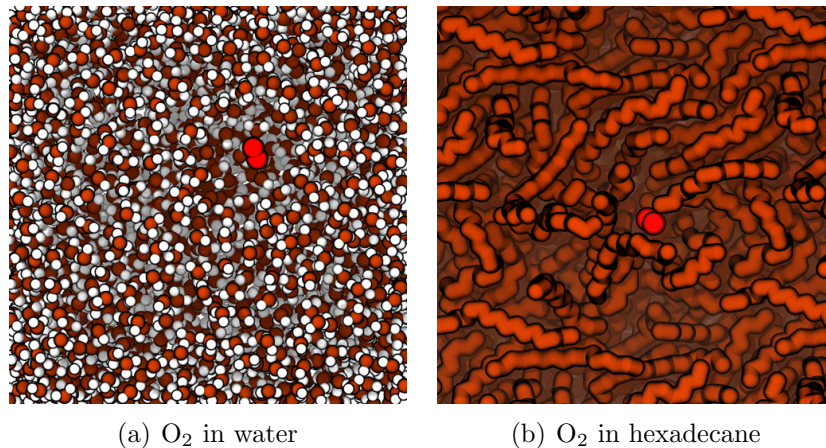


Figure 5.3: Systems used for thermodynamic integration.

Both simulations employed the stochastic dynamics integrator with a time step of 0.1 fs for a total simulation time of 3 ns at a temperature of 298 K. Periodic boundary conditions were employed in all directions and the neighbour list with a cut-off of 1.0 nm was updated every 10 steps. Electrostatic interactions were calculated using the Particle-Mesh Ewald (PME) summation scheme [159] of order 4 with a cut-off of 1.0 nm and a spacing of an FFT grid of 0.12 nm. Lennard-Jones interactions were cut-off at 1.0 nm and long range dispersion correction was applied to both energy and pressure. The Parrinello–Rahman barostat [160] was used for isotropic pressure coupling with a time constant of 4 ps. The compressibility of the system was set at $4.5 \times 10^{-5} \text{ bar}^{-1}$ and the reference pressure at 1 bar.

No constraints were applied to the bonds. The coupling parameter value was held constant for the entire simulation and the interactions of the oxygen molecule were turned off in two sets of simulations. In the first set the Coulombic interactions were turned off and in the second set the Lennard-Jones interactions were made to disappear. The soft-core model for the non-bonded interactions was employed with the parameters $\alpha = 0.65$, $s = 1$ and a value of $\sigma = 0.30$ was used if either of the Lennard-Jones parameters, $C^{(6)}$ or $C^{(12)}$, was equal to zero. The volumes of the systems were also very similar. In this case we can ensure that there is no entropy difference between the two systems with single dummy oxygen molecules as explained in Section 3.1

The values of $\partial\mathcal{H}/\partial\lambda$ were saved every time step and the values obtained during the last 2.8 ns were used for calculations. The averages obtained with different values of λ were then integrated with respect to λ to obtain the free energy difference as suggested by Eq. (3.17).

We tried various parameters for the oxygen molecule to obtain a correct value for the free energy difference between the two phases. The bond length of the molecule

was set at 0.123 nm with a force constant of 251208 kJ/mol. A dummy particle with no mass was placed halfway between the oxygen atoms to produce the correct quadrupole moment. The quadrupole moment for a continuous charge distribution is defined as

$$Q_{ij} = \int (3x_i x_j - \delta_{ij} r^2) \rho(r) dV, \quad (5.5)$$

where i and j take the values of x , y and z , δ_{ij} is the Kronecker delta function and $\rho(r)$ the charge density at position r . In our case of point partial charges this simplifies to

$$Q_{ij} = \sum_l (3(x_i)_l (x_j)_l - \delta_{ij} r_l^2) q_l, \quad (5.6)$$

where q_l is the partial charge on the atom l .

Thus for our molecule, we label the distance between the oxygen atoms as $2d$, the charge on the dummy particle as $2q$, and the counteracting charges on the oxygen atom thus have the value of $-q$ each. Then the quadrupole moment's zz component simplifies to $Q_{zz} = -4qd^2$. With the employed partial charges of 0.22272 and -0.11136 e for the dummy particle and the oxygen atoms, respectively [137], we obtain a value of 0.81 DÅ (Debye \times Åström). A schematic drawing of the oxygen model is presented in Fig. 5.4. Thus the only parameters left for the adjustment were the Lennard-Jones parameters σ and ε . Various sets were employed for these in order to obtain the free energy difference as close to its experimental value as possible.

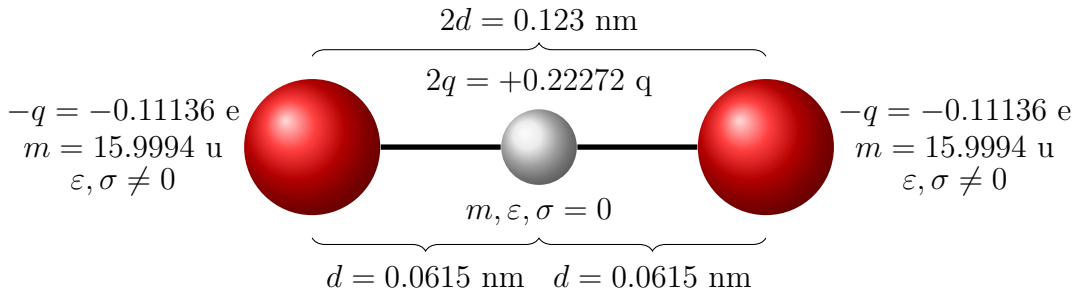


Figure 5.4: The employed O₂ model. The charges, masses and bond lengths are fixed while the Lennard-Jones parameters ε and σ are being adjusted. The red spheres represent the real oxygen atoms while the virtual site is shown in grey.

5.3 Other Methods of Validation

Other methods were also employed for the validation of the model. A box of pure oxygen was simulated for the calculation of the density of pure oxygen liquid at

its melting point of 90.2 K. We simulated a box with 2197 oxygen molecules for a total of 5 ns, employing the leap-frog Newtonian dynamics integrator [156]. The size of the simulation box was allowed to vary according to the Parrinello–Rahman barostat [160]. Temperature was kept constant with the V-rescale algorithm [161]. The density was calculated with the tool `g_density` supplied with the GROMACS package.

Heat or enthalpy of vaporisation is also often employed in the parametrisation of force fields together with density as their combination provides information on both energetic and structural features of a liquid. OPLS is an example of a force field whose basis lies in matching these two features with their experimental values [154].

Enthalpy is a thermodynamic function defined as

$$H = U + pV, \quad (5.7)$$

where U is the internal energy, p the pressure and V the volume of the system. The change in enthalpy related to the vaporisation process can be obtained as a simple difference since enthalpy is a state function. At constant pressure the heat of vaporisation can be calculated from

$$\Delta_{\text{vap}} H^p = U_{\text{vapour}} - U_{\text{liquid}} + pV(V_{\text{vapour}} - V_{\text{liquid}}), \quad (5.8)$$

where pV and H^p indicate that the constant pressure situation is considered. Since the pV term for a liquid is much smaller than that of a gas, we can assume that $pV_{\text{liquid}} = 0$. As we can consider the vapour to behave ideally, we employ the ideal gas law

$$pV = nRT, \quad (5.9)$$

where n is the amount of substance in moles, R the gas constant and T the temperature. Thus the usable form for enthalpy of vaporisation per mole is written as

$$\Delta_{\text{vap}} H^p = U_{\text{vapour}} - U_{\text{liquid}} + RT. \quad (5.10)$$

Enthalpy of vaporisation was calculated by simulating both the liquid and vapour phases at the melting point of oxygen. The liquid phase had 2197 molecules and it was simulated for 5 ns employing the stochastic dynamics integrator. Pressure was kept constant with the Parrinello–Rahman algorithm [160].

A single oxygen molecule in a large box ($8 \times 8 \times 8 \text{ nm}^3$) of constant volume was employed to mimic the vapour. This system was simulated for 50 ns to obtain

statistically meaningful results. Again the stochastic dynamics integrator was used. The energies of both the liquid and the vapour were calculated using the `g_energy` tool, which is part of the GROMACS distribution.

5.4 Permeation Studies

For the permeation studies we employed a model for a protein-free pulmonary surfactant, whose dynamical properties were studied very recently [162]. We also performed calculations on a bilayer with similar a lipid composition for comparison to both experimental and previous simulation studies. The seven simulated monolayer systems represent different compression states of the pulmonary surfactant as their mean molecular areas range from 44 to 68 Å² per lipid with a step of 4 Å². The monolayer systems had two leaflets of lipids separated by a water slab. All the monolayers and the bilayer had a total of 100 lipid molecules in each leaflet with a composition of 60% DPPC, 20% POPC, 10% POPG and 10% cholesterol. The monolayer structures were fully hydrated with 7235 water molecules. A physiological salt concentration of 150 mM of NaCl was employed and additional 20 sodium ions were inserted as the counter ions for the charges in the POPG head groups. A similar salt concentration was also used for the bilayer system with a total 3850 of water molecules. A slightly modified version of the Berger lipids force field [155] was employed for the lipids and the SPC description was used for water [158]. The obtained optimal parameters from the thermodynamic interaction studies were employed for the oxygen molecules.

The systems were constructed starting with a single lipid molecule of each type. The coordinates of these molecules were extracted from bilayers employed in previous studies. We multiplied these one molecule systems to create regular grids of the lipids with very large gaps. We then mixed the grids of different components to create a system with the desired composition. Small relative displacements were applied to different grids in order to avoid overlapping and steric contacts. We compressed the obtained multicomponent grid step-by-step to a desired molecular area of 60 Å². The structure was energy-minimized after each step using the steepest descent algorithm provided with the GROMACS package [78]. The relative compression was five per cent at each step. After the compression, we duplicated this grid to create a bilayer system.

The system was then fully hydrated and again energy-minimized. It was simulated with GROMACS for a short time in order to obtain a stable bilayer structure. This structure was used for the bilayer simulations and to construct the monolayer systems. The water molecules and salt ions were removed and the positions of the two layers were switched. Water and salt ions were again added in between the layers for extensive hydration. The systems obtained were then transformed into the desired

areas per molecule by simulating them with a continuously varying box size with a special version of GROMACS. In this fashion, we were able to compress and expand the structures to a wide range of molecular areas. The limiting values used were 80 and 40 Å² with the former experiencing the formation of holes and the latter buckling during the conversion. The desired frames with correct box sizes were extracted from the simulation trajectory. The monolayers were further apart from each other in the more compressed systems than in the more expanded ones. This is due to the volume of the simulation box being kept constant during the alteration of the box size in the direction of the plane of the membrane.

The permeation through the monolayer system was studied by constraining the z coordinates of two oxygen molecules at different depths in the monolayer, one in each leaflet using the SHAKE constraint method [163]. The constraint distance was chosen with respect to the centre of mass of the monolayers to. One monolayer of the simulated system with a mean area per molecule equal to 56 Å² is depicted in Fig. 5.5 with the constraint locations for oxygen indicated. We perform a set of simulations with the constrained molecules at different z positions within the monolayers. The positions were chosen with a spacing of 0.1 nm. The number and z coordinates of the positions depend on the system under study. For example, for the system with an area per molecule equal to 56 Å² we used a total of 45 simulations covering a total of 4.5 nm. The oxygen molecules were added into the system by forcing their inclusion in the structure file and then performing a thorough minimization in order to remove any steric contacts.

The two oxygen molecules were passing the different monolayers at the same time and the obtained free energy profiles are mirror images of each other. They also have a different reference state, that is, the integration of Eq. (4.19) gives the free energy difference with respect to a different choice of zero. Water phase was chosen to stand for the reference level. We employed a similar method for the bilayer with the largest difference being that there was only one permeating molecule which sampled the depth of the whole membrane (two monolayers), thus going from the water phase into the membrane and back into the water phase. The simulated bilayer system is depicted in 5.6.

To validate the results of the z constraint method, umbrella sampling simulations were performed on the bilayer with the same parameters as the z constraint simulations. Umbrella sampling simulations differ from the z constraint ones in that the location of the permeating molecule is not completely restricted in the pulling dimension but rather allowed to move a little. An imaginary spring is attached between the molecule and the reference position that allows the molecule to sample its close neighbourhood. The aim is to obtain a continuous sampling of the whole range of reference locations and this is obtained by choosing a suitable spring constant that

is neither too stiff nor too loose. In the analysis, the effect of the spring is eliminated. We employed a value of $1000 \frac{\text{kJ}}{\text{mol} \times \text{nm}^2}$ for the spring in our simulations.

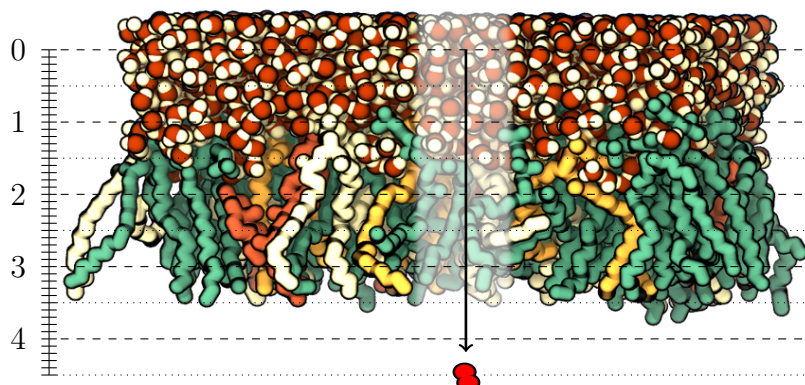


Figure 5.5: Simulated monolayer system with mean area per molecule equal to 56 \AA^2 . The locations at which the oxygen molecule was constrained are indicated. DPPC is drawn in green, POPC in yellow, POPG in white and cholesterol in orange.

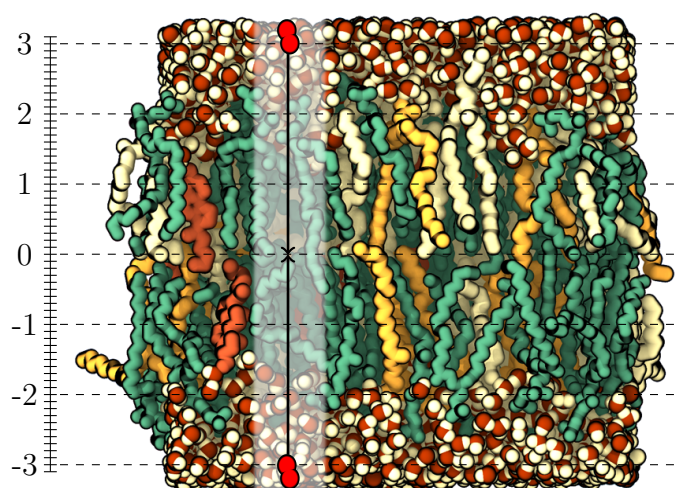


Figure 5.6: Simulated bilayer system with oxygen constraint locations indicated. The molecules are coloured as in Fig. 5.5

The constraint MD simulations were performed using the leap frog integrator with a time step of 2 fs. The total simulation time was set to 10 ns for each system. The neighbour list with a cut-off of 1.0 nm was updated every 10 steps. Electrostatic interactions were calculated with the Particle-Mesh Ewald summation [159] algorithm of the order of four. A cut-off of 1.0 nm was used for both the Coulombic and Lennard-Jones interactions. The FFT grid spacing of the PME algorithm was set to 0.12 nm. The V-rescale algorithm [161] was employed in order to keep the temperature of the system constant. The lipids and the water were coupled separately. The time

constant of the thermostat was set to 1 ps. The force exerted to the oxygen molecule was saved every 10 steps.

For the system with $\langle A \rangle = 56 \text{ \AA}^2$ we employed five different temperatures in order to be able to separate the free energy into energetic and entropic components. The chosen temperatures were 300, 305, 310, 315 and 320 K with the value in the middle being the interesting one representing the normal human body temperature. The length of these simulations was also extended to 15 ns per window to obtain better statistics. All other systems were simulated only at one temperature of 310 K. The monolayer system requires an NVT simulation and thus no pressure coupling was employed. In the case of the bilayer, however, volume of the system was not fixed but allowed to vary according to the Parrinello–Rahman barostat algorithm [160]. All bonds were constrained using the 4th order LINCS algorithm [164] to obtain a speed increase of the order of four [79].

6. RESULTS

This chapter begins with a list of results from the simulations that were used in order to optimize the force field parameters of the oxygen molecule. Our model is compared to both experimental results and values obtained for other parametrisations employed in earlier studies.

The latter part of the chapter consists of results of the permeation studies performed on both a bilayer and various monolayers at different compression. The results that ultimately aim to a single permeability value for each membrane system are explained step-by-step and compared to experimental and simulation results. The bilayer acts as a control system, while the permeabilities of the monolayers are plotted against their physical quantities. The dependencies found are discussed and compared to findings of other related studies. The effects of the suggested structures existing beneath the surfactant monolayer on oxygen permeation are also evaluated.

6.1 O₂ Parameters from Thermodynamic Integration

After testing numerous combinations of ε and σ for the oxygen atom, the optimal parameters were obtained. Initially, bracketing was conducted with parameter pairs close to those previously employed in other studies. The heats of vaporisation and densities of the combinations of $\sigma = 2.9, 3.0$ and 3.1 \AA with those of $\varepsilon = 0.2, 0.3, 0.4$ and 0.5 kJ/mol were calculated in order to bracket the values that were physically acceptable. It was found out that with ε values too large the heat of vaporisation turned out to be too large, and with σ or ε values too small the density was extremely small. This bracketing together with the data calculated for the formerly employed models and some fine tuning enabled us to find the optimal parameters of $\varepsilon = 0.407 \text{ kJ/mol}$ and $\sigma = 0.300 \text{ nm}$.

The dependence of $\partial\mathcal{H}/\partial\lambda$ on λ is shown in Fig. 6.1 together with the integrated free energy curves. The free energies obtained from thermodynamic integration for water were $\Delta G_{\text{water}} = 8.79 \pm 0.11 \text{ kJ/mol}$ consisting of -0.13 kJ/mol for the electrostatic and 8.92 kJ/mol for the Lennard-Jones part. The respective values for hexadecane, $\Delta G_{\text{organic}}$, were $3.50 \pm 0.14 \text{ kJ/mol}$, -0.07 kJ/mol and 3.57 kJ/mol . Thus the free energy difference for transferring an oxygen molecule from the water phase to the organic hexadecane phase according to Fig. 3.1 is $\Delta G_{\text{water} \rightarrow \text{organic}} = -5.3 \pm 0.3 \text{ kJ/mol}$ at 298 K. The volumes of the systems were very similar and the

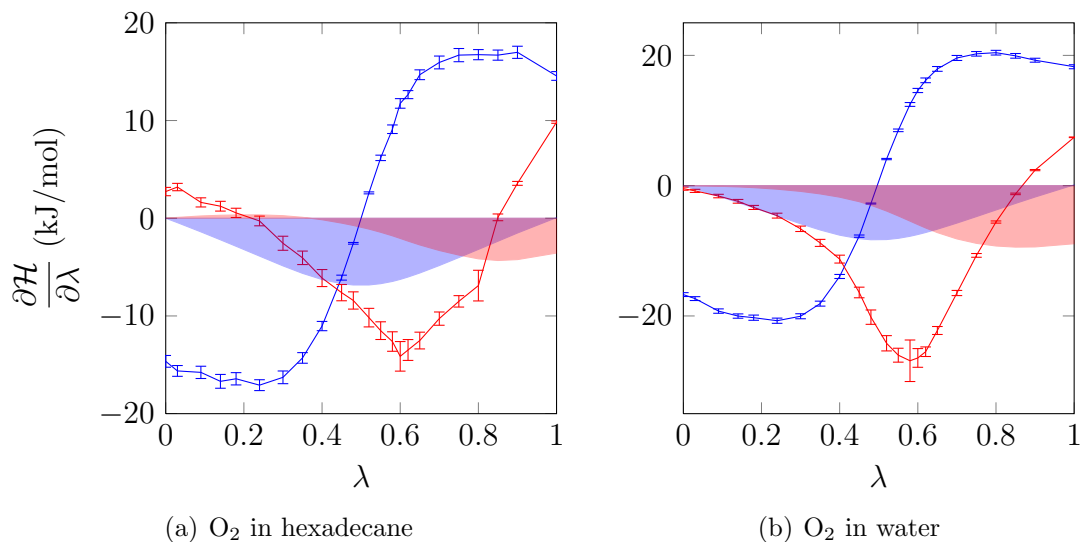


Figure 6.1: Results from thermodynamic integration. Blue curves represent turning off the coulombic interactions, while red curves show the effect of turning off Lennard-Jones interactions. The error bars show two times the standard errors which are calculated using the block averaging method [165]. The filled areas represent the integrals of the curves from $\lambda = 0$ to the respective λ value.

entropy change of the dummy molecules in the thermodynamic cycle, Fig. 3.1, can be neglected.

Since no values for the free energy difference of oxygen molecules in water and hexadecane were found in the literature, they were calculated from other thermodynamic quantities. According to Abraham et al. the hexadecane–gas partition coefficient for oxygen is 0.19 [166].

From the solubility of oxygen in water we can obtain the partitioning coefficient between water and gas from Henry’s law approximately in the form of

$$\frac{[\text{O}_2]_{\text{water}}}{[\text{O}_2]_{\text{gas}}} \approx \frac{RT}{p} \times [\text{H}_2\text{O}] \times X_1, \quad (6.1)$$

where $[\text{H}_2\text{O}]$ is the concentration of pure water (55.51 mol/l) and X_1 the solubility of oxygen in water (2.293×10^{-5} at 1 atm [167]). A value of 0.031 is obtained when the numbers are plugged in.

Thus the partition coefficient for hexadecane/water is $P = 0.19/0.031 = 6.0$. The free energy difference is obtained from this value through the use of Eq. (3.2), which results in a value of -4.4 kJ/mol. The value we obtained from the simulations is somewhat larger than the value calculated from the literature values but it performs better than models used earlier as can be seen from the comparison in Table 6.1.

One problem arises since our simulation method corresponds to the case of infinite

dilution with no solute–solute interactions. The literature values are often, however, tabulated for concentrations of 1 mol/l which is also true in our case. This is problematic since the derivation of an analytical correction is impossible due to the complexity of the system. In the case of ideal particles the correction to the free energy obtained from the entropy of mixing would be equal to 1.08 kJ/mol, bringing the experimental value very close to that obtained from simulations (4.21 kJ/mol compared to the experimental 4.44 kJ/mol). This correlation naturally applies to results calculated for other employed parameter sets as well. However, approximating a hexadecane molecule to be a single ideal spherical particle should naturally be questioned. Nevertheless, a long hydrocarbon chain has considerably more degrees of freedom than a single particle and thus the correction in a non-ideal case is smaller than that in the ideal case.

In addition to considering applying corrections to the numbers, we also performed a simulation of solvating 27 oxygen molecules into both solvents. This number of molecules in our simulation box gives a concentration very close to 1 M. The error estimates are naturally larger than when using only one oxygen molecule. The free energy difference per one mole of oxygen is, however, very similar to that calculated for the case of infinite dilution. This indicates that the mixing entropy due to different number of degrees of freedom in the two solvents is not much different and that the enthalpic contribution is efficiently screened by the solvent molecules. Due to the uncertain nature of the contributions of these factors, no corrections were applied to the obtained values.

Table 6.1: Comparison of the obtained parameter set, experiments and models employed earlier. “CHARMM” stands for the standard oxygen molecule of the CHARMM force field [168] with an added quadrupole moment [137]. σ and ε for this model are 3.03 Å and 0.523 kJ/mol. “Fischer” represents a model developed by Fischer and Lago [169] and employed in permeation studies by Marrink and Berendsen [8] and Sugii et al. [92]. The parameters for this model were 3.09 Å and 0.363 kJ/mol. Both density and heat of vaporisation are calculated at the boiling point of oxygen, 90.2 K.

Property	Experiments	Our model	CHARMM	Fischer
$\Delta G_{\text{water} \rightarrow \text{organic}}$ (kJ/mol)	−4.44	−5.29	−6.12	−5.48
Density (kg/m ³)	1141 [170]	1140	1198	1133
Heat of vaporisation (kJ/mol)	6.82 [170]	6.85	8.70	5.64

Comparison of other quantities between the models was also performed. The density at the boiling point (90.2 K) for the optimal parameter set was calculated to be 1140 kg/m³, which is very close to the experimental value of 1141 kg/m³ [170]. It is also slightly better than the values calculated for the earlier employed models as Table 6.1 suggests.

The heat of vaporization at 90.2 K was calculated to be 6.85 kJ/mol, while the experimental value is 6.82 kJ/mol [170]. Our model again performs better than the models employed earlier. The values are also listed in Table 6.1.

6.2 Oxygen Permeation

The results obtained from the permeation studies are listed in this section with comparison to experimental and computational studies. We present the free energy and diffusion profiles together with the permeation resistance profiles calculated from these two along the membrane normal. Their shape is explained based on density and free volume properties of the systems. The permeabilities of the monolayers at different compression are plotted with respect to their other physical properties in order to discover and validate the dependencies of permeability values on these quantities. The possible membrane structures supporting the lung surfactant monolayer are also evaluated based on their permeation properties.

6.2.1 Adequacy of Sampling

In order to enable us to consider the results to be trustworthy, we have to ensure that the oxygen molecule samples a reasonably large area in the xy plane at each constraint depth. Increasing the simulation time naturally improves sampling, but in some cases the oxygen molecule might get trapped in a small cage for a long time. Restriction of this kind might not be observed as larger error estimates of the obtained values. Sufficient sampling is also required to average the effects that might arise from the undulations of the membrane and local fluctuations in membrane thickness as well as to correctly account for the lipid composition of the system.

The positions of the oxygen molecule in the xy plane are shown in Fig. 6.2 for the monolayer system with $\langle A \rangle = 56 \text{ \AA}^2$. The data is extracted from the trajectory every 10 ps and the different colours represent the five different regions as indicated in Fig. 4.2.

While the oxygen molecule samples the whole area of the box in the low density tail region, the situation is quite different in the denser parts of the system. Regions 2 and 3 show pretty hindered movement whereas in region 1, which is abundant with water molecules, the sampling is again better. Nevertheless, the molecules do not seem to be trapped in any region and the simulations can be considered to be long enough to provide one with trustworthy statistics and a good description of the effects of the employed molecular composition.

6.2.2 Excess Free Energy Profiles

Here we present the excess free energy profiles and the mean force curves that these profiles are calculated from via Eq. (4.19). The bilayer system is used for comparison with other studies and data for one monolayer is also shown. All results are discussed with the aid of the “four region model” introduced in Section 4.3.

The excess free energy curve for the bilayer shown in Fig. 6.3 was integrated from

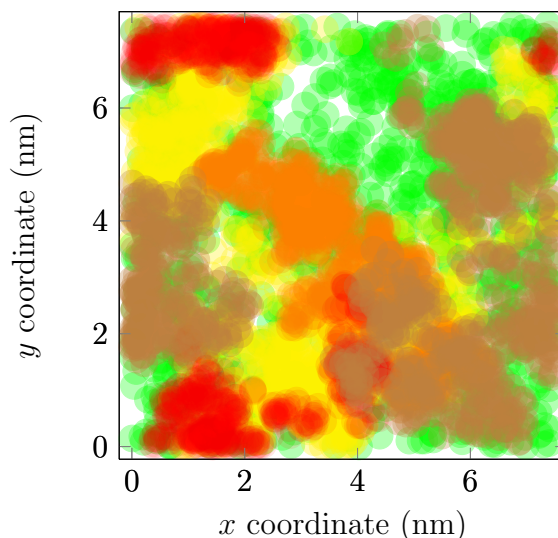


Figure 6.2: Scatter plots of the motion of the oxygen molecule in the xy plane constrained at different depths in the membrane. The data presents oxygen motion in the monolayer with mean molecular area equal to 56 \AA^2 . The colours represent oxygen movement at $z =$ ● 1.0, ● 1.5, ● 2.2, ● 3.0, and ● 3.5 nm from the start of the constraint MD calculations in the bulk water phase, that is in the regions from 1 to 5.

both sides of the membrane to the membrane core, and bulk water was used as the reference state with $\Delta G = 0$. The profiles shown here are not symmetrized so their mutual differences provide us with information about the size of the effect of heterogeneities between the two leaflets.

Since the z constraint method is effective in a way that it provides one with information on both kinetic and energetic contributions to permeation, it was employed for all the systems. However, its more refined counterpart, the umbrella sampling method, was employed on the bilayer system in the form of 20 ns long simulations per window to ensure the validity of the z constraint simulations. As Fig. 6.4 shows, the results of the methods agree well and the total free energy difference between the membrane core and water phase is almost identical.

As is seen in Fig. 6.3, when moving from the water region into the head group area, the mean force experienced by the oxygen molecules reaches its maximum value of almost 10 kJ/mol/nm as it is energetically very unfavourable for the hydrophobic oxygen to permeate through the region with high charge density. After passing through the head group region, the force changes sign and is of equal magnitude through region 2. In regions 3 and 4 the force is still negative but smaller, indicating that oxygen tends to move closer to the membrane core. In the very middle of the layers the mean force goes to zero, since the molecule experiences a force of similar size from the tails of both layers.

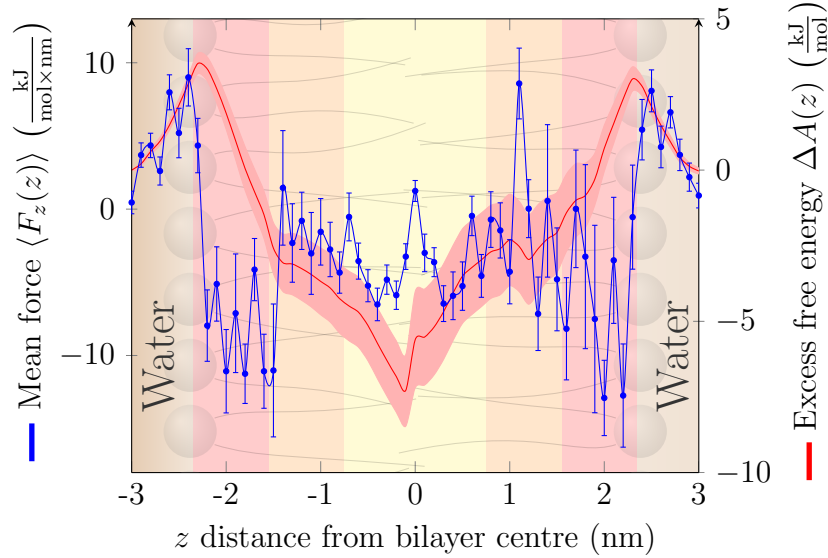


Figure 6.3: Mean force of the oxygen molecule in z direction in the bilayer system is drawn with $\text{---}\bullet\text{---}$ with error bars obtained from the block averaging method [165]. The integrated excess free energy is shown as --- with the error limits shown in filled light red area.

The energetics can be compared to other studies on oxygen permeation through a bilayer. The height of the energetic barrier in our study is a bit less than 4 kJ/mol, while in the membrane core the excess free energy gains its minimum value of about -7.3 kJ/mol. The average free energy value between the head group barriers is -3.4 kJ/mol.

These compare substantially well to other similar simulation studies. Hub and de Groot calculated a value of 4 kJ/mol for their barrier, while the minimum value of the free energy curve was about -7 kJ/mol [137]. They employed the CHARMM force field parameters for oxygen which also had a quadrupole moment. The bilayer was made of POPE lipids and simulated at 300 K.

CHARMM parametrization was also used in the study by Shinoda et al. in their study on a DPPC bilayer at 323 K [98]. The values they found for the head group region barrier and membrane core minimum were about 3 and -8 kJ/mol, respectively. Slightly larger value of about -10 kJ/mol was obtained for the minimum of the excess free energy profile in a study on dimyristoylphosphatidylcholine (DMPC)/cholesterol membranes at 310 K employing Monte Carlo simulations [171]. Cholesterol mole fraction was not seen to substantially affect the profiles, and a barrier was observed in the head group region [171].

The O_2 parametrization by Fischer and Lago was employed by Sugii et al. in their study on a DPPC bilayer at 320 K [92]. They obtained values of 4 and -8 kJ/mol for the barrier and the core, respectively. Marrink and Berendsen did not observe

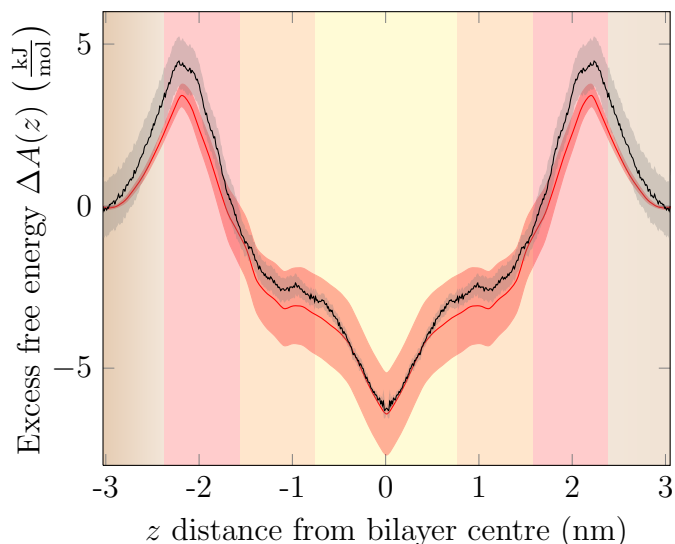


Figure 6.4: Comparison between the pulling methods: —: constraint MD method, —: umbrella sampling method. Profiles are symmetrized and error bars are shown in the lighter shade of the respective colour. Calculation is performed either from membrane core outwards or the other way and thus the errors accumulate in the different ends of the curve over one leaflet.

a barrier for oxygen in the head group area in their study on a DPPC bilayer at 350 K [8]. The free energy in the membrane core, -8.5 kJ/mol, was also slightly lower compared to most other studies [8]. These effects might be due to their higher simulation temperature, their charge-free oxygen molecule, different lipid composition, or the fact that they reduced the charges on lipid molecules suggested by the GROMOS force field to half of their original values.

However, as the key values from various studies agree with those obtained from our simulations, the validity of the results of Marrink and Berendsen has to be questioned. As the free energy barrier in the head group region obtained from umbrella sampling is even higher than that obtained from the z constraint method, we can conclude that it is clearly not an artefact of the employed methodology.

Al-Abdul-Wahid et al. measured values of -4.0 and -5.1 kJ/mol for the partitioning of an oxygen molecule into a MLMPC (DMPC with a perdeuterated sn-2 chain) bilayer at 298 and 318 K using NMR spectroscopy [97]. These numbers lie between the values we obtain for the minimum free energy and the average free energy between the barriers. In their other study, Al-Abdul-Wahid et al. measured a minimum value of -5.8 kJ/mol and an average value of -3.0 kJ/mol for their MLMPC bilayer at 318 K [10]. Their values were calculated from oxygen concentration profiles obtained from MD simulations of free oxygen molecules [10].

Smotkin et al. measured a partition coefficient of 4.9 ± 0.8 for DMPC liposomes and water and this value translates to $\Delta G = -4.1$ kJ/mol [172]. A similar value was

obtained by Power and Stegall who measured a partition coefficient of 5 ± 4 between water and red blood cells [173].

Jedlovsky and Mezei calculated a free energy difference of 12.4 kJ/mol between water and hydrocarbon phases for a DMPC bilayer at 310 K using a cavity insertion Widom method and CHARMM parametrisation [174]. This is much larger than our value and not in line with other studies.

Our results agree well with other studies regardless of the differences in lipid composition and temperature. Knowing this, we can proceed to investigate the monolayer systems. Throughout the discussion, the system with mean area equal to 56 \AA^2 will be used as a reference since it is the midmost regarding the area. The mean force and excess free energy for this system are plotted in Fig. 6.5. Here water is used as the reference state of the free energy. However, when calculating the permeabilities from gas phase to water, the reference is switched to the side of the gas phase.

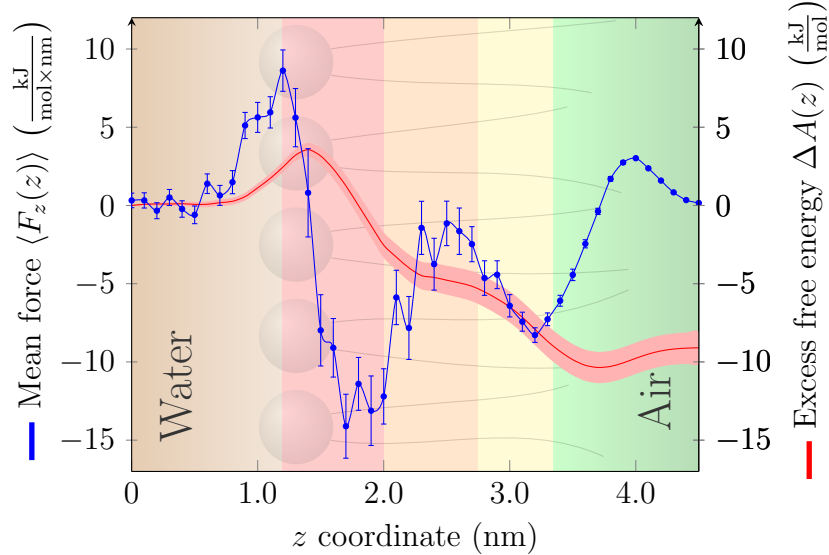


Figure 6.5: Mean force in z direction of the oxygen molecule in the monolayer system with $\langle A \rangle = 56 \text{ \AA}^2$ is shown in \bullet with error bars obtained from the block averaging method [165]. The integrated excess free energy is given in — with the error limits shown in filled light red area.

The profiles are very similar to the bilayer ones both in shape and values. The minimum free energy is somewhat lower than in the case of the bilayer, but that is explained by the occurrence of the fifth region with a really low density, which is not present in bilayers as explained in section 4.3. The shapes and key values of the profiles of other monolayer systems were very similar to those of the system with $\langle A \rangle = 56 \text{ \AA}^2$ and are not shown here. This fact is also justified by the fact that free energy is a state function and thus the free energy difference between bulk water and

air should be independent of the state of the monolayer residing between these two phases.

6.2.3 Entropic and Energetic Components

Since we calculated the free energies at various temperatures, we can separate the entropic and energetic components. Since the energetic component is independent of temperature, and all the temperature dependence is included in the entropic term. This approach was used successfully in a computational study by MacCallum and Tieleman [122].

By using three separate temperatures, an easy formula for the components can be obtained simply by approximating the partial derivative by the difference quotient and assuming that the dependence is linear in the interval from $T - \Delta T$ to $T + \Delta T$. The entropic component is obtained from

$$-T\Delta S = \left(T \frac{\partial A}{\partial T} \right)_V \quad (6.2)$$

$$\approx \frac{T}{2\Delta T} (A(T + \Delta T) - A(T - \Delta T)). \quad (6.3)$$

Then the internal energy part of the free energy is easily calculated from the definition of the Helmholtz free energy as

$$U = A + TS. \quad (6.4)$$

In Fig. 6.6 the energetic and entropic contributions on free energy at 310 K are shown. The calculation is performed with two temperature pairs, namely with 300 and 320 K and then with 305 and 315 K, that is, with $\Delta T = 5$ K and 10 K.

Based on these curves it is impossible to give accurate statements about the profile since the error limits are large. However, the entropic component is positive and the internal energy negative for both temperature pairs when moving from water to the membrane core. In their study, Al-Abdul-Wahid et al. obtained a negative entropic contribution of $-T\Delta S = -17.2 \pm 1$ kJ/mol and a positive enthalpy of $\Delta H = 12 \pm 0.9$ kJ/mol for oxygen partitioning into a DMPC lipid bilayer at 318 K [97]. In an extra series of umbrella sampling simulations performed on the bilayer system at 295, 310 and 325 K, we observed that the conclusions drawn from the results were completely opposite as the enthalpy change of moving the oxygen from water to the membrane core was positive. The simulation time at each z value was sufficient (20 ns) and the discrepancies could not be explained with the error margins. All in all, it is still uncertain whether this partitioning process is really driven by enthalpy or entropy as discussed in section 4.4. It seems that the outcome of the

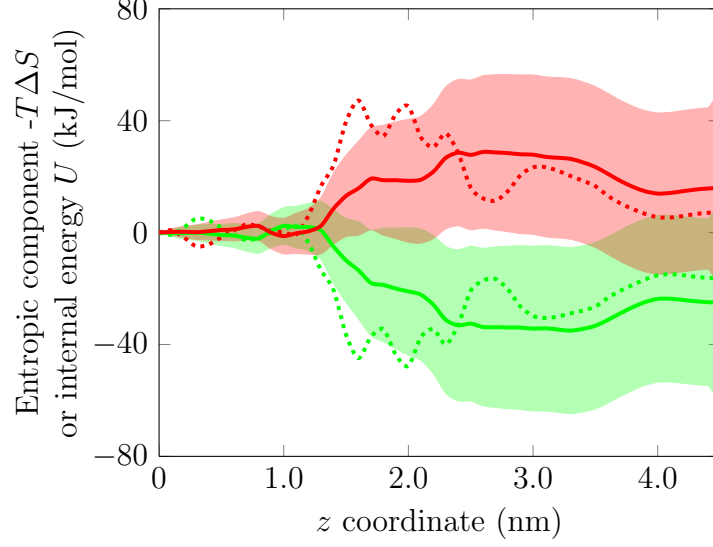


Figure 6.6: Entropic and internal energy components of the excess free energy along the z coordinate for the monolayer with $\langle A \rangle = 56 \text{ \AA}^2$. Entropy calculated from the systems with $T = 300$ and 320 K is given in — and internal energy from the same pair of systems in — with their error limits shaded. Curves obtained for the pair of $T = 305$ and 315 K are given with dotted lines of the same colours.

analysis is highly dependent on the method employed in the free energy calculation, and it is also possible that the simple model for the permeating molecule does not correctly capture all the entropic effects. To summarize, our results support neither the existence or non-existence of the non-classical hydrophobic effect.

6.2.4 Local Diffusion Coefficients

Local diffusion coefficients in z direction were extracted from the force autocorrelation curves by first performing a double exponential fit and then integrating this obtained equation analytically from 0 to infinity as presented in [8, 83, 99, 116]. The fitted function is of the form

$$C(t) = A_0 \exp(-t/\tau_0) + A_1 \exp(-t/\tau_1), \quad (6.5)$$

where A_0 and A_1 are prefactors and τ_0 and τ_1 are the decay times of the correlation of the fast and slow motions of oxygen molecules in the membrane. The decay times τ_0 and τ_1 were observed to have values of around 0.1 ps and 10 ps, respectively. The fit was performed from the beginning of the autocorrelation curve up to the time at which the function had decreased to $1/10000$ of its initial value. For the oxygen molecule in the water phase the fit provided two very similar time constants of about 1 ps, indicating only one decay mode. The diffusion coefficients in xy direction were

obtained from MSD curves by a linear fit in the time interval from 0.1 to 1 ns.

The spatial dependence of the local diffusion coefficient in the bilayer system is plotted in Fig. 6.7, and respective data on one monolayer system is shown in Fig. 6.8. Both the diffusion coefficient in xy plane and in z direction are plotted in both cases to show that the values are very similar, therefore diffusion displays isotropic behaviour in the case of small permeants like oxygen. This fact justifies the comparison between the calculated D_z values with the experimental ones in which oxygen is free to diffuse in all directions. The error bars are also drawn. For D_{xy} , they are obtained from the output of the `g_msd` program included in the GROMACS package. For force autocorrelation, the error bars were obtained by dividing the simulation into 4 or 5 equally long parts. The fitting process was performed separately on each of these and error bars represent the standard deviations of these obtained values. The error bars are mostly acceptably small.

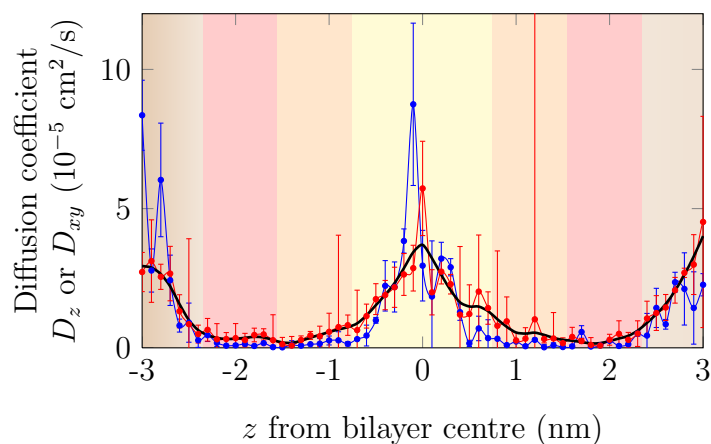


Figure 6.7: Diffusion coefficients within the bilayer obtained from the two methods. —•—: $D_{xy}(z)$ calculated from the mean squared displacement, —•—: $D_z(z)$ obtained from the force autocorrelation method, and —: smoothed version of the latter one employed in the permeability calculations.

In water phase the diffusion coefficient obtains a value of about $(3-4) \times 10^{-5} \text{ cm}^2/\text{s}$. Comparing this value with experiments is a good benchmark for our fitting procedure. Han and Bartels measured values of 2.52 and $2.78 \times 10^{-5} \text{ cm}^2/\text{s}$ at 308.1 and 313.2 K respectively [175]. A slightly larger value of $3.33 \times 10^{-5} \text{ cm}^2/\text{s}$ was obtained at 313.15 K [176]. Krieger et al. found a diffusion coefficient of $3.49 \pm 0.24 \times 10^{-5} \text{ cm}^2/\text{s}$ at 302.75 K [177]. These are all in fairly good agreement with our values on oxygen diffusion in the aqueous phase.

Fig. 6.7 clearly shows that as we advance deeper to the membrane, diffusion gets drastically slower reaching values as low as $(0.1-0.3) \times 10^{-5} \text{ cm}^2/\text{s}$ in regions 2 and 3. In region 4, however, the density and charge density of the hydrocarbon tails are so low that the diffusion is about one magnitude faster. We calculate $2.3 \times 10^{-5} \text{ cm}^2/\text{s}$

to be the average value within region 4, which resembles a system comprised of pure alkanes. This value is slightly lower than that of oxygen in water.

Our values are again fairly close to those obtained in other studies. Ju and Ho measured a value of $2.49 \times 10^{-5} \text{ cm}^2/\text{s}$ for oxygen in n-hexadecane at 295.15 K, which is 18% larger than the value they obtained in water [178]. A similar value of $2.66 \times 10^{-5} \text{ cm}^2/\text{s}$ was measured by Kowert and Dang for n-hexadecane at 298.7 K [143]. McKinnon et al. reported values of 2.6 ± 0.2 and $3.6 \pm 0.3 \text{ cm}^2/\text{s}$ for a simulated hexadecane monolayer at 300 K with 0% and 10% molar cholesterol concentration, respectively [9]. Fischkoff and Vanderkooi obtained values in the range from 1.56 to $6.8 \times 10^{-5} \text{ cm}^2/\text{s}$ in the temperature interval from 298 to 318 K, with a value of $4.1 \times 10^{-5} \text{ cm}^2/\text{s}$ at 310 K [9]. The average diffusion coefficient in the membrane interior obtained by Al-Abdul-Wahid et al. in their simulation of an MLMPC membrane at 318 K was $3.7 \times 10^{-5} \text{ cm}^2/\text{s}$ [10]. The diffusion coefficient profile obtained by Marrink and Berendsen shows somewhat larger values for all regions due to their higher simulation temperature and reduced charges in the lipids [8]. However, the minimum value they obtained is close to $2 \times 10^{-5} \text{ cm}^2/\text{s}$, which is one magnitude larger than our values. This might also be explained by the differences in lipid compositions, especially the lack of cholesterol in their model membranes.

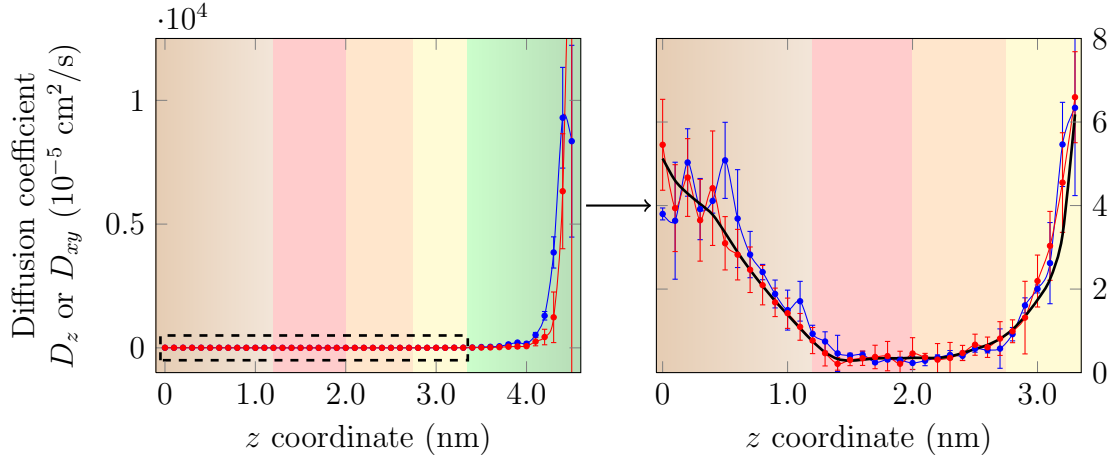


Figure 6.8: Local diffusion coefficients obtained by two methods for the system with $\langle A \rangle = 56 \text{ \AA}^2$. \bullet represents the $D_{xy}(z)$ obtained from a linear fit to the MSD data while \bullet stands for the $D_z(z)$ obtained from the integration of the force autocorrelation. — represents the smoothed version of the latter curve and the smoothed version is used for further calculations. The figure on the left shows data from the range of the whole system, and the values are very large in and near the air phase. The figure on the right shows data in more detail in the interesting domain, ranging from the water phase to the tail region.

Fig. 6.8 shows that diffusion in a monolayer follows the same guidelines as diffusion in a bilayer. The curves are similar in both shape and values. In the monolayer

system diffusion speeds up drastically towards the air phase. Actually in the air phase, the mean squared displacement curves are no longer linear since the oxygen molecule experiences ballistic unhindered motion. The very large diffusion coefficients in region 5 with very low density are not of large interest since the contribution of these z locations to the permeation resistance, Eq. (4.11), is diminishing.

Examples of both force autocorrelation and mean squared displacement curves for oxygen molecule at different depths in the monolayer are shown in Fig. 6.9, with an objective to show that their shape is physically correct. Force autocorrelation decays with two time constants and the MSD curves show linear behaviour in the time scale of fitting.

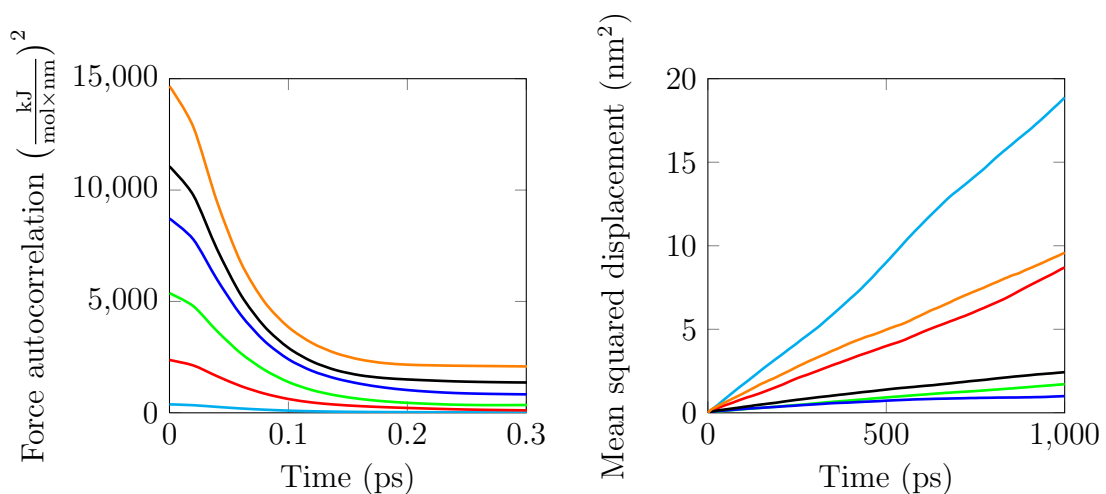


Figure 6.9: Examples of force autocorrelation and MSD curves from which the local diffusion coefficients are obtained through integration and linear fitting. They represent the monolayer system with $\langle A \rangle = 56 \text{ \AA}^2$. The colors stand for systems in which the oxygen molecule is constrained at different depths in the membrane measured from the starting value in the water phase as —: 0.5 nm, —: 1.0 nm, —: 1.5 nm, —: 2.0 nm, —: 2.5 nm, and —: 3.0 nm.

In order to compare the diffusion rates in monolayers at different compressions, we calculated the average diffusion coefficients in each region. The regions for each system were determined from density profiles, and their comparison is easier than real diffusion profiles due to the differences in membrane thickness. These data are presented in Fig. 6.10 on a logarithmic scale.

Diffusion rates are close to each other in region 1 since it is fairly similar to bulk water independent of the compression state of the monolayer. Diffusion slows down considerably in region 2 and gets somewhat faster in region 3. In region 4 diffusion is much faster, as expected. The plot shows that the diffusion coefficients are closely related to mean area per molecule and at least in the densely packed regions we

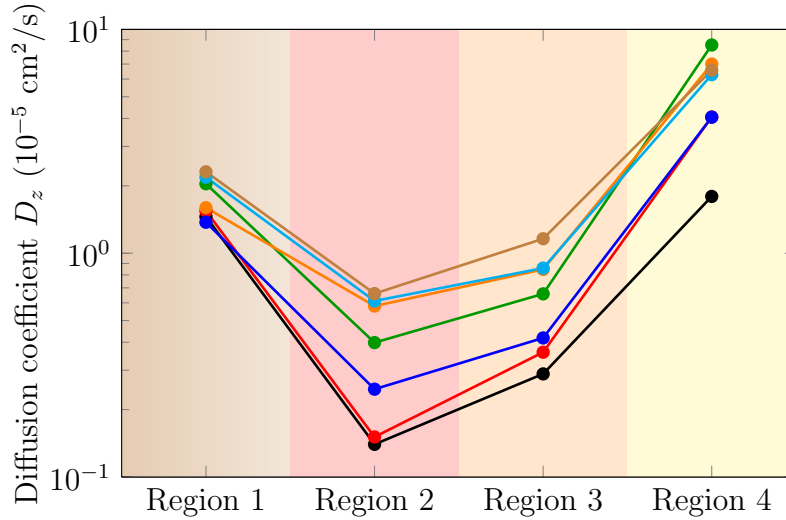


Figure 6.10: Average diffusion coefficients in different regions. Different curves represent monolayers at different compressions. —: 44 Å², —: 48 Å², —: 52 Å², —: 56 Å², —: 60 Å², —: 64 Å², and —: 68 Å².

can conclude that oxygen in the more expanded systems diffuses around 5 times faster than in the compressed ones. The comparison in regions 1 and 4 is a little questionable since both of these regions cover a range of diffusion coefficient values. In region 1 diffusion gets slower when moving into the membrane from bulk water as the perturbation caused by lipid head groups becomes more prominent. The inverse phenomenon takes place in region 4 as diffusion coefficients quickly grow when the membrane gets less dense towards the ends of the hydrocarbon tails.

6.2.5 Permeation Resistance Profiles

The local permeation resistance profile for the bilayer obtained from free energy and local diffusion coefficient profiles through Eq. (4.11) is presented in Fig. 6.11. Resistance to permeation is largest in region 2 and decreases significantly in the membrane core. The profile is very different from the one obtained by Marrink and Berendsen as their profile reaches its maximum value in the aqueous phase [8]. This difference is due to two factors. To begin with, our free energy profile has a peak in the head group region while the profile of Marrink and Berendsen never obtains values higher than those in bulk water. Additionally, diffusion coefficients in their membrane are drastically higher in the head group region. These might arise from the issues discussed earlier, namely simulation temperature, lipid composition and the reduction of the lipid charges.

To exclude one possible source for this high resistance barrier, we simulated the system with $\langle A \rangle = 56$ Å² at 310 K but with the charges of our oxygen model

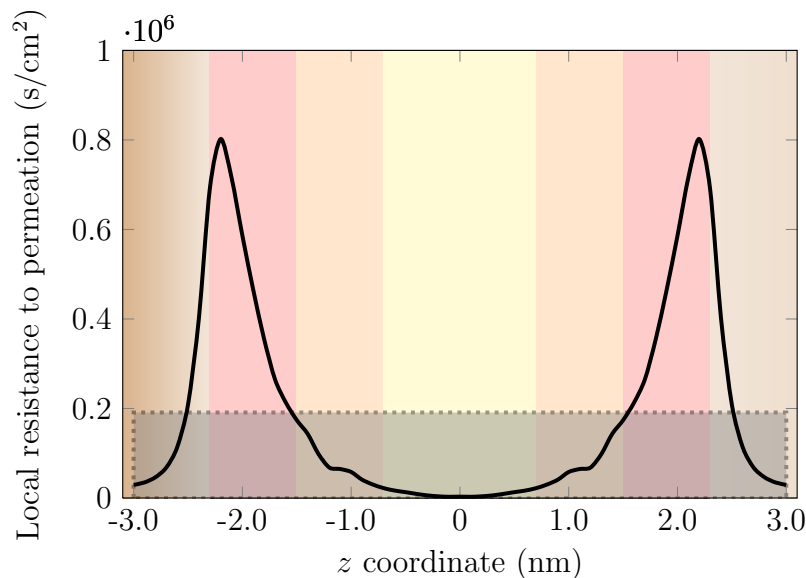


Figure 6.11: Symmetrized local permeation resistance of the bilayer. The grey box shows the resistance profile following the homogeneous solubility–diffusion theory that produces the same permeability.

discarded. The change in the excess free energy profile diminished but diffusion was slightly enhanced within the membrane. This caused the permeability resistance barrier to decrease by about 30% and the permeability to increase by about 20%. However, the barrier within region 2 was still substantial. Therefore, it cannot be explained by the charges in the oxygen molecule.

There is experimental evidence for the existence of the permeation barrier within the head group region. In their series of studies, Subczynski et al. studied the variation of the oxygen transport parameter, which is inversely proportional to the local permeation resistance [5, 138, 139, 142, 147]. They observed that this profile reached its minimum value in region 2 for membranes with cholesterol [5]. In another paper they found that the head group region acts as a moderate permeability barrier in cell membranes [139]. This was also proposed in the original inhomogeneous solubility–diffusion model paper to be the case for hydrophobic molecules [11].

In addition to the local permeation resistance profile which was obtained based on the inhomogeneous solubility–diffusion model, we have plotted a curve representing the profile according to the homogeneous version of the model which produces the same total permeation resistance value when integrated over the membrane (see Fig. 6.11). Simplifying, this corresponds to the average value of the resistance profile and it is notably higher than the resistance of the aqueous phase, thus supporting the view that biological membranes slow down oxygen permeation compared to bulk water.

The local permeation resistance profiles for the monolayer systems are plotted in Fig. 6.12 for both directions according to Eq. (4.14). The constant B , the shift in energy due to the change of the reference point to the air phase, was calculated to have an average value of 9.67 kJ/mol in the monolayer systems. The average shift was employed since the total free energy difference between water and air phase should be equal in all systems. The obtained scaling factor, $\exp[9.67 \text{ kJ/mol}/(RT)]$, has a numerical value equal to 42.6. The curves are also shifted in z direction so that the maximum values are horizontally aligned with $z = 0$ corresponding to the location of the maximum.

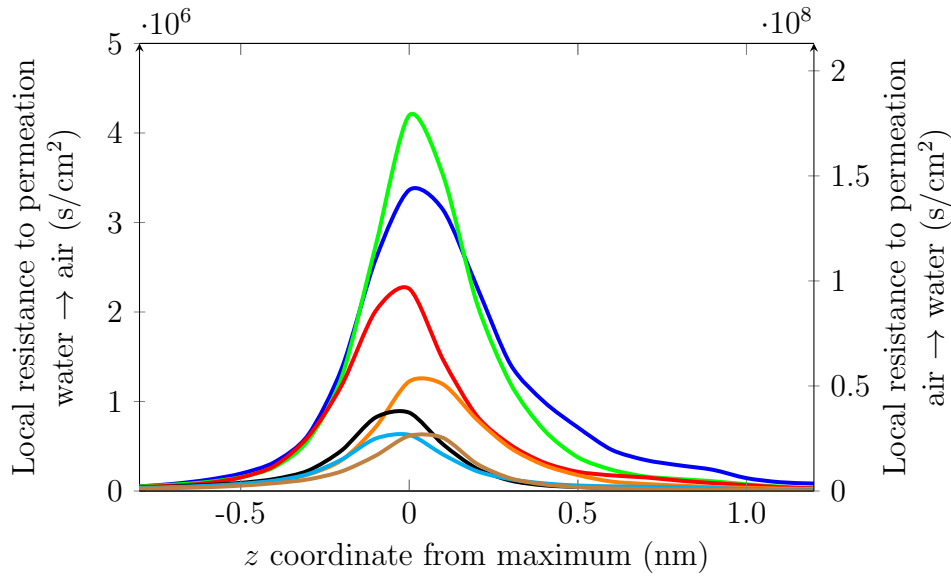


Figure 6.12: Permeation resistance plots for the monolayer systems. The plots are shifted in z direction for better comparison. Different colours represent different compression stages with —: 44 Å², —: 48 Å², —: 52 Å², —: 56 Å², —: 60 Å², —: 64 Å², and —: 68 Å².

We can readily conclude that the heights of the resistance barriers follow the expected tendency that a more compressed system induces a higher hindrance for the motion of oxygen through the membrane. However, the barrier of the most compressed system is not the highest. A possible explanation for this is that the membrane is not completely planar and thus the resistance of region 2 is a little spread over a range of z values. The preferred location of cholesterol molecules in the monolayer might also change with varying mean area per molecule. At higher molecular areas cholesterol is located in a manner similar to that of phospholipids, yet it is pushed down to the tail region when the monolayer is compressed. The fact that the total permeation resistance systematically follows the area per molecule value supports these ideas.

6.2.6 Total Permeation Resistances and Permeabilities

The total permeation resistance of a membrane can be obtained from the local permeation resistance profiles by integration as suggested by Eq. (4.12). The permeability in turn is given by the inverse of this integral as proposed by Eq. (4.13). The integrals were performed in the z range that was considered to belong to the membrane. The criteria was set so that if the density of the lipids exceeded a value of 10 kg/m^3 at a certain depth, it was included in the integration.

The integrated value for the bilayer was 8.7 cm/s . For monolayers the permeability values for the process of going from water to air phase ranged from 5.2 to 34.4 cm/s , increasing monotonically with increasing area. The values in the opposite direction, from air phase to water are obtained by dividing these values by 42.6 as suggested by Eq. (4.15). This results in permeabilities in the range from 0.12 to 0.81 cm/s . The permeability of the bilayer obtained by integrating only over regions 3 and 4 was 72 cm/s . The value obtained from employing the homogeneous solubility–diffusion model and the average values of diffusion coefficient and free energy difference over the whole bilayer was 36 cm/s . There are various studies in both experimental and computational fields that have measured the permeability coefficients in both bilayers and monolayers, and the values obtained in these studies are very diverse depending not least on the direction in which the permeation is measured.

Subczynski et al. calculated the permeability of the Chinese hamster ovary membrane at different temperatures and obtained values of 7.2 , 21.1 and 42.0 cm/s at 283 , 293 and 310 K , respectively [139]. In their other study, Subczynski et al. measured oxygen permeability through DMPC and DOPC membranes at various temperatures with cholesterol molar concentrations of 0 and 50% [5]. At 303 K the permeabilities they obtained for DOPC were 114 and 54.6 cm/s for systems without and with cholesterol, in respective order, and they increase significantly with temperature. The values for the DMPC membranes are lower both with and without added cholesterol [5]. In their yet another study on the effect of chain unsaturation and cholesterol intercalation, Subczynski et al. found permeabilities of 15.0 , 32.5 and 201.5 cm/s for EYPC membranes at 283 , 293 and 310 K , respectively. With $50 \text{ mol-}\%$ of cholesterol, the values decreased to about one third of these [147]. The effect of cholesterol concentration on the permeability was seen to be linear [147]. Dzikovski et al. calculated a value of 210 cm/s for their DMPC bilayer at 312 K combining data from their solubility–diffusion profiles together with other experimental results [179]. In a study on thylakoid membranes, Ligeza et al. measured a value of 39.5 cm/s for oxygen permeability at 293 K [138].

A simulation by Marrink and Berendsen revealed similar values. For their DPPC membrane at 350 K a value of $200 \pm 500 \text{ cm/s}$ for the whole membrane and 1500 ± 400

cm/s for regions 3 and 4 only was obtained [8]. This value together with the experimental ones listed above are higher than those we obtained. However, many other studies suggest a drastically smaller value for O_2 permeation through biological membranes.

In their study on DPPC monolayers at very high compression in the limit of no domain boundaries, Borden and Longo found a value of 2.1×10^{-3} cm/s for the permeability of oxygen from air to aqueous phase [7]. This value rises linearly with domain boundary density, and with the observed systems a maximum increase of about 50% was measured [7].

Ivanov et al. measured oxygen permeability for a range of monolayers at different compressions [6]. For a DPPC monolayer with applied surface pressure equal to 30 mN/m a value of $4.3 \pm 0.58 \times 10^{-3}$ cm/s was found. Similar values were also calculated for a TLPS monolayer. At surface pressures from 4 to 18 mN/m, permeabilities from 1.25×10^{-2} to 2.33×10^{-3} cm/s were measured. All measurements were again performed from the air phase towards the water phase [6]. Strutwolf et al. measured a value of 1.4×10^{-2} cm/s at ambient temperature for their compressed DOPC monolayer [105]. However, the values for DPPC and DMPC monolayers were much higher. The permeability was measured from the organic phase towards the water phase.

Since no data is available in which monolayer permeability is measured from the aqueous phase towards vacuum, the comparison between monolayers and bilayers is not trivial. However, these two membrane structures are in many ways similar. The mean area per molecule for the simulated bilayer system was 50.3 \AA^2 and the interpolated permeability value for a monolayer with similar area was 7.4 cm/s. The process of permeating two successive monolayers of this kind result in a permeability of 3.7 cm/s. This is smaller than the value obtained for the bilayer indicating some differences in membrane variables.

Another reason for the large experimental permeabilities in bilayers might be the fact that the employed probes do not often reside in the head group region and thus the effects of this region are approximated. In the studies listed above, the resistance in the head group region was either estimated with a linear interpolation from aqueous phase to the beginning of the hydrocarbon region thus fully omitting the possible barrier in the head group region [138, 139] or a single probe was inserted between the aqueous and hydrocarbon phases [5, 147]. Dzikovski et al. calculated the permeability based on probes only inserted to the hydrocarbon tails from 4th to 14th carbon atom thus wholly neglecting the head group region [179]. The values obtained for the bilayer in this study is actually fairly close to the experimental ones if only regions 3 and 4 are considered. Another issue is that the insertion of these probes induces defects in the membrane structure that might locally alter the permeability

drastically.

On the other hand, it is possible that a fully condensed (solid) monolayer is not a valid description of the lung surfactant. Therefore, the comparison of the results of Borden and Longo with ours should be avoided [7]. Ivanov et al. suggested that the low permeabilities compared to water observed in some studies are due to the high microviscosity of lipid membranes [6]. It might be that the united atom model employed in our study does not correctly reproduce this effect. In the study by Marrink and Berendsen the free energy profile was different to those obtained in other computational studies and thus their permeability value must also be taken with a grain of salt.

The direction seems to play a large role in the permeability of monolayers. This is also suggested by the inhomogeneous solubility–diffusion model as the change in the standard state of the free energy drastically changes the local permeation resistance values. Experiments must also be conducted with extreme care in order to prevent the formation of membrane structures other than the monolayer itself in its vicinity. These structures might have greatly different permeabilities compared to pure water and they could be connected to the monolayer in a manner which prevents the need for the oxygen molecules to actually pass through the high-resistance head group region. Qualitatively our results point out that the head group region acts as a barrier for oxygen permeation and that membranes slow down permeation compared to pure water.

6.2.7 Dependence of Permeability on Physical Quantities

To take into account the possibility that an alveolus has a smaller surface area when it is empty compared to its expanded state, we scale the permeabilities by the fraction of the area of the system and that of the most compressed system as $\mathcal{P}_{\text{scaled}} = \frac{A}{44 \text{ \AA}^2} \times \mathcal{P}$. The scaling factor has a value of 1 for the most compressed system and a value of $68/44 = 1.55$ for the most expanded system. This way we can inspect a system of a fixed amount of surfactant molecules rather than one of fixed area. This is required since the total number of oxygen molecules permeating the studied system in unit time is obtained as the product of permeability with the available surface area and concentration difference between the sides of the system. However, the effect of the concentrations is not discussed here.

The dependence of permeability on the mean area per molecule is represented in Fig. 6.13. Since the data for the most compressed system showed some artefacts, we have performed fits to both the whole range of molecular areas and then to a set from which the most compressed system is left out.

Regardless of whether the most compressed system is included or not, the permeabilities clearly show linear dependence on the mean molecular area. Mathai

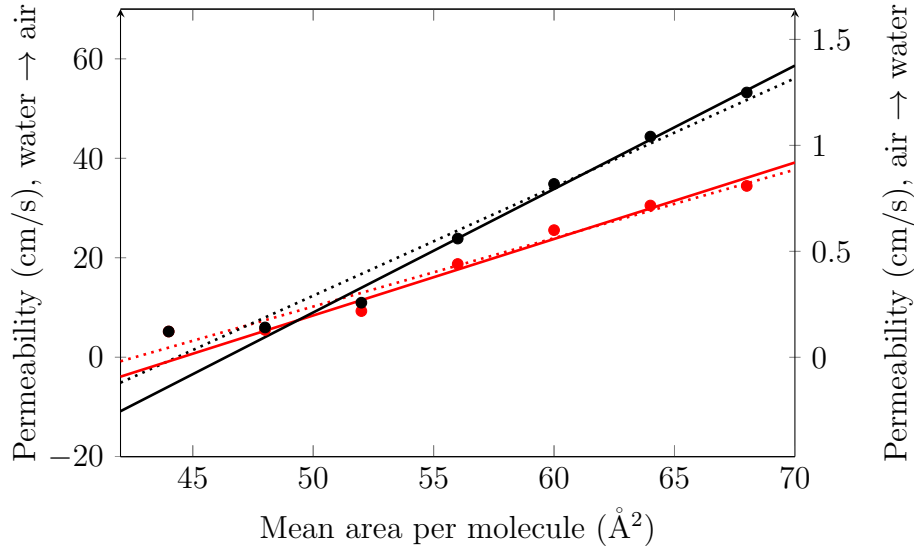


Figure 6.13: Permeabilities of the monolayer system versus area. • represent the absolute values, while • are scaled with area. The lines show fits to all data points (.....,.....) or to those other than the most compressed system (—, —)

et al. also found a linear dependence between the permeability of water through lipid bilayers and the mean area per molecule [86]. Ladanyi et al. found a two-fold increase in oxygen transport through a DPPC monolayer when the area per molecule varied by 30% [4]. This observation, roughly in line with our results, is due to both faster kinetics and increased area for permeation [4].

The dependence of permeability on the monolayer thickness is presented in Fig. 6.14. The thickness is calculated as the mean distance between the phosphate atom and the terminal carbons in the acyl chains. Two mathematical descriptions are tested by fitting curves with permeability depending either exponentially or inversely on the monolayer thickness.

We notice that both fits are acceptable. The exponential formula performs better in the whole data range while the points other than the most compressed system (the one with largest thickness) are better characterised by the fit in the form of $1/d_c$. If the volume of the molecule is approximately constant, then a linear dependence on the mean molecular area should naturally lead to permeability being inversely related to the thickness. In our case of fixed lipid composition, it is fair to expect this to be the case. This was also the conclusion in the study by Mathai et al. [86], which is further supported by the formulation of the homogeneous solubility–diffusion theory. Exponential dependence was observed in some studies [7, 93], while some suggest smaller dependence [92]. The small thickness range that these fits are applied to enables many formulations to match the data well, and a justified decision between them cannot be made.

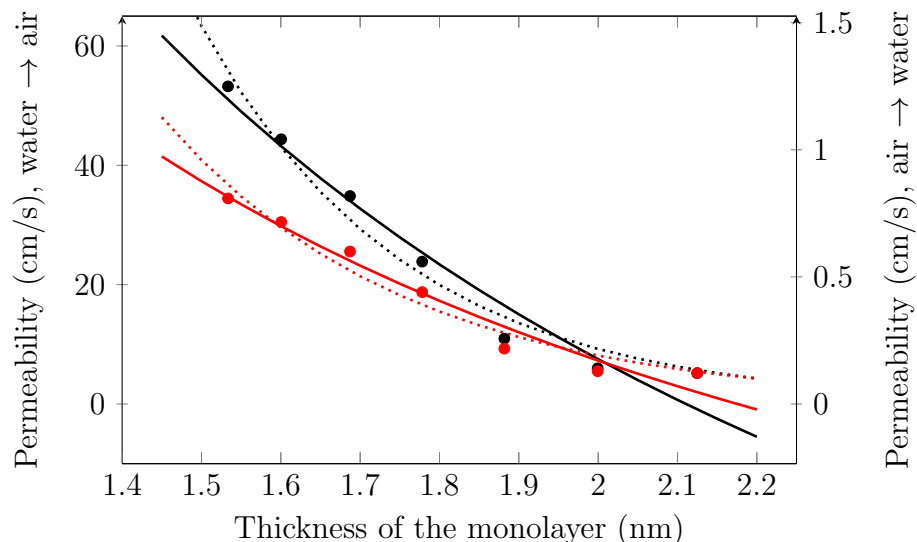


Figure 6.14: Permeabilities of the monolayer system versus the thickness of the monolayer (•,•). The fits are either of the form $\mathcal{P} \sim 1/d_c$ (—, —) or $\mathcal{P} \sim \exp(-\alpha d_c)$ (.....,). Again red color stands for unscaled and black for scaled values.

The dependence of permeability on surface tension is represented in Fig. 6.15 again with both scaled and unscaled values. Surface tension was calculated from the pressure tensor employing the `g_energy` supplied with GROMACS package in the form of $\gamma = [P_{zz} - \frac{1}{2}(P_{xx} + P_{yy})] / N_s$. Here P :s stand for the elements of the pressure tensor and N_s is the number of surfaces in the system (2 in our case).

Fits are again performed to both scaled and unscaled values and they seem exceptionally good. This supports the views of Ciani et al. [96] and Cannan et al. [149], while it is in contrast with some other studies [3, 150]. Phase behaviour and other factors may change these results between different lipid types and techniques.

6.2.8 Comparison to Density and Free Volume Profiles

In order to better understand the free energy, diffusion and permeation resistance profiles, their shapes can be related to the density profiles of different components of the system. The model that divides membranes into separate regions is also supported by these profiles. It has been suggested that diffusion is closely related to the free volume properties [97, 180]. Both the density and free area profiles are plotted for the monolayer with $\langle A \rangle = 56 \text{ \AA}^2$ in Fig. 6.16. The free energy and diffusion coefficient profiles found in Sections 6.2.2 and 6.2.4 are not included in this figure for clarity.

The peak in the excess free energy plot occurs at a depth at which the total density of the system is the highest. In this region the density of charged head groups also reaches its maximum value. The density of water is also substantial here.

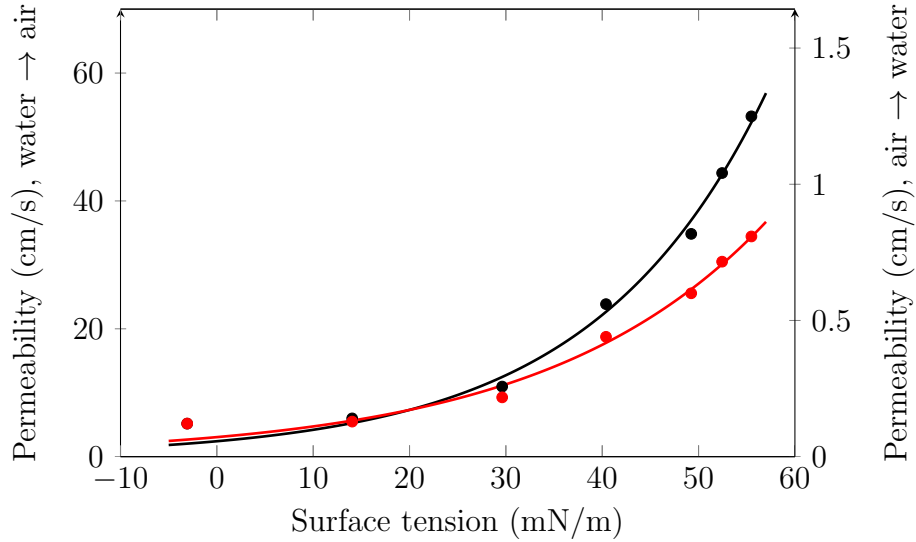


Figure 6.15: Permeabilities of the monolayer system the versus surface tension of the monolayer. The fits are performed in the form of $\mathcal{P} \sim \exp(\alpha\gamma)$. • and — stand for the unscaled values while • and — ones show data for the scaled ones.

When moving deeper into the membrane, the shape of the free energy curve follows that of the lipid density. The diffusion coefficient profile can also be linked to the density profiles. Its value seems to follow the total lipid density rather than the total density. This is somewhat surprising as one would assume the tail region to pose very little resistance to diffusion. However, diffusion in the beginning of the tail region with glycerol groups is much slower than diffusion in water phase. The correlation between the shape of the free area profile and the diffusion coefficient profile can also be seen. The regions 2 and 3 with the lowest free area also have the lowest diffusion coefficients. Precise arguments on the dependence of diffusion coefficients on free volume distributions cannot, however, be made and the existence of a linkage between these two is still under debate [83, 98].

6.3 Free Oxygen Molecules

In order to compare the separate monolayer systems and to investigate the realistic free movement of oxygen within membranes, simulations with unconstrained oxygen were also performed. Their motion within the membrane was monitored and some chosen trajectories are shown in Fig. 6.17, with the bottom part representing the gas phase. The coordinates were saved every picosecond.

It is seen that oxygen spends more time within a more compressed membrane. The motion seems to resemble what is referred to as “rattling in a cage” as the permeating molecule stays in a small volume for a considerably long period. This

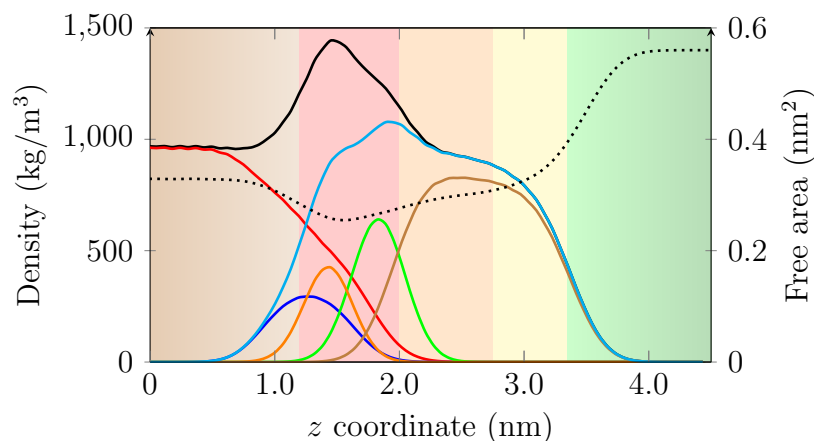


Figure 6.16: Mass density and free area profiles of different components for the monolayer system with $\langle A \rangle = 56 \text{ \AA}^2$. The different components are given with —: head group, —: glycerol group, —: phosphate group and —: hydrocarbon tails. Density of the whole system is drawn in —, water in — and total lipid density in —. stands for the free area profile that is normalised so that it shows the free area per lipid molecule

effect is clearly emphasized in the more compressed systems. The rattling seems to occur at same depths regardless of the compression state. Hindered motion is seen both at the surface of the membrane and deeper, ranging through the glycerol and phosphate regions where head group density is still prominent.

6.4 Permeation below the Surfactant Monolayer

With the results obtained above we can also discuss the possible routes of oxygen molecules below the surfactant monolayer in the light of the studies discussed in Section 2.3. We will employ the same key ideas as Åberg et al. did in their study [53]. However, both partitioning coefficients and diffusion coefficients are obtained from our simulations so our natural choice is to employ these values in the calculations.

Permeation through stacked bilayers involves passing the homogeneous water region and the very inhomogeneous bilayer. The permeability through the bilayer was calculated to be 8.7 cm/s which translates to a total resistance of 0.11 s/cm in the 6 nm distance. Åberg et al. employed a value of 45 nm for the distance between the bilayers [53]. Since the zero of the free energy was chosen to lie within bulk water, the local permeation resistance of water, Eq. (4.11), simply becomes a constant $R^p = 1/D_z$. The permeability is obtained by multiplying this value by the thickness of the water slab h and by taking the inverse value of this as $\mathcal{P} = D_z/h$. However, instead of permeabilities it is more intuitive to compare permeation resistances as they are additive. The diffusion coefficient of water in our simulations was found to be about $3.5 \times 10^{-5} \text{ cm}^2/\text{s}$. Then passing through a water layer with a thickness

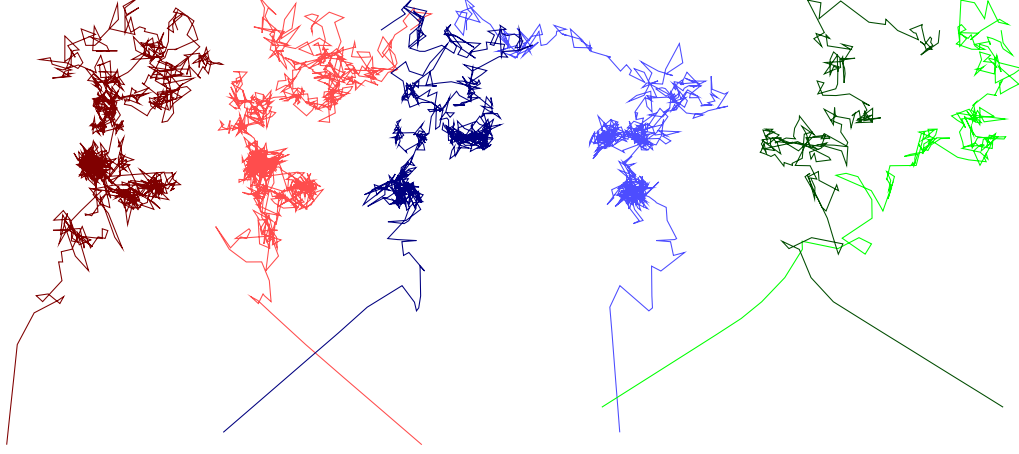


Figure 6.17: Trajectories of oxygen molecules permeating freely through monolayer systems. The mean molecular areas represented are $\langle A \rangle = 48 \text{ \AA}^2$ (— and —), 56 \AA^2 (— and —) and 64 \AA^2 (— and —). Darker and lighter colours show the motion of the same oxygen molecule in the (x, z) and (y, z) directions in the respective system.

of 45 nm gives $\mathcal{R}_{\text{water}} = 0.13 \text{ s/cm}$ as the total resistance of the water layer. Now the mean local permeation resistance averaged over the system of alternating water layers and bilayers is $\mathcal{R}_{\text{average}} = 4.9 \times 10^4 \text{ s/cm}^2$.

In the case of the CLP structure the oxygen molecule travels through the membrane interior. The calculated average diffusion coefficient in the membrane plane in region 4 is $2.4 \times 10^{-5} \text{ cm}^2/\text{s}$. The average free energy difference between region 4 and the water phase is -5.2 kJ/mol . Now the mean local resistance is again constant and has a value of $5.5 \times 10^3 \text{ s/cm}^2$. This value is approximately one order of magnitude smaller than the one obtained for the aligned bilayers, clearly supporting the view of oxygen permeating lung surfactant structures through the bilayer cores if such structures are available in the real lung. Following the ideas of Åberg et al., we can also calculate the weighted average of the resistances of stacked bilayers and bilayer cores in the CLP model and the resulting resistance is $4.4 \times 10^4 \text{ s/cm}^2$. Thus by introducing the bilayer channels at the intervals of 45 nm to the system of stacked bilayers, the resistance for oxygen is reduced by about 10%.

It is also possible that the pathway for oxygen is the one suggested by Olmeda et al. [54] and depicted on the right of Fig. 2.5, since as long as the distance the oxygen has to travel is not more than 10 times longer than the shortest path in the stacked bilayer model, permeation is still faster through the cores of the bilayers. It is also possible that these bilayers directly connect to the surfactant monolayer and that oxygen actually never has to pass through the monolayer. If lung surfactant remains in the state of very low tension even during inhaling, the permeation resistance of the surfactant monolayer is always substantially high. Hence, a pathway that would

not include permeation through the monolayer would be very favourable.

To conclude, oxygen is likely to pass the membrane structures through the bilayer cores, namely through the tubular myelin structure if such structures are available in the lung. The explanation to why proteins enhance oxygen permeation rates might be that the structure of tubular myelin is not that presented in Fig. 2.5 but rather one in which the bilayers do not cross each other and permeation occurs through channels induced by surfactant protein B as suggested by Pérez-Gil [56]. Another option is that proteins are not vital structural components in tubular myelin but they are needed in the formation process of the structure.

7. CONCLUDING REMARKS

The aim of this Thesis project was to study oxygen permeation through biological membranes employing the computational molecular dynamics method. The first goal was to develop an atomistic model for molecular oxygen, with an objective to optimize its validity at the interface between aqueous and membrane phases. This model was further employed in studying the permeation of lung surfactant structures.

The optimal parameter set obtained for the oxygen molecule reproduced well the behaviour of real oxygen in terms of the considered physical quantities. While the calculated density at boiling point and heat of vaporisation were both surprisingly close to their experimental counterparts [170], the correct value for partitioning between water and hexadecane could not be exactly obtained. Discrepancy between simulated and experimental values might, however, be due to differences in solute concentration. All in all, our model performed exceptionally well and better than the models employed in earlier computational studies on the topic of oxygen permeation [8, 137].

The excess free energy and diffusion coefficient profiles of the monolayers and the bilayer were calculated from the data obtained from the constraint pulling method. The key values of all free energy profiles matched well the values determined experimentally and computationally in other studies. The free energy of transfer for going from bulk water phase to the bilayer core was found to be about -7 kJ/mol with a barrier in the head group region of approximately 4 kJ/mol.

The excess free energy profiles for the monolayer followed the same guidelines. The profiles for systems with a different mean molecular area were fairly similar, and the average free energy of transfer between water and gas phase was calculated to be about 9.7 kJ/mol. The validity of the simulations was ensured in the case of the bilayer with a more commonly employed umbrella sampling method, which provided results very similar to those obtained from the z constraint method. Effort was also put into calculating the entropic and enthalpic contributions to oxygen partitioning into lipid systems, yet the results for mono- and bilayers were not in line together. Thus no conclusions can be drawn on the existence of the so-called bilayer effect in the case of oxygen.

Local diffusion coefficient profiles were calculated for the monolayers and the bilayer. The key values that can be compared to experiments, namely diffusion in

membrane core resembling hexadecane and diffusion in bulk water, were very close to values obtained in other studies. The values between these two extremities, however, were drastically smaller than expected and diffusion was also greatly hindered when the monolayer was compressed. The methodology through which diffusion coefficients were obtained was also verified with calculations on the lateral diffusion coefficients at different depths in the membrane and these values turned out to be almost identical to the ones obtained from force autocorrelation, indicating that oxygen diffusion in our systems is highly isotropic.

The resistance profiles displayed large peaks in the head group region in all studied cases due to slow diffusion and a fairly high free energy barrier in this region. The permeability of the bilayer for oxygen was calculated to be 8.7 cm/s whereas the values for the monolayer systems were in the range from 5.2 cm/s to 34.4 cm/s when moving from water phase towards vacuum, and 0.12 cm/s to 0.81 cm/s in the other direction. The experimental values for bilayer systems are somewhat larger, yet possible factors for these discrepancies include the perturbation induced by the experimental methods and the limited resolution of the experiments especially in the head group region in which the highest resistance peak lies. If the high-resistance head group regions are discarded in our calculations, the obtained values are of the same order of magnitude as the experimental ones.

Experimental studies on monolayers have come up with drastically different values for oxygen permeation compared to those obtained for bilayers [6, 7, 105]. The values are often measured from the air phase towards the aqueous phase, thus to the higher free energy state in the case of oxygen. In this case our values are slightly larger than the experimental ones, which might be due to the inability of a united atom force field to reproduce the correct microviscosity. However, our results further support the idea that monolayers, especially in the low tension state, are permeation barriers for oxygen and the permeability through them is drastically slower than that through bulk water.

Theories on how permeability is connected with other physical quantities could be examined with the aid of permeability data on monolayers with a range of mean molecular areas. Many of these dependencies could be verified. Permeability seems to be inversely proportional to monolayer thickness, which in the case of constant lipid composition results in the linear dependence between permeability and mean area per molecule. It was also found that the relation between permeability and monolayer thickness could also be exponential as is the case with permeability and surface tension.

The effect on oxygen transport imposed by the lung surfactant structures residing in its close vicinity were also evaluated based on our results. It was found that if bilayer complexes exist below the surfactant monolayer in one form or another, they

could positively affect the permeation of oxygen through the membrane system in addition to their positive structural importance. Within these structures, oxygen permeation could be enhanced if the molecules travelled along the bilayer cores as suggested very recently [53, 54]. The total permeation resistance observed by oxygen along this pathway is drastically smaller than in the case of oxygen, having to permeate successive water layers. The calculated oxygen permeation was slow through the tightly-packed monolayers, supporting a model according to which oxygen might pass to bilayer structures folded out from the monolayer plane and thus not needing to permeate the dense monolayer at all.

The problem of oxygen permeation through lung surfactant structures was thoroughly studied. Improvements over earlier studies were made in the form of more accurate models and longer simulation times. The employed conditions mimicked that of the real lung and the effect of monolayer state was considered by employing a range of monolayers at different compression levels. High resolution profiles calculated here are able to provide information far beneath the level of detail of experimental studies. The results provide answers to many open questions that are currently impossible to study experimentally, yet they also leave some questions unanswered. One of these is whether partitioning of hydrophobic particles into biological membranes is driven by enthalpic or entropic force. It is hard to see how the topic could be further investigated through molecular dynamics as the length and time scaled employed in this study are already adequate. Improvements on the model are always possible, yet quantum-mechanical models might be required as the limitations of classical potential descriptions might already be reached in this study. The recent results on oxygen permeation through other lung surfactant structures, such as the CLP model and other possibilities, however, pose an ideal target for further molecular dynamics simulations on this topic.

BIBLIOGRAPHY

- [1] **J.B. West.** *Respiratory physiology: the essentials*. Lippincott Williams & Wilkins, Baltimore, 2008.
- [2] **J. Goerke.** Pulmonary surfactant: functions and molecular composition. *Biochimica et Biophysica Acta (BBA)-Molecular Basis of Disease*, 1408:79–89, 1998.
- [3] **Y.Y. Zuo, E. Acosta, P.N. Cox, D. Li, and A.W. Neumann.** Effect of compressed bovine lipid extract surfactant films on oxygen transfer. *Langmuir*, 23:1339–1346, 2007.
- [4] **E. Ladanyi, RC Ahuja, D. Möbius, and K. Stalder.** Oxygen transport through a model lung surfactant surface layer: influence of the film compression on the kinetics. *Advances in Experimental Medicine and Biology*, 317:343, 1992.
- [5] **W.K. Subczynski, J.S. Hyde, and A. Kusumi.** Oxygen permeability of phosphatidylcholine–cholesterol membranes. *Proceedings of the National Academy of Sciences of the United States of America*, 86:4474, 1989.
- [6] **I.I. Ivanov, G.E. Fedorov, R.A. Gus’kova, K.I. Ivanov, and A.B. Rubin.** Permeability of lipid membranes to dioxygen. *Biochemical and Biophysical Research Communications*, 322:746–750, 2004.
- [7] **M.A. Borden and M.L. Longo.** Oxygen permeability of fully condensed lipid monolayers. *The Journal of Physical Chemistry B*, 108:6009–6016, 2004.
- [8] **S.J. Marrink and H.J.C. Berendsen.** Permeation process of small molecules across lipid membranes studied by molecular dynamics simulations. *The Journal of Physical Chemistry*, 100:16729–16738, 1996.
- [9] **S.J. McKinnon, S.L. Whittenburg, and B. Brooks.** Nonequilibrium molecular dynamics simulation of oxygen diffusion through hexadecane monolayers with varying concentrations of cholesterol. *The Journal of Physical Chemistry*, 96:10497–10506, 1992.
- [10] **M.S. Al-Abdul-Wahid, C.H. Yu, I. Batruch, F. Evanics, R. Pomès, and R.S. Prosser.** A combined NMR and molecular dynamics study of the transmembrane solubility and diffusion rate profile of dioxygen in lipid bilayers. *Biochemistry*, 45:10719–10728, 2006.
- [11] **J.M. Diamond and Y. Katz.** Interpretation of nonelectrolyte partition coefficients between dimyristoyl lecithin and water. *The Journal of Membrane Biology*, 17:121–154, 1974.
- [12] **S.J. Marrink and H.J.C. Berendsen.** Simulation of water transport through a lipid membrane. *The Journal of Physical Chemistry*, 98:4155–4168, 1994.
- [13] **R. Rhoades and D.R. Bell.** *Medical physiology: principles for clinical medicine*. Lippincott Williams & Wilkins, Baltimore, 2009.
- [14] **M. Ochs, J.R. Nyengaard, A. Jung, L. Knudsen, M. Voigt, T. Wahlers, J. Richter, and H.J.G. Gundersen.** The number of alveoli in the human lung. *American Journal of Respiratory and Critical Care Medicine*, pages 120–124, 2003.

- [15] **C.B. Daniels and S. Orgeig.** Pulmonary surfactant: the key to the evolution of air breathing. *Physiology*, 18:151–157, 2003.
- [16] **E.R. Weibel.** Morphometry of the human lung. *Anesthesiology*, 26:367, 1965.
- [17] **S.A. Hafez, T. Caceci, L.E. Freeman, and K.E. Panter.** Angiogenesis in the Caprine caruncles in non-pregnant and pregnant normal and swainsonine-treated does. *The Anatomical Record: Advances in Integrative Anatomy and Evolutionary Biology*, 290, 2007.
- [18] **P.H. Raven and G.B. Johnson.** *Biology 6th ed.* McGraw-Hill Publishing, New York, 2002.
- [19] **G.E. Nilsson.** *Respiratory physiology of vertebrates: life with and without oxygen.* Cambridge University Press, Cambridge, 2010.
- [20] **M. Longmore, I.B. Wilkinson, and S.R. Rajagopalan.** *Oxford handbook of clinical medicine.* Oxford University Press, USA, New York, 2004.
- [21] **J.E. Cotes and G.L. Leathart.** *Lung function.* Blackwell Scientific, Oxford, 1968.
- [22] **B.D. Butler and B.A. Hills.** The lung as a filter for microbubbles. *Journal of Applied Physiology*, 47:537, 1979.
- [23] **S.M. Travis, B.A. Conway, J. Zabner, J.J. Smith, N.N. Anderson, P.K. Singh, E.P. Greenberg, and M.J. Welsh.** Activity of abundant antimicrobials of the human airway. *American Journal of Respiratory Cell and Molecular Biology*, 20:872, 1999.
- [24] **O. Sand, Ø.V. Sjaastad, and E. Haug.** *Menneskets fysiologi.* Gyldendal Akademisk., Oslo, 2001.
- [25] **M.H. Ross, E.J. Reith, L.J. Romrell, and L.V. Kibiuk.** *Histology: a text and atlas.* Williams & Wilkins, Baltimore, 1989.
- [26] **P.J. Lynch and C.C. Jaffe.** Personal site of artist and author Pat Lynch. <http://patricklynch.net/>, December 2006. Cited June 9. 2009.
- [27] **Y.Y. Zuo, R.A.W. Veldhuizen, A.W. Neumann, N.O. Petersen, and F. Possmayer.** Current perspectives in pulmonary surfactant–inhibition, enhancement and evaluation. *Biochimica et Biophysica Acta (BBA)-Biomembranes*, 1778:1947–1977, 2008.
- [28] **R.D. Hubmayr.** Perspective on lung injury and recruitment. *American Journal of Respiratory and Critical Care Medicine*, 165:1647–1653, 2002.
- [29] **A. Keith.** The mechanism of respiration in man. *Further advances in physiology*, pages 182–207, 1909.
- [30] **J.B. Forrest.** The effect of changes in lung volume on the size and shape of alveoli. *The Journal of Physiology*, 210:533, 1970.
- [31] **S. Krol, M. Ross, M. Sieber, S. Künneke, H.J. Galla, and A. Janshoff.** Formation of three-dimensional protein-lipid aggregates in monolayer films induced by surfactant protein B. *Biophysical Journal*, 79:904–918, 2000.

- [32] **S. Baoukina, L. Monticelli, M. Amrein, and D.P. Tieleman.** The molecular mechanism of monolayer-bilayer transformations of lung surfactant from molecular dynamics simulations. *Biophysical Journal*, 93:3775–3782, 2007.
- [33] **S. Baoukina, L. Monticelli, H.J. Risselada, S.J. Marrink, and D.P. Tieleman.** The molecular mechanism of lipid monolayer collapse. *Proceedings of the National Academy of Sciences*, 105:10803, 2008.
- [34] **D. Kashchiev and D. Exerowa.** Structure and surface energy of the surfactant layer on the alveolar surface. *European Biophysics Journal*, 30:34–41, 2001.
- [35] **S. Baoukina and D.P. Tieleman.** Lung surfactant protein SP-B promotes formation of bilayer reservoirs from monolayer and lipid transfer between the interface and subphase. *Biophysical Journal*, 100:1678–1687, 2011.
- [36] **H.J. Galla, N. Bourdos, A. Von Nahmen, M. Amrein, and M. Sieber.** The role of pulmonary surfactant protein C during the breathing cycle. *Thin Solid Films*, 327:632–635, 1998.
- [37] **S. Malcharek, A. Hinz, L. Hilterhaus, and H.J. Galla.** Multilayer structures in lipid monolayer films containing surfactant protein C: effects of cholesterol and POPE. *Biophysical Journal*, 88:2638–2649, 2005.
- [38] **H. Bachofen and S. Schürch.** Alveolar surface forces and lung architecture. *Comparative Biochemistry and Physiology-Part A: Molecular & Integrative Physiology*, 129:183–193, 2001.
- [39] **J.M. Halter, J.M. Steinberg, H.J. Schiller, M. DaSilva, L.A. Gatto, S. Landas, and G.F. Nieman.** Positive end-expiratory pressure after a recruitment maneuver prevents both alveolar collapse and recruitment/derecruitment. *American Journal of Respiratory and Critical Care Medicine*, 167:1620–1626, 2003.
- [40] **E. Namati, J. Thiesse, J. De Ryk, and G. McLennan.** Alveolar dynamics during respiration: are the pores of Kohn a pathway to recruitment? *American Journal of Respiratory Cell and Molecular Biology*, 38:572, 2008.
- [41] **L. Sherwood.** *Human physiology: from cells to systems*. Brooks/Cole, Belmont, 2008.
- [42] **J.R. Wright.** Pulmonary surfactant: a front line of lung host defense. *The Journal of Clinical Investigation*, 111:1453–1455, 2003.
- [43] **I. Frerking, A. Günther, W. Seeger, and U. Pison.** Pulmonary surfactant: functions, abnormalities and therapeutic options. *Intensive Care Medicine*, 27:1699–1717, 2001.
- [44] **U. Pison, R. Herold, and S. Schürch.** The pulmonary surfactant system: biological functions, components, physicochemical properties and alterations during lung disease. *Colloids and Surfaces A: Physicochemical and Engineering Aspects*, 114:165–184, 1996.
- [45] **T. Akino.** Lipid components of the surfactant system. *Pulmonary Surfactant: from molecular biology to clinical practice*. Eds. LMG van Golde and JJ Batenburg, Elsevier Science Publishers, New York NY, pages 19–31, 1992.

- [46] **R. Veldhuizen, K. Nag, S. Orgeig, and F. Possmayer.** The role of lipids in pulmonary surfactant. *Biochimica et Biophysica Acta (BBA)-Molecular Basis of Disease*, 1408:90–108, 1998.
- [47] **G.S. Pryhuber.** Regulation and function of pulmonary surfactant protein B. *Molecular Genetics and Metabolism*, 64:217–228, 1998.
- [48] **S. Hawgood, B.J. Benson, J. Schilling, D. Damm, J.A. Clements, and R.T. White.** Nucleotide and amino acid sequences of pulmonary surfactant protein SP 18 and evidence for cooperation between SP 18 and SP 28-36 in surfactant lipid adsorption. *Proceedings of the National Academy of Sciences of the United States of America*, 84:66, 1987.
- [49] **A.M. LeVine and J.A. Whitsett.** Pulmonary collectins and innate host defense of the lung. *Microbes and Infection*, 3:161–166, 2001.
- [50] **Y. Kikkawa, K. Yoneda, F. Smith, B. Packard, and K. Suzuki.** The type II epithelial cells of the lung. II. Chemical composition and phospholipid synthesis. *Laboratory Investigation; a Journal of Technical Methods and Pathology*, 32:295, 1975.
- [51] **M.C. Williams.** Conversion of lamellar body membranes into tubular myelin in alveoli of fetal rat lungs. *The Journal of Cell Biology*, 72:260, 1977.
- [52] **S. Hawgood and J.A. Clements.** Pulmonary surfactant and its apoproteins. *The Journal of Clinical Investigation*, 86:1, 1990.
- [53] **C. Åberg, E. Sparr, M. Larsson, and H. Wennerström.** A theoretical study of diffusional transport over the alveolar surfactant layer. *The Journal of The Royal Society Interface*, 7:1403–1410, 2010.
- [54] **B. Olmeda, L. Villén, A. Cruz, G. Orellana, and J. Perez-Gil.** Pulmonary surfactant layers accelerate O_2 diffusion through the air-water interface. *Biochimica et Biophysica Acta (BBA)-Biomembranes*, 1798:1281–1284, 2010.
- [55] **M. Larsson, K. Larsson, S. Andersson, J. Kakhar, T. Nylander, B. Ninham, and P. Wollmer.** The alveolar surface structure: transformation from a liposome-like dispersion into a tetragonal clp bilayer phase. *Journal of Dispersion Science and Technology*, 20:1–12, 1999.
- [56] **J. Pérez-Gil.** Structure of pulmonary surfactant membranes and films: the role of proteins and lipid-protein interactions. *Biochimica et Biophysica Acta (BBA)-Biomembranes*, 1778:1676–1695, 2008.
- [57] **M.K. Campbell and S.O. Farrell.** *Biochemistry*. Thomson Brooks/Cole, Pacific Grove, 2003.
- [58] **M.I. Gurr, J.L. Harwood, K.N. Frayn, and Inc ebrary.** *Lipid biochemistry*. Blackwell Science, Oxford, 2002.
- [59] **P.R. Cullis, C.P. Tilcock, and M.J. Hope.** Lipid polymorphism. *Membrane Fusion (Wilschut, J. and Hoekstra, D., eds.)*, pages 35–64, 1991.
- [60] **O.G. Mouritsen.** *Life-as a matter of fat*. Springer-Verlag, Berlin, 2005.

- [61] **P. Nelson, M. Radosavljevic, and S. Bromberg.** *Biological physics*. Freeman, New York, 2004.
- [62] **W.R. Nes.** Role of sterols in membranes. *Lipids*, 9:596–612, 1974.
- [63] **K. Lindsey, M.L. Pullen, and J.F. Topping.** Importance of plant sterols in pattern formation and hormone signalling. *Trends in Plant Science*, 8:521–525, 2003.
- [64] **J.A. Porter, K.E. Young, and P.A. Beachy.** Cholesterol modification of hedgehog signaling proteins in animal development. *Science*, 274:255, 1996.
- [65] **J.T. Moore and R. Langley.** *Biochemistry for dummies*. Wiley, Indianapolis, 2008.
- [66] **G. Daum.** Lipids of mitochondria. *Biochimica et Biophysica Acta (BBA)-Reviews on Biomembranes*, 822:1–42, 1985.
- [67] **W. Zhao, T. Róg, A.A. Gurtovenko, I. Vattulainen, and M. Karttunen.** Atomic-scale structure and electrostatics of anionic palmitoylphosphatidylglycerol lipid bilayers with Na^+ counterions. *Biophysical Journal*, 92:1114–1124, 2007.
- [68] **G.E. Hook, J.W. Spalding, M.J. Ortner, E.G. Tombropoulos, and C.F. Chignell.** Investigation of phospholipids of the pulmonary extracellular lining by electron paramagnetic resonance. The effects of phosphatidylglycerol and unsaturated phosphatidylcholines on the fluidity of dipalmitoyl phosphatidylcholine. *Biochemical Journal*, 223:533, 1984.
- [69] **B. Alberts.** *Molecular biology of the cell*. Routledge, New York, 1989.
- [70] **E. Falck, M. Patra, M. Karttunen, M.T. Hyvönen, and I. Vattulainen.** Lessons of slicing membranes: interplay of packing, free area, and lateral diffusion in phospholipid/cholesterol bilayers. *Biophysical Journal*, 87:1076–1091, 2004.
- [71] **A.D. McNaught, A. Wilkinson, International Union of Pure, and Applied Chemistry.** *Compendium of chemical terminology: IUPAC recommendations*. Blackwell Science, Oxford, 1997.
- [72] **R.P. Schwarzenbach, P.M. Gschwend, and D.M. Imboden.** *Environmental organic chemistry*. Wiley-Interscience, New York, 2003.
- [73] **S.A. Best, K.M. Merz Jr, and C.H. Reynolds.** Free energy perturbation study of octanol/water partition coefficients: Comparison with continuum GB/SA calculations. *The Journal of Physical Chemistry B*, 103:714–726, 1999.
- [74] **J.E. Eksterowicz, J.L. Miller, and P.A. Kollman.** Calculation of chloroform/water partition coefficients for the n-methylated nucleic acid bases. *The Journal of Physical Chemistry B*, 101:10971–10975, 1997.
- [75] **D. Frenkel and B. Smit.** *Understanding molecular simulation*. Academic Press, Orlando, 2001.
- [76] **J.P. Hansen and I.R. McDonald.** *Theory of simple liquids*. Academic Press, London, 2006.

- [77] **S. Boresch, G. Archontis, and M. Karplus.** Free energy simulations: the meaning of the individual contributions from a component analysis. *Proteins: Structure, Function, and Bioinformatics*, 20:25–33, 1994.
- [78] **B. Hess, C. Kutzner, D. van der Spoel, and E. Lindahl.** GROMACS 4: Algorithms for highly efficient, load-balanced, and scalable molecular simulation. *The Journal of Chemical Theory and Computation*, 4:435–447, 2008.
- [79] **D. Van Der Spoel, E. Lindahl, B. Hess, G. Groenhof, A.E. Mark, and H.J.C. Berendsen.** GROMACS: fast, flexible, and free. *The Journal of Computational Chemistry*, 26:1701–1718, 2005.
- [80] **V.C. Scanlon and T. Sanders.** *Essentials of anatomy and physiology*. FA Davis, Philadelphia, 1991.
- [81] **T. Hanai and D.A. Haydon.** The permeability to water of bimolecular lipid membranes. *The Journal of Theoretical Biology*, 11:370–382, 1966.
- [82] **W.D. Stein and W.R. Lieb.** *Transport and diffusion across cell membranes*. Academic Press, New York, 1986.
- [83] **D. Bemporad, C. Luttmann, and J.W. Essex.** Computer simulation of small molecule permeation across a lipid bilayer: dependence on bilayer properties and solute volume, size, and cross-sectional area. *Biophysical Journal*, 87:1–13, 2004.
- [84] **A. Walter and J. Gutknecht.** Permeability of small nonelectrolytes through lipid bilayer membranes. *The Journal of Membrane Biology*, 90:207–217, 1986.
- [85] **T.X. Xiang and B.D. Anderson.** The relationship between permeant size and permeability in lipid bilayer membranes. *The Journal of Membrane Biology*, 140:111–122, 1994.
- [86] **J.C. Mathai, S. Tristram-Nagle, J.F. Nagle, and M.L. Zeidel.** Structural determinants of water permeability through the lipid membrane. *The Journal of General Physiology*, 131:69, 2008.
- [87] **A. Carruthers and D.L. Melchior.** Study of the relationship between bilayer water permeability and bilayer physical state. *Biochemistry*, 22:5797–5807, 1983.
- [88] **N.D. Winter and G.C. Schatz.** Coarse-grained molecular dynamics study of permeability enhancement in DPPC bilayers by incorporation of lysolipid. *The Journal of Physical Chemistry B*, 114:5053–5060, 2010.
- [89] **A. Finkelstein.** Effect of cholesterol on the water permeability of thin lipid membranes. *Nature*, 216:717–718, 1967.
- [90] **D. Papahadjopoulos, S. Nir, and S. Ohki.** Permeability properties of phospholipid membranes: effect of cholesterol and temperature. *Biochimica et Biophysica Acta (BBA)-Biomembranes*, 266:561–583, 1972.
- [91] **S. Paula, A.G. Volkov, A.N. Van Hoek, T.H. Haines, and D.W. Deamer.** Permeation of protons, potassium ions, and small polar molecules through phospholipid bilayers as a function of membrane thickness. *Biophysical Journal*, 70:339–348, 1996.

- [92] **T. Sugii, S. Takagi, and Y. Matsumoto.** A molecular-dynamics study of lipid bilayers: effects of the hydrocarbon chain length on permeability. *The Journal of Chemical Physics*, 123:184714, 2005.
- [93] **G. Pu, M.L. Longo, and M.A. Borden.** Effect of microstructure on molecular oxygen permeation through condensed phospholipid monolayers. *The Journal of the American Chemical Society*, 127:6524–6525, 2005.
- [94] **R.J. Archer and V.K.L. Mer.** The rate of evaporation of water through fatty acid monolayers. *The Journal of Physical Chemistry*, 59:200–208, 1955.
- [95] **I. Langmuir and V.J. Schaefer.** Rates of evaporation of water through compressed monolayers on water. *The Journal of the Franklin Institute*, 235:119–162, 1943.
- [96] **I. Ciani, D.P. Burt, S. Daniele, and P.R. Unwin.** Effect of surface pressure on oxygen transfer across molecular monolayers at the air/water interface: scanning electrochemical microscopy investigations using a mercury hemispherical microelectrode probe. *The Journal of Physical Chemistry B*, 108:3801–3809, 2004.
- [97] **M.S. Al-Abdul-Wahid, F. Evanics, and R.S. Prosser.** Dioxygen Transmembrane Distributions and Partitioning Thermodynamics in Lipid Bilayers and Micelles. *Biochemistry*, 50:3975–3983, 2011.
- [98] **W. Shinoda, M. Mikami, T. Baba, and M. Hato.** Molecular dynamics study on the effects of chain branching on the physical properties of lipid bilayers: 2. Permeability. *The Journal of Physical Chemistry B*, 108:9346–9356, 2004.
- [99] **D. Bemporad, J.W. Essex, and C. Luttmann.** Permeation of small molecules through a lipid bilayer: a computer simulation study. *The Journal of Physical Chemistry B*, 108:4875–4884, 2004.
- [100] **Y. Rharbi, A. Yekta, and M.A. Winnik.** A method for measuring oxygen diffusion and oxygen permeation in polymer films based on fluorescence quenching. *Analytical Chemistry*, 71:5045–5053, 1999.
- [101] **G. Schappacher and P. Hartmann.** Partial analytical solution of a model used for measuring oxygen diffusion coefficients of polymer films by luminescence quenching. *Analytical Chemistry*, 75:4319–4324, 2003.
- [102] **I.I. Ivanov, A.V. Loktyushkin, R.A. Gus' kova, N.S Vasil'ev, G.E. Fedorov, and A.B. Rubin.** Oxygen channels of erythrocyte membrane. In *Doklady Biochemistry and Biophysics*, volume 414, pages 137–140. Springer, 2007.
- [103] **D. Marsh, B.G. Dzikovski, and V.A. Livshits.** Oxygen profiles in membranes. *Biophysical Journal*, 90:L49–L51, 2006.
- [104] **R.D. Nielsen, K. Che, M.H. Gelb, and B.H. Robinson.** A ruler for determining the position of proteins in membranes. *The Journal of the American Chemical Society*, 127:6430–6442, 2005.

- [105] **J. Strutwolf, J. Zhang, A.L. Barker, and P.R. Unwin.** Effect of phospholipids on the kinetics of dioxygen transfer across a 1, 2-dichloroethane/water interface. *Physical Chemistry Chemical Physics*, 3:5553–5558, 2001.
- [106] **T. Graham.** LV. On the absorption and dialytic separation of gases by colloid septa. *Philosophical Magazine Series 4*, 32:401–420, 1866.
- [107] **H. Träuble.** The movement of molecules across lipid membranes: a molecular theory. *The Journal of Membrane Biology*, 4:193–208, 1971.
- [108] **E. Orbach and A. Finkelstein.** The nonelectrolyte permeability of planar lipid bilayer membranes. *The Journal of General Physiology*, 75:427, 1980.
- [109] **A. Finkelstein.** Water and nonelectrolyte permeability of lipid bilayer membranes. *The Journal of General Physiology*, 68:127, 1976.
- [110] **D.W. Deamer, A. Kleinzeller, and D.M. Fambrough.** *Membrane permeability: 100 years since Ernest Overton*. Academic Press, San Diego, 1999.
- [111] **E. Overton.** About the general osmotic properties of the cell, their presumable causes, and their importance for physiology. *Vierteljahrsschrift der Naturforschenden Gesellschaft in Zürich*, 44:88–135, 1899.
- [112] **H. Meyer.** Zur theorie der alkoholnarkose. *Naunyn-Schmiedeberg's Archives of Pharmacology*, 42:109–118, 1899.
- [113] **G. Zaccai, J.K. Blasie, and B.P. Schoenborn.** Neutron diffraction studies on the location of water in lecithin bilayer model membranes. *Proceedings of the National Academy of Sciences of the United States of America*, 72:376, 1975.
- [114] **M.C. Wiener and S.H. White.** Structure of a fluid dioleoylphosphatidylcholine bilayer determined by joint refinement of x-ray and neutron diffraction data. III. Complete structure. *Biophysical Journal*, 61:434–447, 1992.
- [115] **Y.K. Levine and M.H.F. Wilkins.** Structure of oriented lipid bilayers. *Nature*, 230:69–72, 1971.
- [116] **E.S.E. Eriksson and L.A. Eriksson.** The influence of cholesterol on the properties and permeability of hypericin derivatives in lipid membranes. *The Journal of Chemical Theory and Computation*, 7:560–574, 2011.
- [117] **R.H. Guy and D.H. Honda.** Solute transport resistance at the octanol-water interface. *International Journal of Pharmaceutics*, 19:129–137, 1984.
- [118] **L.R. De Young and K.A. Dill.** Solute partitioning into lipid bilayer membranes. *Biochemistry*, 27:5281–5289, 1988.
- [119] **L.R. De Young and K.A. Dill.** Partitioning of nonpolar solutes into bilayers and amorphous n-alkanes. *The Journal of Physical Chemistry*, 94:801–809, 1990.
- [120] **M. Orsi, W.E. Sanderson, and J.W. Essex.** Permeability of small molecules through a lipid bilayer: a multiscale simulation study. *The Journal of Physical Chemistry B*, 113:12019–12029, 2009.

- [121] **J.M. Diamond, G. Szabo, and Y. Katz.** Theory of nonelectrolyte permeation in a generalized membrane. *The Journal of Membrane Biology*, 17:148–152, 1974.
- [122] **J.L. MacCallum and D.P. Tieleman.** Computer simulation of the distribution of hexane in a lipid bilayer: spatially resolved free energy, entropy, and enthalpy profiles. *The Journal of the American Chemical Society*, 128:125–130, 2006.
- [123] **S. Mitragotri, M.E. Johnson, D. Blankschtein, and R. Langer.** An analysis of the size selectivity of solute partitioning, diffusion, and permeation across lipid bilayers. *Biophysical Journal*, 77:1268–1283, 1999.
- [124] **J.F. Nagle, J.C. Mathai, M.L. Zeidel, and S. Tristram-Nagle.** Theory of passive permeability through lipid bilayers. *The Journal of General Physiology*, 131:77, 2008.
- [125] **S.J. Marrink, R.M. Sok, and H.J.C. Berendsen.** Free volume properties of a simulated lipid membrane. *The Journal of Chemical Physics*, 104:9090–9099, 1996.
- [126] **J.L. MacCallum, WF Bennett, and D.P. Tieleman.** Distribution of amino acids in a lipid bilayer from computer simulations. *Biophysical Journal*, 94:3393–3404, 2008.
- [127] **D. Bemporad, C. Luttmann, and J.W. Essex.** Behaviour of small solutes and large drugs in a lipid bilayer from computer simulations. *Biochimica et Biophysica Acta (BBA)-Biomembranes*, 1718:1–21, 2005.
- [128] **V.S. Markin and M.M. Kozlov.** Pore statistics in bilayer lipid membranes. *Biologicheskije Membrany*, 2:205–223, 1985.
- [129] **R.T. Hamilton and E.W. Kaler.** Alkali metal ion transport through thin bilayers. *The Journal of Physical Chemistry*, 94:2560–2566, 1990.
- [130] **G.M. Torrie and J.P. Valleau.** Nonphysical sampling distributions in Monte Carlo free-energy estimation: umbrella sampling. *Journal of Computational Physics*, 23:187–199, 1977.
- [131] **B. Widom.** Some topics in the theory of fluids. *The Journal of Chemical Physics*, 39:2808, 1963.
- [132] **R. Kubo.** The fluctuation-dissipation theorem. *Reports on Progress in Physics*, 29:255, 1966.
- [133] **J. Wong-Ekkabut, Z. Xu, W. Triampo, I. Tang, et al.** Effect of lipid peroxidation on the properties of lipid bilayers: a molecular dynamics study. *Biophysical Journal*, 93:4225–4236, 2007.
- [134] **P.V.K. Pant and R.H. Boyd.** Molecular-dynamics simulation of diffusion of small penetrants in polymers. *Macromolecules*, 26:679–686, 1993.
- [135] **D. Bassolino-Klimas, H.E. Alper, and T.R. Stouch.** Solute diffusion in lipid bilayer membranes: an atomic level study by molecular dynamics simulation. *Biochemistry*, 32:12624–12637, 1993.
- [136] **D. Bassolino-Klimas, H.E. Alper, and T.R. Stouch.** Mechanism of solute diffusion through lipid bilayer membranes by molecular dynamics simulation. *The Journal of the American Chemical Society*, 117:4118–4129, 1995.

- [137] **J.S. Hub and B.L. de Groot.** Mechanism of selectivity in aquaporins and aquaglyceroporins. *Proceedings of the National Academy of Sciences of the United States of America*, 105:1198, 2008.
- [138] **A. Ligeza, A.N. Tikhonov, J.S. Hyde, and W.K. Subczynski.** Oxygen permeability of thylakoid membranes: electron paramagnetic resonance spin labeling study. *Biochimica et Biophysica Acta (BBA)-Bioenergetics*, 1365:453–463, 1998.
- [139] **W.K. Subczynski, L.E. Hopwood, and J.S. Hyde.** Is the mammalian cell plasma membrane a barrier to oxygen transport? *The Journal of General Physiology*, 100:69, 1992.
- [140] **S. Fischkoff and J.M. Vanderkooi.** Oxygen diffusion in biological and artificial membranes determined by the fluorochrome pyrene. *The Journal of General Physiology*, 65:663, 1975.
- [141] **K. Kawasaki, J.J. Yin, W.K. Subczynski, J.S. Hyde, and A. Kusumi.** Pulse EPR detection of lipid exchange between protein-rich raft and bulk domains in the membrane: methodology development and its application to studies of influenza viral membrane. *Biophysical Journal*, 80:738–748, 2001.
- [142] **I. Ashikawa, J.J. Yin, W.K. Subczynski, T. Kouyama, J.S. Hyde, and A. Kusumi.** Molecular organization and dynamics in bacteriorhodopsin-rich reconstituted membranes: discrimination of lipid environments by the oxygen transport parameter using a pulse ESR spin-labeling technique. *Biochemistry*, 33:4947–4952, 1994.
- [143] **B.A. Kowert and N.C. Dang.** Diffusion of Dioxygen in n-Alkanes. *The Journal of Physical Chemistry A*, 103:779–781, 1999.
- [144] **B.A. Kowert, N.C. Dang, J.P. Reed, K.T. Sobush, and G. Louis III.** Diffusion of Dioxygen in Alkanes and Cycloalkanes. *The Journal of Physical Chemistry A*, 104:8823–8828, 2000.
- [145] **D.R. DeVido, J.G. Dorsey, H.S. Chan, and K.A. Dill.** Oil/water partitioning has a different thermodynamic signature when the oil solvent chains are aligned than when they are amorphous. *The Journal of Physical Chemistry B*, 102:7272–7279, 1998.
- [146] **W.C. Wimley and S.H. White.** Membrane partitioning: distinguishing bilayer effects from the hydrophobic effect. *Biochemistry*, 32:6307–6312, 1993.
- [147] **W.K. Subczynski, J.S. Hyde, and A. Kusumi.** Effect of alkyl chain unsaturation and cholesterol intercalation on oxygen transport in membranes: a pulse ESR spin labeling study. *Biochemistry*, 30:8578–8590, 1991.
- [148] **R.J. Pace and S.I. Chan.** Molecular motions in lipid bilayers. III. Lateral and transverse diffusion in bilayers. *The Journal of Chemical Physics*, 76:4241, 1982.
- [149] **S. Cannan, J. Zhang, F. Grunfeld, and P.R. Unwin.** Scanning electrochemical microscopy (secm) studies of oxygen transfer across phospholipid monolayers under surface pressure control: comparison of monolayers at air/water and oil/water interfaces. *Langmuir*, 20:701–707, 2004.

- [150] **T.R. Sosnowski, L. Gradon, M. Skoczek, and H. Drozdziel.** Experimental evaluation of the importance of the pulmonary surfactant for oxygen transfer rate in human lungs. *International Journal of Occupational Safety and Ergonomics: JOSE*, 4:391, 1998.
- [151] **J. Zhang, J. Strutwolf, S. Cannan, and P.R. Unwin.** Combined scanning electrochemical microscopy-langmuir trough technique for investigating phase transfer kinetics across liquid/liquid interfaces modified by a molecular monolayer. *Electrochemistry Communications*, 5:105–110, 2003.
- [152] **M.I.S. Macho, A.G. González, and A.S. Varela.** Photophysical study of pyrene-labeled phospholipids at the gas/water interface. *Langmuir*, 16:9347–9351, 2000.
- [153] **B.J. Alder and T.E. Wainwright.** Studies in molecular dynamics. I. General method. *The Journal of Chemical Physics*, 31:459, 1959.
- [154] **W.L. Jorgensen, J.D. Madura, and C.J. Swenson.** Optimized intermolecular potential functions for liquid hydrocarbons. *The Journal of the American Chemical Society*, 106:6638–6646, 1984.
- [155] **O. Berger, O. Edholm, and F. Jähnig.** Molecular dynamics simulations of a fluid bilayer of dipalmitoylphosphatidylcholine at full hydration, constant pressure, and constant temperature. *Biophysical Journal*, 72:2002–2013, 1997.
- [156] **W.F. Van Gunsteren and H.J.C. Berendsen.** A leap-frog algorithm for stochastic dynamics. *Molecular Simulation*, 1:173–185, 1988.
- [157] **M. Tuckerman, B.J. Berne, and G.J. Martyna.** Reversible multiple time scale molecular dynamics. *The Journal of Chemical Physics*, 97:1990, 1992.
- [158] **H.J.C. Berendsen, J.P.M. Postma, W.F. van Gunsteren, and J. Hermans.** Interaction models for water in relation to protein hydration. *Intermolecular Forces*, 331, 1981.
- [159] **T. Darden, D. York, and L. Pedersen.** Particle mesh Ewald: An $N \log(N)$ method for Ewald sums in large systems. *The Journal of Chemical Physics*, 98:10089, 1993.
- [160] **M. Parrinello and A. Rahman.** Polymorphic transitions in single crystals: A new molecular dynamics method. *Journal of Applied Physics*, 52:7182–7190, 1981.
- [161] **G. Bussi, D. Donadio, and M. Parrinello.** Canonical sampling through velocity rescaling. *The Journal of Chemical Physics*, 126:014101, 2007.
- [162] **M. Javanainen, L. Monticelli, J.B. de la Serna, and I. Vattulainen.** Free Volume Theory Applied to Lateral Diffusion in Langmuir Monolayers: Atomistic Simulations for a Protein-Free Model of Lung Surfactant. *Langmuir*, pages 438–443, 2010.
- [163] **J.P. Ryckaert, G. Ciccotti, and H.J.C. Berendsen.** Numerical integration of the cartesian equations of motion of a system with constraints: molecular dynamics of n-alkanes. *Journal of Computational Physics*, 23:327–341, 1977.

- [164] **B. Hess, H. Bekker, H.J.C. Berendsen, and J. Fraaije.** LINCS: a linear constraint solver for molecular simulations. *The Journal of Computational Chemistry*, 18:1463–1472, 1997.
- [165] **B. Hess.** Determining the shear viscosity of model liquids from molecular dynamics simulations. *The Journal of Chemical Physics*, 116:209, 2002.
- [166] **M.H. Abraham, P.L. Grellier, and R.A. McGill.** Determination of olive oil-gas and hexadecane-gas partition coefficients, and calculation of the corresponding olive oil-water and hexadecane-water partition coefficients. *Journal of the Chemical Society, Perkin Transactions 2*, pages 797–803, 1987.
- [167] **J.H. Weaver and B.J. McCall.** Crc handbook of chemistry and physics. *The Journal of the American Chemical Society*, 129:724, 2007.
- [168] **A.D. MacKerell Jr, D. Bashford, M. Bellott, R.L. Dunbrack Jr, J.D. Evanseck, M.J. Field, S. Fischer, J. Gao, H. Guo, S. Ha, et al.** All-atom empirical potential for molecular modeling and dynamics studies of proteins. *The Journal of Physical Chemistry B*, 102:3586–3616, 1998.
- [169] **J. Fischer and S. Lago.** Thermodynamic perturbation theory for molecular liquid mixtures. *The Journal of Chemical Physics*, 78:5750, 1983.
- [170] **D.R. Lide.** *CRC handbook of chemistry and physics 2009–2010 : A Ready reference book of chemical and physical data.* CRC Press, Boca Raton, 90th edition, 2009.
- [171] **P. Jedlovsky and M. Mezei.** Effect of cholesterol on the properties of phospholipid membranes. 2. free energy profile of small molecules. *The Journal of Physical Chemistry B*, 107:5322–5332, 2003.
- [172] **E.S. Smotkin, F.T. Moy, and W.Z. Plachy.** Dioxygen solubility in aqueous phosphatidylcholine dispersions. *Biochimica et Biophysica Acta (BBA)-Biomembranes*, 1061: 33–38, 1991.
- [173] **G.G. Power and H. Stegall.** Solubility of gases in human red blood cell ghosts. *The Journal of Applied Physiology*, 29:145, 1970.
- [174] **P. Jedlovsky and M. Mezei.** Calculation of the free energy profile of H₂O, O₂, CO, CO₂, NO, and CHCl₃ in a lipid bilayer with a cavity insertion variant of the widom method. *The Journal of the American Chemical Society*, 122:5125–5131, 2000.
- [175] **P. Han and D.M. Bartels.** Temperature dependence of oxygen diffusion in H₂O and D₂O. *The Journal of Physical Chemistry*, 100:5597–5602, 1996.
- [176] **R.T. Ferrell and D.M. Himmelblau.** Diffusion coefficients of nitrogen and oxygen in water. *The Journal of Chemical and Engineering Data*, 12:111–115, 1967.
- [177] **I.M. Krieger, G.W. Mulholland, and C.S. Dickey.** Diffusion coefficients for gases in liquids from the rates of solution of small gas bubbles. *The Journal of Physical Chemistry*, 71:1123–1129, 1967.

-
- [178] **L.K. Ju and C.S. Ho.** Oxygen diffusion coefficient and solubility in n-hexadecane. *Biotechnology and Bioengineering*, 34:1221–1224, 1989.
- [179] **B.G. Dzikovski, V.A. Livshits, and D. Marsh.** Oxygen permeation profile in lipid membranes: comparison with transmembrane polarity profile. *Biophysical Journal*, 85: 1005–1012, 2003.
- [180] **M.H. Cohen and D. Turnbull.** Molecular transport in liquids and glasses. *The Journal of Chemical Physics*, 31:1164, 1959.